# Development of a Novel Super Resolution Microscopy Technique using an Electron Beam for High Resolution Imaging

**Clare Lois Dennison**

PhD

University of York

Biology

September 2014

## Abstract

The requirement for spatial resolution that surpasses the limitations of classical light microscopy has proceeded along two paths; super-resolution light microscopy and electron microscopy. Optical microscopy offers multicolour flexibility for use in live cell imaging. Conversely, electron microscopes require a vacuum, and are essentially monochromatic; biological materials require dehydration and laborious treatments.

Correlative light and electron microscopy endeavours to combine the two imaging approaches to maximise spatial resolution and correlate these images with live cell dynamics. The JEOL ClairScope atmospheric scanning electron microscope (ASEM) enables wide-field fluorescence microscopy on living cells, and can then obtain electron microscope images on the same sample in a hydrated environment. In many cases this would use conventional heavy metal stains; this project aimed to use the instrument for investigations of specific biological interactions, using immunogold.

The labelling protocols were verified using the model system of actin in cells. The achievable resolution of the ClairScope was determined to be about 20 nm. Immunogold labelling was used to investigate the recycling dynamics of vesicles in neuroblastoma cells. The use of fluid phase markers such as FM dyes were used in attempts to correlate fluorescence and ASEM, although it was discovered that in an aqueous environment these markers were not suitable.

The immunogold labelling system was further employed to investigate of the previously reported association of the protein kinase A (PKA) subunit RIα. Puncta of this protein were observed to form during differentiation of neuroblastoma cells following treatment with cAMP. Various techniques in fluorescence microscopy were employed in the study of RIα localisation. Photobleaching revealed that RIα puncta freely exchanged with cytoplasmic molecules. Further work is required to shed light on the signalling mechanism of neuroblastoma differentiation.

## Contents

## List of Figures

## List of Tables

## Acknowledgements

I would like to thank my supervisors Peter O’Toole and Gareth Evans for their guidance throughout the project. I would also like to thank Ian Morrison for his endless support regarding data analysis.

Thanks also to my TAP committee, Christoph Baumann and Paul Pryor, along with Andy Yarwood and Jason Dalby (JEOL) for their advice throughout the project.

To the many friends I have made during this project, thank you for the encouragement and support.

## Declaration

I, Clare Lois Dennison, declare that this thesis is a presentation of original work and I am the sole author. This work has not been previously presented for an award at this, or any other, University. All sources are acknowledged as references.

# 1.0 Introduction

## 1.1 The history of microscopy

Modern microscopy has developed from the earliest observations of insects using magnifying glasses through the development of single lensed microscopes by Van Leeuwenhoek (1632-1723). Through improved lens production greater magnification was achieved enabling initial scientific cell biology observation of microscopic objects, such as bacteria, yeast and blood cells (Dobell & Leeuwenhoek 1932). In 1665 Robert Hooke published Micrographia, where he described illustrations of the structural mesh of a sample of cork as 'cells'; the first description of the fundamental unit of life, the cell (Hooke, 1665).

There still remained problems resulting from chromatic and spherical aberrations in optical lenses. Improvements have been achieved by using combinations of lenses with different shapes and refractive powers, thus reducing chromatic aberration. The studies of optical principles by Ernst Abbe helped to overcome problems caused by the diffraction of the glass lenses and chromatic aberration, which is necessary for observing the smallest resolvable detail (Abbe 1873). Chromatic aberration results from the non-convergence of refracted wavelengths of light, due to differences in refractive indexes of the microscope lens. To overcome this, lenses such as achromatic and apochromatic lenses are used. Achromatic lenses are corrected to allow two wavelengths to converge at one focal plane and apochromatic lenses are corrected to allow three wavelengths to converge at one focal plane. This correction is achieved through the use of Abbe's formula to calculate the correct focal length of each lens to ensure one focal spot with minimal error. Apochromatic lenses also allow correction for spherical aberration, which can arise from the increased refraction of light rays when they strike the curved edge of a lens. The combined effects of diffraction and chromatic aberration give rise to the point spread function (PSF), which depends on the numerical aperture (NA) of the lens; the narrower the aperture the higher the diffraction of the point spread function, giving a lower resolution of the image. Angular resolution is determined by the Rayleigh criterion (Rayleigh 1879; S, L.R.S.R 1896). This describes the minimum separation between two light sources required so that they may be resolved as two distinct objects, where the aperture of the lens and the wavelength of the light source results in the separation of the diffraction patterns, or Airey rings, of the two objects. Application of these theories has resulted in improvements in optical microscopy increasing the optical resolution, although this is still limited to ~200 nm. This is due to the physical limitations set by the diffraction limit of visible light; as described in Abbe's law this is approximately half the wavelength of light used (as described below).

$$\mathbf{d = \frac{\lambda}{2NA}}$$

The resolution limit of the optical light microscope, where d= resolution, λ= wavelength of the light source used and NA= numerical aperture of the lens.

### 1.2 Overcoming the resolution limitations of light microscopy

The development of electron microscopy by Ernst Ruska, as early as the 1931 (Knoll, M. and Ruska, E. 1931), helped to overcome the resolution limitation of optical microscopy using visible light. This method uses the same basic design as a light microscope, except the light source is replaced with an electron beam source. This passes through apertures and electromagnetic fields, which focus the beam, as would a series of glass lenses. As this technique uses an electron beam in place of a light beam resolution is no longer limited by the wavelength of light, but by the equivalent wavelength of the electron beam, which depends on the accelerating voltage used.  In transmission electron microscopy (TEM) the electron beam is transmitted through thin sections of resin embedded samples. As the electron beam passes through the sample the electrons are deflected or absorbed by the sample; these effects manifest themselves in different degrees of transmission as a function of position in the sample section. Contrast it created by these interactions, forming the TEM image; although low contrast in is intrinsic in the imaging of biological samples due to the low electron density of carbon, nitrogen and phosphorus found in biomacromolecules. Therefore, heavy metal stains are commonly used to enhance contrast in TEM. Application of TEM can improve image resolution to within fractions of nanometers and is a valuable imaging method revealing high detail resolution of cellular ultrastructure and insight into protein-protein interactions. However, limitations of contrast in biological samples and the requirement for ultrathin sections limit this high resolution technique to the imaging of fixed cell samples only, which must be imaged under vacuum.

The introduction of a scanning EM (SEM) by Manfred Von Ardenne (Ardenne 1938) enabled the imaging of the surface topology of a sample. In this system an electron beam is scanned across the surface of the sample, interacting with the electrons in the sample to produce secondary and back scattered electrons. Detection of these electrons in relation to the beam and position are combined to create an image with an achievable resolution down to 1 nm.

### Improvements in imaging

The problems encountered by early microscopists included the lack of contrast in biological samples. Methods were developed including phase contrast (Zernike 1942) and differential interference contrast (DIC) (Allen et al. 1969) and the use of fluorescent stains. Further advances saw the development of the use of fluorescence in microscopy to create contrast. Early studies used fluorescent stains such as Fluorescein and Rhodamine which can be covalently linked to target proteins, and nuclear stains such as 4’, 6’-diamino-2-phenylindole (DAPI); later fluorescent proteins, such as green fluorescent protein (GFP) were introduced. The cloned GFP gene from the jellyfish *Aequorea victoria* has revolutionised the non-invasive study of live cell function and protein dynamics, as reviewed by (Tsien 1998). The cloning of the GFP complementary DNA sequence and protein expression in *Escherichia coli* (*E.coli*) to produce a fluorescent product, was first achieved by Chalfie et al. (1994). This fluorescent product was further enhanced through introducing mutations guided by atomic resolution crystal structures (Heim et al. 1995), which resulted in enhanced fluorescence emission and altered fluorescence excitation and emission spectra (Heim et al. 1994; Ormö et al. 1996 and Gross et al. 2000).

Fluorescence in light microscopy is achieved by using an excitation light source at a specific wavelength tuned to the chosen fluorophore. The fluorophore becomes excited by absorption of photons from the excitation light source, creating an excited electronic singlet state. Energy is then lost through the emission of a photon as the electron returns to its ground state as shown in Figure 1.1.1 as a Jablonski diagram (Jablonski A., 1933; Frackowiak 1988). High energy photons have shorter wavelength; the loss of energy results in emission at a longer wavelength; this energy change is described as the Stokes shift for the fluorophore. Classically, specific dichroic mirrors and filters are chosen to match the spectral properties of the chosen fluorophore; therefore intense excitation light can be separated from weaker fluorescence emission using an emission filter before the detector, where the fluorescent image is formed.

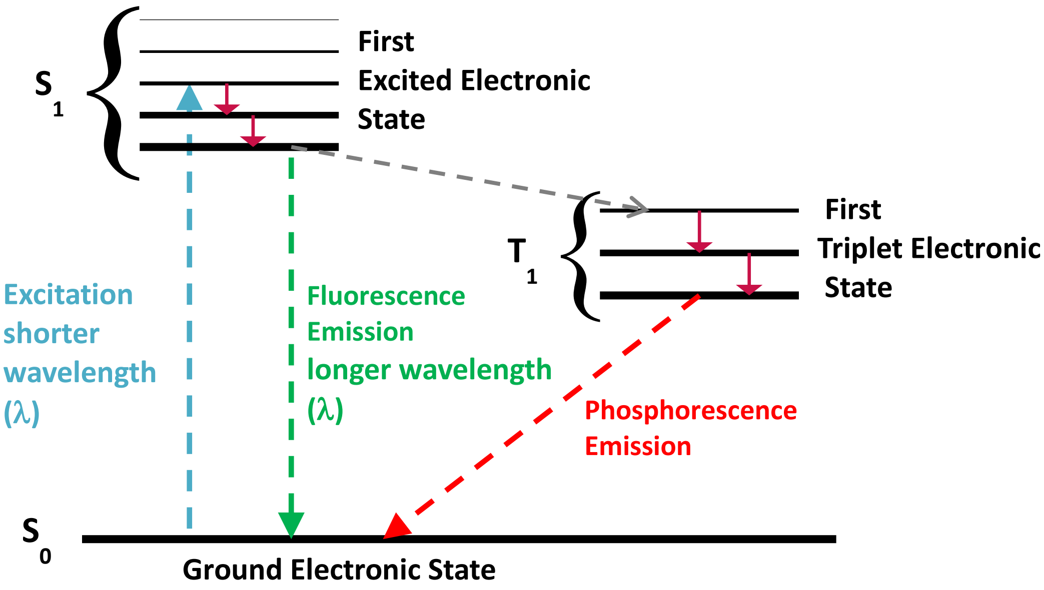

**Figure 1.1.1. Jablonski Diagram for electronic states associated with fluorescence and luminescence emission.** A photon of energy is absorbed by an excitable molecule, populating the excited electronic singlet. This descends to its lowest vibrational state, then drops to the ground state emitting a longer wavelength photon (green). An alternative route may populate a triplet state and results in phosphorescence emission. (Image hand-drawn).

The three dimensional nature of some samples can cause difficulties due to out-of-focus effects, which in turn limit the attainable resolution. The confocal microscope was developed to enable 'sectioning' of 3 dimensional samples by eliminating out of focus fluorescence from all but a defined focal plane (Minsky, 1957). This is achieved through the light source beam passing through an aperture to create a point source which is focussed on a small area by the objective lens producing point illumination. Fluorescence as well as scatter and reflected light is collected through the objective lens; this must pass through a detection aperture/pin hole which is parfocal to the illumination point and obstructs any light outside of the selected focal plane. This filtering effect at the focal plane improves the achievable optical resolution, especially in samples of increasing sample depth, allowing optical sectioning, where in-focus images are collected at selected focal planes throughout the sample (Cremer & Cremer 1978; Sheppard & Wilson 1981). In modern confocal 'laser scanning' microscopes (CLSM) detected light is further split by a beam splitter to select desired emission wavelengths. After passing through the pinhole the light intensity is detected by photomultiplier tubes (PMT), which transform the signal into images. The introduction of CLSM has enabled the collection of images by a laser scanning over the sample to produce an image in a single focal plane collecting light of the image in each pixel, line by line at one of many different wavelengths. The scan speed of the laser may be varied to produce better signal to noise, depending on the fluorescence intensity of the sample. Fluorescence intensity is lower compared with simple wide field fluorescence imaging due to the pinhole removing an element of the emitted light, due to the restriction of fluorescence detection, resulting in the need for longer sampling times.

Despite recent advances, the resolution of EM is still frequently needed to gain higher resolution as well as complementary structural information. Fluorescent stains cannot readily be detected by electron microscopy and may be destroyed by the electron beam. Therefore other probes such as FM dyes have been developed to display properties such as photoconversion from a fluorescent dye to electron dense material, allowing visualisation by both imaging methods (Miesenböck et al. 1998). The use of a combination of both fluorescence and electron microscopy is commonly referred to as correlative light and electron microscopy (CLEM). CLEM techniques are designed to gain benefit from live cell imaging by light microscopy with high resolution gained by electron microscopy; relating function to the surrounding ultrastructure. This has been beneficial in many areas of research, notably these developments have advanced studies into membrane trafficking, cellular trafficking and neuronal activity.

The study of membrane trafficking and the cytoskeleton has been a driving factor behind the development of techniques in microscopy, which has advanced the improvement of achievable resolution in order to visualise mechanisms behind the secretory pathway and vesicle trafficking; reviewed by Lange et al. (2001). A schematic of the secretory pathway is shown in Figure 1.2.1, which reveals the myriad of membrane bound compartments, which dynamically transport protein carbohydrate and lipids within the cell and to the extracellular milieu. The various compartments can be isolated by biochemical fractionation, but the development of fluorescence microscopy has allowed these dynamic pathways to be observed and dissected.

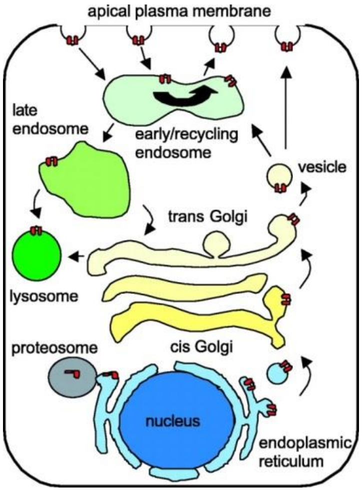

**Figure 1.2.1 Intracellular membrane trafficking.** Vesicles leave the rough endoplasmic reticulum and travel through the Golgi, where they undergo glycosylation. Vesicles leave the Golgi and can travel directly to the apical plasma membrane or to the recycling endosome. Vesicles may enter the late endosome to lysosome pathway for degradation, mis-folded proteins are degraded by the proteosome (Bertrand & Frizzell 2003). Disclaimer: American Physiology Society grants permission for free use of our articles (in whole or in part) in education materials, provided i) there is no charge ii) those materials are not directly or indirectly commercially supported.

The advent of GFP labelling enabled the tracing of components of the endoplasmic reticulum (ER) in live cells (Scales et al. 1997). The contents of vesicular tubular complexes (VTCs) in living cells were labelled with GFP to reveal movement along microtubules from the ER, dependent on dynactin and dynein (Presley et al. 1997). The trafficking of synaptic vesicles and associated proteins to the growth cone plasma membrane occurs by similar mechanisms. Axonal membrane transport has previously been visualised by video enhanced contrast differential interference contrast (VEC-DIC) (Allen et al. 1982). This imaging method led to the discovery of the kinesin motor protein and the directed organelle transport in living axons (Vale et al. 1985).

### 1.3 Overview of imaging synaptic activity

The study of neuronal activity is crucial in understanding the processes involved in fundamental synaptic transmission as well as when these connections are modulated in processes such as learning and memory. Methods used to measure activity include electrophysiological measurements of membrane potential under stimulation or measurement of stimulation of cellular activity by incubation with chemicals that initiate signalling pathways. These may then be traced in live cells by labelling proteins with fluorescent markers, which this study will discuss further. Pioneering research into the application of electrophysiological measurements of synaptic vesicle activity at neuronal synapses was carried out by Bernard Katz in the 1950s. These investigations described how the release of neurotransmitter at the synapse is quantal; at any particular synapse the amount of neurotransmitter will never be less than a certain amount (Fatt & Katz 1952; Del Castillo & Katz 1954).

Since the first cell culture experiments, neuronal differentiation has long been studied in order to identify the mechanisms involved. Classical measurement of neuronal activity has involved the stimulation of primary cultured neurons or differentiation of neuroblastoma cells, to form neuron-like cell projections. This research mainly focusses on the formation of neurites, axons, dendrites and synaptic formation and organisation.

Synaptogenesis results in the formation of tight connections between neurons at junctions known as synapses (Nirenberg et al. 1983; Bianchi et al. 2013). At these junctions information from an action potential is transferred through release of neurotransmitter from the presynaptic terminal; these chemical signalling molecules diffuse across the synaptic cleft to the postsynaptic terminal where the neurotransmitters bind specifically to post synaptic receptors and activate transduction of the action potential along the postsynaptic terminal.

An action potential occurs through the change in membrane potential of an axon. At -70mV the axon is at resting potential, a change in membrane potential can result in a small depolarisation of the membrane potential, Figure1.3.1. If this reaches the threshold potential of -65mV, depolarisation occurs; a change in internal sodium ($Na^+$) and external potassium ($K^+$) levels occurs via the active diffusion of extracellular $Na^+$ into the axon through voltage gated ion channels and vice versa in the case of the $K^+$ ions. Repolarisation of the membrane potential through diffusion of $K^+$ out of the cell stabilises the electrochemical gradient. Shortly after the $K^+$ channels close a period of hyperpolarisation occurs, the refractory period where no action potential can occur, until the resting potential is re-established, (reviewed in Bean 2007).

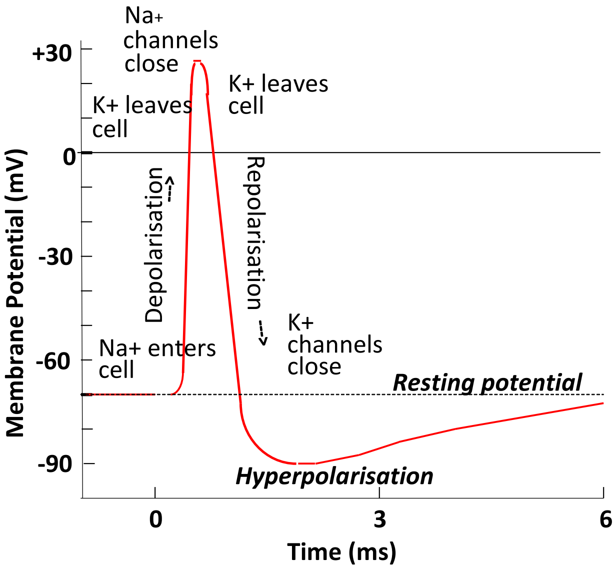

**Figure 1.3.1 Action Potential.** Depolarisation of the synaptic membrane occurs as $Na^+$ ions enter the cell and $K^+$ ions leave the cell through voltage gated ion channels. Repolarisation occurs through the diffusion of $K^+$ out of the cell. A period of hyperpolarisation occurs until resting potential is recovered. Image hand-drawn.

Synaptic activity in response to stimulation such as neurotransmitter release is crucial in neuronal plasticity, although the true extent of the relationship between presynaptic structural organisation and the functional dynamics within the presynaptic terminal remains unclear. Synaptic vesicles fill the presynaptic terminal; they have uniform shape and size at ~40-50 nm in diameter and contain neurotransmitters such as glutamate (Shulman et al. 2004; Schafer and Jones 1982). Exocytosis and endocytosis of synaptic vesicles occurs at a specialised area of the presynaptic membrane known as the active zone (AZ), resulting in the release of neurotransmitter into the synaptic cleft (Heuser and Reese 1973). The organisation of synaptic vesicles within the presynaptic terminal is considered essential for neurons to maintain neurotransmitter release under stimulation. Studies have shown synaptic vesicles localise in distinct 'pools' within the presynaptic terminal (Staras et al. 2010). These are supported by interactions between synaptic vesicles and actin filaments, although it remains unclear if this organisation is spatial or purely functional. It is thought that these actin filaments undergo structural rearrangements during cell depolarisation, enabling synaptic vesicle trafficking and recycling events (Südhof 1995).

Synaptic vesicles clustered adjacent to the AZ are described as 'docked'; Figure 1.4.2. These synaptic vesicles are specialised as they have undergone a maturation process which 'primes' them for fast exocytosis, a process regulated by internal presynaptic calcium concentration (Klenchin & Martin 2000 and Pumplin et al. 1981). Internalisation of the fused synaptic vesicle membrane occurs from the AZ through the endocytosis of clathrin coated pits (Mundigl & De Camilli 1994 and Heuser 1989). These vesicles quickly acidify and shed their clathrin coatings, attaching to an early endosomal compartment in preparation to be refilled with neurotransmitters and then translocated to the reserve pool (Mundigl & De Camilli 1994). Synaptic vesicles clustered in the reserve pool replenish the readily releasable pool as synaptic vesicles are translocated to the plasma membrane to dock and undergo priming and fusion, completing the cycle; Figure 1.4.1. (Fredj & Burrone 2009).

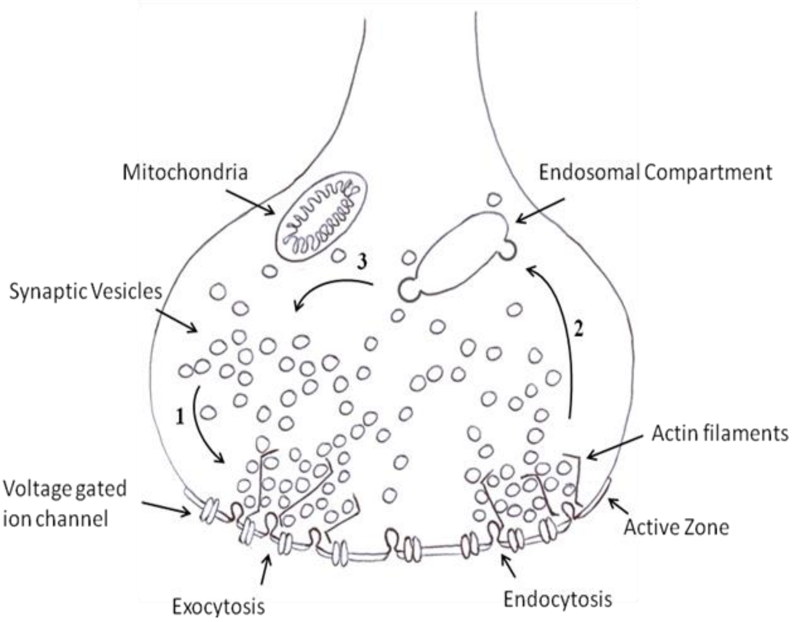

**Figure 1.4.1 Synaptic vesicle recycling events at the presynaptic terminal.**
Schematic showing the stages of synaptic vesicle recycling at the presynaptic terminal. 1) Exocytosis of synaptic vesicles in the readily releasable pool, to the active zone of the presynaptic terminal. 2) Endocytosis of synaptic vesicles at the active zone and attachment to early endosomal compartments and clustering in the reserve pool. 3) Synaptic vesicles are trafficked from the reserve pool to the readily releasable pool under stimulation to undergo exocytosis. (Image hand-drawn).

## 1.4 Fluorescence techniques in biological imaging

The development of sophisticated techniques in fluorescence microscopy has enabled analysis of protein –protein interactions and trafficking in live neuronal cells. Förster (or fluorescence) resonance energy transfer (FRET) is a distance dependent energy transfer between two fluorescent molecules; these are termed the donor and the acceptor molecules (Förster 1948). This interaction occurs when energy from the donor molecule following excitation is passed without emission of a photon, to the acceptor molecule which in turn is excited and emits at a longer, red shifted wavelength compared to the donor.  This interaction can only occur when the donor and acceptor are within ≤10 nm, which makes this technique an excellent measure of the distance between proteins or ultrastructure.

FRET has been successfully applied in the study of intracellular 3'-5'-cyclic adenosine monophosphate (cAMP) concentrations, as in a study by Zaccolo and Pozzan (2002) which enabled the visualisation of microdomains of high concentrations of cAMP, indicating the specific localisation of cAMP within the cell. Amongst many molecules involved in neuronal differentiation, a major contributor is the intracellular secondary messenger cAMP (Sutherland EW 1970). cAMP has been shown to promote neurite outgrowth and synaptogenesis, differentiating a variety of cell lines into neuronal-like cells. Differentiation of cells by cAMP occurs through the phosphorylation of effector proteins controlled by opposing actions of protein kinases and phosphatases. Protein kinase A (PKA) (also known as cAMP –dependent kinase) is an enzyme complex which has long been considered a major constituent in neuronal differentiation. Stimulation with cAMP initiates a kinase cascade, where surrounding effector proteins are phosphorylated (Krebs et al. 1959; Herberg et al. 2000; Akimoto et al. 2013).

PKA activity has also been measured by FRET between conjugated polymer and fluorescently labelled peptide. This monitored electrostatic interactions between the peptide and conjugated polymer; an increase in FRET efficiency was observed following phosphorylation. The same method was applied to monitor PKA activity in the presence of PKA inhibitor H-89 (Tang et al. 2014).

Intracellular membrane fusion is mediated by a fusion complex comprised of N-ethylmaleimide-sensitive factor N-terminal peptides (SNAREs) (Kuge et al. 1994; Kümmel et al. 2011), and Sec 1/Munc18 (SM) proteins (Dulubova et al. 2007). Syntaxin forms stable intracellular SNARE complexes with SNAP-25, but only if the two proteins encounter each other before syntaxin interacting with Munc18-1 (Dulubova et al. 2007). Fluorescence lifetime imaging (FLIM) demonstrated ectopic interactions on the Golgi body between SNARE proteins. Munc18-1 binds to the closed form of syntaxin and traffics to the plasma membrane, but remains inactive in the presence of SNAP-25. It was observed that an influx in $Ca^{2+}$ increases the number of SNARE clusters at the plasma membrane which contain interacting t-SNARE proteins, revealing information about the importance of munc18-1 in the SNARE trafficking cycle (Medine et al. 2007).

### Circularly permuted GFP.

The circularly permuted GFP (cpGFP) variants have undergone rearrangements where two portions of the polypeptide are flipped around a central site (shown in Figure 1.5.1) (Topell et al. 1999). With these conformational changes the β-can has increased sensitivity to protons outside of the structure. This adaptation allows the use of the probe in identification of interaction signals that occur in the chormophore cleft by a change in electrostatic potential of the chromophore to produce a fluorescent signal. It has been shown that when a cpYFP fluorescent probe was fused with calmodulin (CaM) and M13, a 26 residue peptide from the CaM binding region, the fluorescence properties of this complex changed upon interaction with $Ca^{2+}$ (Nagai et al. 2001).

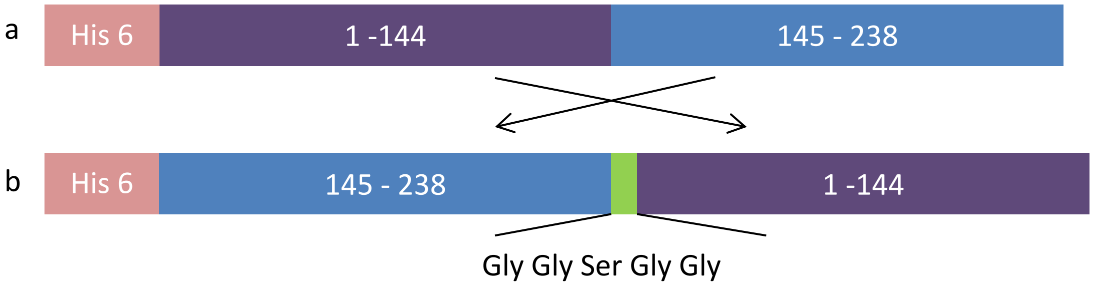

**Figure 1.5.1 Modifications to GFP yielding cpGFP**. a) EGFP, b) cpEGFP. Amino and carboxyl terminals of EGFP are switched and reconnected with a short spacer (green) (Nagai et al. 2001).

### SynaptopHluorin

Stimulated synaptic activity, vesicle distribution and dynamics have been successfully observed by using of fluorescent markers to label vesicle membrane proteins. An example of such is the fluorescent marker synaptopHluorin (spH), a protein fusion of a pH sensitive GFP mutant with the luminal domain of the vesicle associated membrane protein (VAMP), also known as synaptobrevin (Miesenböck et al. 1998). Application of this fluorescent probe has enabled the fluorescent identification of individual synaptic vesicle fusion events at the presynaptic membrane, (Miesenböck et al. 1998).

This is achieved through changes in pH levels; during intracellular stages the vesicular luminal compartment remains at pH 5.5, when fluorescence is quenched. On synaptic vesicle exocytosis the lumen bound spH is exposed to the synaptic cleft, where the pH is 7.4; this change in pH results in synaptopHluorin fluorescence emission. This fluorescence is observed until re-acidification of vesicles occurs, following endocytosis, which quenches fluorescence. This process is shown schematically in Figure 1.6.1.

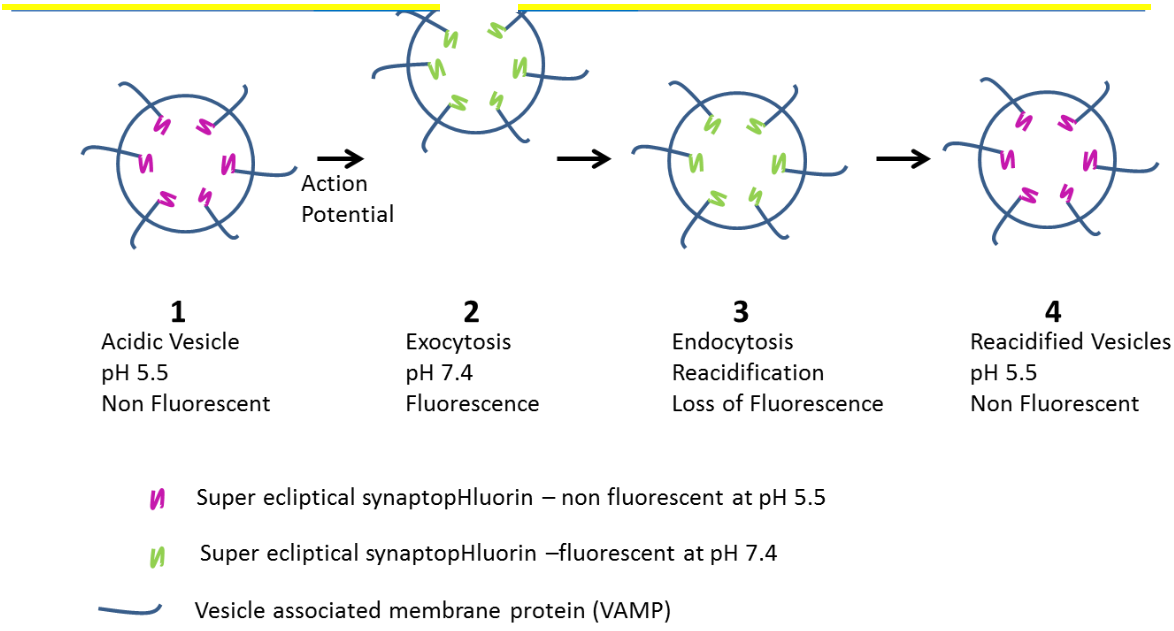

**Figure 1.6.1 pH dynamics of SynaptopHluorin**

1) During intracellular stages the luminal compartment of the synaptic vesicles is at pH 5.5. 2) Action potential firing (AP) induces SV fusion with the presynaptic membrane, exposing the lumen bound spH to synaptic cleft at pH 7.4, seen by an increase in spH fluorescence. 3) Acidification of the internalised synaptic vesicles quenches fluorescence. 4) Reacidification of the vesicle lumen results in spH returning to a non-fluorescent state. Figure hand drawn, based on Ryan & Reuter (2001).

The fluorescent tagging of vesicles by spH has aided the study of active vesicle recycling in hippocampal small synapses under electrical and chemical stimuli (Gandhi and Stevens 2003). Other related studies using fluorescent markers have resulted in the identification of stimulated bulk endocytosis in response to varying stimuli (Clayton, Evans, and Cousin 2008).

Direct measurement of synaptic vesicle turnover has also been studied in the presynaptic terminal by measuring internalisation of fluorescently labelled antibody specific for the luminal epitope of the vesicular protein synaptotagmin (Malgaroli et al. 1995). This ratiometric measure of antibody uptake during incubation with neuronal cells allowed direct measurement of changes in synaptic vesicle recycling activities by immunofluorescence detection during known changes in stimulation. Similarly the internalisation of synaptotagmin specific antibody probes was used to monitor the synaptic vesicle recycling events at cerebellar granule cell synapses in the absence of action potentials. Internalised antibody was labelled with fluorescent markers to reveal the true extent of vesicle recycling and localisation with PKA in the presynaptic terminal in both resting state and stimulated conditions. This enabled the measurement of rate of spontaneous vesicle exocytosis in comparison to vesicle dynamics induced by the addition of cAMP (Chavis et al. 1998).

The internal acidity of synaptic vesicles is a key mechanism in vesicle function and also the fluorescence and quenching of lumen bound spH. A study into the relationship between vesicle pH and spH fluorescence showed that the rate of vesicle acidification ranged from 500 milliseconds to 1 second. This rate increased with increasing concentrations of extracellular adenosine triphosphate (ATP) and glutamate, suggesting that vesicle recycling  may be regulated by changes in concentration of available neurotransmitter (Budzinski et al. 2011).

The fluorescent tagging of vesicles by spH has also aided the study of active vesicle recycling in hippocampal small synapses under electrical and chemical stimuli (Gandhi & Stevens 2003). Live cell imaging of synaptic vesicle release and retrieval has also been measured by this method in doperminergic (DA) neurons. This revealed that DA neurons, in comparison to hippocampal neurons, show limited depletion of the recycling pool under increasing stimulus, even though exocytosis rates are similar. This suggests that the depletion may be dependent on the frequency of endocytosis (Mani & Ryan 2009). This technique has also resulted in the identification of differing modes of endocytosis of synaptic vesicle retrieval in response to varying stimuli, such as bulk endocytosis (Clayton et al. 2008). These techniques provide valuable information into cellular activity, but lack the sensitivity required to define the mechanisms and outcomes of individual cells.

## 1.5 Super resolution light microscopy techniques

To enable visualisation of synaptic vesicle and protein distributions, microscopy has seen a recent expansion of SRM techniques. The techniques typically enable imaging with a 2-10x improvement in resolution. Each technique has its own advantages and disadvantages and is suited to specific sample types.

### Total internal reflection fluorescence microscopy

Total internal reflection fluorescence microscopy (TIRFM) illuminates cells in contact with a glass surface, using an evanescent wave, a near field wave that decreases exponentially with distance from the glass-water interface (Axelrod, D. 1981). This wave selectively illuminates and excites fluorophores directly adjacent to the glass/ water interface; only fluorophores in the evanescent wave are excited and can emit light (Mattheyses et al. 2010). These fluorophores lie in a layer ~100 nm from the glass-water interface, so the contribution of background signal for out of focus fluorochromes is strongly reduced which helps to increase the signal to noise whilst also improving the axial resolution. This field is usually created between a glass coverslip and a film of aqueous buffer, which sits between the coverslip and the sample. TIRFM can use either a prism coupled or an objective coupled design. TIRFM increases the axial z-resolution from a wide-field resolution of ~100nm, however, the lateral, x,y-resolution is not altered.

Biological applications of TIRFM exploit the limited depth of penetration of the evanescent wave resulting in high signal to background ratios and has been widely used in the visualisation of cell biological research by fluorescence microscopy. *In vivo* imaging is restricted to the study of membrane and membrane associated events, as only labelled molecules in a narrow layer in contact with the glass interface may be imaged, as reviewed by Matsuoka et al. 2012, Luo et al. 2013 and Bezzi & Volterra 2014).

### Single molecule fluorescence imaging.

Single molecule fluorescence imaging (SMFI) enables the quantification of fluorescence particles from sub-microscopic particles. Images are recorded on a cooled charge coupled device camera with high sensitivity. Each particle must be well separated from its neighbours so that the point spread function (PSF) approximates a 2-dimensional Gaussian shape, as shown in Figure 1.7.1. Each particle can then be fitted with a 2D Gaussian, to extract the position, width and intensity above local background, and the algorithm also provides an estimate for the error in each of these parameters (Cherry et al. 1998). The position is thus determined to a precision much better than the width of the peak, typically ~20 nm. This is also the basis of the following two super resolution methods.

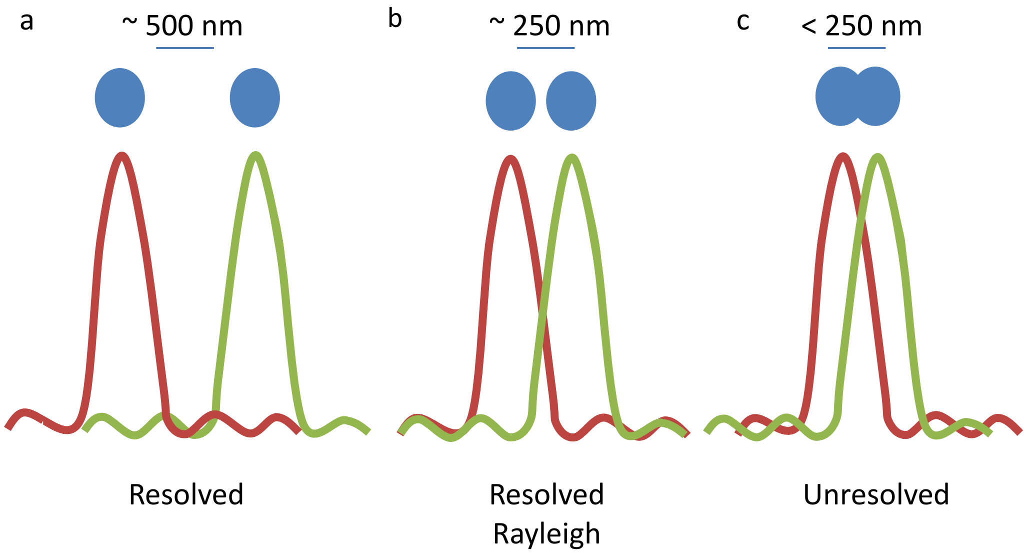

**Figure 1.7.1 Point Spread Function.** The point spread function as determined by the Rayleigh criterion, where resolution is limited by light diffraction alone. a) Two light sources are ~500 nm apart and resolved, as neither diffraction pattern overlaps on the other. b) Two light sources ~250 nm apart are resolved within the Rayleigh criterion. c) Two light sources are unresolved as the Rayleigh criterion is not met and the two light source diffraction patterns overlap. Figure hand drawn, based on Thorley et al. (2014).

### Photoactivated localisation microscopy (PALM)

The lateral and axial resolutions of far-field optical microscopy are improved through sequential imaging of densely packed and similarly labelled features. This enables the differentiation of individual target PSF from the surrounding features to achieve optimum individual resolution, as reviewed by (Hell 2007). Photoactivated localisation microscopy (PALM) is a technique that can improve the lateral resolution to ~20nm and enable greater accuracy in protein localisation, even when protein densities exceed the diffraction limit (Betzig et al. 2006). PALM enables this method by using genetically mutated fluorescent proteins, which have been mutated to produce a variety of fluorescent probes that may be photoactivated or photoswitched from a fluorescent state to a non -fluorescent state. Photoactivatable GFP (paGFP) (Patterson & Lippincott-Schwartz 2002), a probe which increases its fluorescence emission following irradiation with 413 nm light and excitation with 488 nm light and crucially, can remain stable for several hours, allowing long periods of imaging, or bleached with increased exposure to 488 nm light.

Challenges involved in this imaging technique include the fact that if all probes were excited at once, SRM imaging would only be possible if the probes were sparsely populated, as with SMFI. Photoactivatable probes can help overcome this limitation. Using paGFP as an example, inactivated paGFP is not fluorescent when imaged with blue light (e.g. 488 nm). However, using a violet light source (e.g. 405 nm laser), paGFP can be activated. These activated probes are then excited when imaged with blue light and can clearly be seen. To enable imaging of densely packed probes, activation is carefully undertaken such that only a few probes are activated at once. These probes are then imaged until bleached. The process is then repeated to activate remaining probes, yet to be imaged. This is done repetitively until all available probes have been visualised. Each PSF can then be fitted to a 2D Gaussian profile to localise its position, as with SMFI, with a resolution of around 20 nm. This approach is limited however by the lengthy imaging times required and the total bleaching following imaging of the sample, removing the possibility of further complementary imaging techniques. The development of PALM for biological imaging is reviewed by Sengupta et al. (2014).

PALM has been used to great effect to study the organisation of α-amino-3-hydroxy-5-methyl-4-isoxazolepropionic acid receptors (AMPA) at the neuronal synapse. These were shown to be highly concentrated at synapses in clusters that are ~70 nm in size (Izeddin et al. 2011). The spatial organisation of the calmodulin-dependent protein kinase II has also been visualised by PALM, revealing at least three kinetic subpopulations in hippocampal dendritic spines. These subpopulations were found to be distant from the synapse, suggesting diverse mechanisms of synaptic transmission regulation (Lu et al. 2014).

However, it can be difficult to only activate a few molecules in the first round of activation in densely packed regions of interest, such that only molecules separated by a distance greater than the diffraction limit are able to have their position calculated. If two probes are activated within this spatial volume, then their individual positions cannot be calculated; this means that not all probes will be imaged.

As PALM relies on fluorescent proteins, the technique is well suited to live cell imaging and the localisation of probes that are not restricted to the membrane itself. The pitfall is that the axial resolution is not improved and therefore the density of probes in the axial plane also needs to be considered. This can be minimised by using TIRFM in conjunction with PALM to decrease the contribution from out of focus probes.

Finally, fluorescent proteins typically have a maturation half-time of several hours (Corish & Tyler-Smith 1999) and not all fluorescent proteins will go on to form a functional chromophore. These facts will prevent all of the labelled proteins being visualised. PALM is well suited to studies of structural patterns, e.g. actin filaments, but it cannot label every protein and a proportion may remain unresolved (Durst et al. 2014).

### Stochastic optical reconstruction microscopy (STORM)

Stochastic optical reconstruction microscopy is very similar to PALM, but instead of using photoactivable dyes, it exploits photoswitchable dyes, such as Cy3-Cy5 which can be switched on and off and permit imaging of densely packed areas, by only switching on a few probes (Rust et al. 2006).

STORM relies on the concept that photoswitchable fluorophores can be used to resolve single fluorophores when multiple fluorophores are within the conventional resolution limit. This is achieved by switching many fluorophores to their dark state and imaging only a small number of probes that remain active; single molecules may be isolated and imaged and therefore their positions can be precisely localised (Tam et al. 2014). A localisation algorithm is then used to analyse a time-series of short exposure images and localise single molecules using Gaussian fitting, whilst also reducing noise and increasing the positional precision (Geissbuehler et al. 2011).

Photoswitching is typically achieved using synthetic dyes such as Cy3 and Cy5, which can be covalently attached to a specific antibody, and used to label the protein of interest (Bates et al. 2005). The sample will then often be fixed and permeabilised before antibody staining. Exposing the sample to an intense red laser power switches the dyes from an active state to a dark state where they will not emit upon excitation. As the probes enter an emitting state, they can be visualised until they once again become trapped in a dark state. Similar to PALM, imaging is repeated until all probes have been visualised (Zhuang 2009).

An adaptation of STORM is direct stochastic optical reconstruction microscopy (dSTORM) where fluorophores are embedded in a reducing buffer system for imaging, (used as a scavenging system to remove oxygen and reduce the effects of photobleaching; consisting of glucose oxidase and catalase (Shi et al. 2010)) where a fluorophore enters its triplet state it is reduced to a long lived radical state, where it remains dark for several seconds. This approach has been successfully used in the development of multicolour dSTORM, which can be used for imaging of complex biological systems (Lampe et al. 2012).

Unlike PALM, STORM is better suited to fixed samples where strongly reducing buffers can be used and the sample can be fixed and permeabilised to permit antibody labelling. Although not reliant on the maturation of chromophores found when using fluorescent proteins, each antibody ideally needs to be labelled with just one fluorescent dye. Due to the stochastic nature of the labelling process, this is not readily achieved and thus not all antibodies will have a fluorescent tag, whilst others will have more than one, and so again, this technique is ideally suited to studying structural details, but cannot be safely used for studying protein complexes at the level of precision needed for obtaining functional information.

Both PALM and STORM need repetitive imaging often over very prolonged time periods. Thousands of images are often collected to capture as many single probes as possible. This can result in images being acquired over tens of minutes. Although faster approaches have been developed (Sengupta et al. 2012), this improvement only really benefits structural studies where imaging of as many probes as possible is not vital.

Good examples come from regular studies of the neuronal actin cytoskeleton; such studies have revealed the 3D organisation of the actin cytoskeleton in cellular sheet-like protrusions (Xu et al. 2012). Similar studies have also suggested actin, spectrin and associated proteins co-localise in evenly spaced ring-like structures around the neuronal axon; importantly in this study these ring-like structures were shown to co-localise with axonal sodium channels, suggesting a possible link between structure and function (Xu et al. 2013).

STORM has also been effectively used to study synaptic plasticity in learning. A high abundance of brain derived neurotrophic factor BDNF was observed within glutamatergic presynapses of cultured hippocampal neurons, by the application of two colour dSTORM, suggesting that BDNF may be stored in small granules within the presynapse (Andreska et al. 2014).

Major advances in super resolution microscopy have significantly improved the spatial resolution of optical imaging to ~30 nm dynamics in live hippocampal neurons, allowing the tracking of F-actin dynamics, measured at the single particle level (Tatavarty et al. 2009).

### Structured illumination microscopy (SIM)

SIM illuminates a sample with a sinusoidal modulated light pattern created by superimposing two fine spatial frequency grid patterns. This passes through the sample and creates Moiré fringe patterns. Images are collected as a function of the sample as it is rotated in the imaging plane, collecting fluorescence images that contain spatial frequencies of the illuminated sample. By measuring the fringes in the resulting Moiré pattern normally unobservable frequencies are detected; computational deconvolution of these frequencies can increase the achievable resolution to ~100 nm when using commercial OMX or Nikon systems, although in ideal test samples 20 nm resolution can be achieved (Gustafsson 2000). This is achieved through specific microscopy protocols and extensive software analysis post-exposure, allowing otherwise unobservable sample information to be deduced from the fringes and computationally restored. Imaging of dendritic spines and protrusions by conventional fluorescence microscopy had identified the outgrowths as potential targets for postsynaptic excitatory targets. Only through advances in SRM light microscopy techniques such as SIM could these protrusions be quantified and further identified as crucial in neuronal connectivity and plasticity (Schouten et al. 2014).

### Stimulated emission depletion.

Stimulated emission depletion (STED) improves achievable resolution by using two laser beams, one to excite the fluorophores at the point of focus and the second to deplete fluorescence emission from proximal regions (Hell & Wichmann 1994). The depletion beam is passed through a phase plate that cuts out the centre of the beam, leaving a 'ring donut' of illumination that surrounds the excited area from the first shorter wavelength beam.  As the depletion laser power is increased, the effective volume of STED increases and thus leaving a smaller area in the centre able to actually emit photons. This reduces the effective area of fluorescence emission which can provide a resolution of ~30 nm (Willig, et al. 2006; Thompson et al. 2002). However as STED is not restricted to imaging probes with only one label, it should be possible to image most, if not all tagged proteins. However, the theoretical resolution (of 1 nm) is never achieved as the sample introduces aberrations that are detrimental to the image resolution. These become significant when imaging biological samples that have imperfect refractive structures, and are exacerbated as imaging moves away from the coverslip. Indeed, commercial systems, such as those from Leica, only quote improvements of around 2 fold over CLSM techniques to around 90 nm.

Another limitation of STED is that sample damage may occur due to the high intensity depletion beam needed. As the area left to fluoresce is limited, the signal returning to a PMT is also very low, and thus makes single molecule imaging very difficult due to the inherent poor quantum efficiency (QE) of PMT's. This can be overcome by increasing the image acquisition time, but again this increases exposure time and reduces its usefulness for real-time imaging.

Despite these inherent limitations, STED is still a powerful and useful technique in breaking the diffraction limit of light microscopy (Klar et al. 2000; Hein et al. 2008). Investigations into the processes underpinning synaptic vesicle recycling have successfully been studied by STED. For example, the vesicle protein synaptotagmin I was visualised at high resolution, revealing clustering of the protein during synaptic vesicle fusion at the presynaptic membrane and recycling in both the resting and stimulated states (Willig, et al. 2006).

Conventional fluorescence imaging protocols are being adapted for SRM, for example, the incorporation of fluorescent in situ hybridisation (FISH) in STED imaging. This enabled the simultaneous detection of mRNA and specific target proteins, in a study that measured the change in expression levels and localisation of the presynaptic proteins synaptobrevin, synaptotagmin and synaptophysin in primary culture neurons (Zhang et al. 2014). STED has also been applied in the high resolution imaging of axons in cultured rat neurons, revealing the spatial organisation and symmetry of actin in live cells (Lukinavičius et al. 2014).

### Super-resolution optical fluctuation imaging (SOFI)

Super-resolution optical fluctuation imaging (SOFI) is an imaging technique, which in contrast to STED and PALM/STORM, does not rely on photoswitching or photoactivation of fluorophores. Instead SOFI enables the deconvolution of individual stochastic fluorescent fluctuations regardless of neighbouring fluorophores, which may contribute to overlapping diffraction patterns; this could be colour changes, brightening or dimming of the fluorophore or changes in polarisation (Dertinger et al. 2009). Application of the SOFI algorithm results in decrease of the point spread function (PSF) by isolating each individual peak of fluorescence emission, therefore improving overall resolution, which can be applied to video data and used to compile a movie, in order to identify protein localisation in a live cell system. A similar approach, which allows live cell imaging, is the use of algorithms such as Bayesian localisation microscopy, to resolve cellular structures; this can offer an achievable resolution of ~50 nm, using wide-field fluorescence microscopy (Cox et al. 2012). Both of these techniques rely on analysis of a time-sequence acquired using a very short exposure, so they depend on modern high speed, high sensitivity cameras in the same way as PALM and STORM.

These developments have greatly improved the achievable resolution of optical microscopy, although it is still necessary to use fluorescence microscopy in conjunction with EM in order to link live cell dynamics and function to ultrastructural organisation. The SRM techniques discussed above each have specific benefits for high resolution imaging of biological samples, although none can readily create a SRM image of ~20 nm resolution with fast image acquisition. To overcome these limitations EM is often still required.

### 1.6 Electron microscopy in bioimaging.

Electron microscopy has been used for many decades to achieve an increased resolution of ~2 nm, revealing fine detailed images of cellular ultrastructure. Imaging this detail with clarity is important in the study of the role of actin in intracellular organisation: such as how the structural organisation of the presynaptic terminal is related to the dynamic function of synaptic vesicles (Bloom et al. 2003).

Despite advances in light microscopy that increase the resolution achievable, EM is still the best technique for studying neuronal processes and producing detailed images which identify individual structures in neuronal circuits, such as synaptic connections (Anderson et al. 1994). Whilst EM techniques allow insight into the ultrastructural arrangement, the sample processing required is not always desirable and can result in various artefacts. Firstly, fixation, depending on the technique used, can result in the loss or redistribution of soluble proteins (Melan and Sluder 1992; Schnell et al. 2012). Secondly, the process of sample dehydration results in shrinkage and loss of the original live cell state, so protein localisation cannot be directly compared to that determined by live cell fluorescence microscopy studies (Gusnard & Kirschner 1977). Thirdly, for imaging by transmission electron microscopy, the resin embedded samples must be sectioned to produce 70 nm ultrathin sections; this means that only a small 'representative' area of the cell is imaged, which may not be a true representation of the whole cell.

Ultrathin sectioning of resin embedded samples results in a snapshot of the cellular environment (Shepherd & Harris 1998). TEM has advantages, in comparison to SEM, in that high voltages may be used to achieve high signal to noise in thin samples without a high degree of sample damage, such as structural deterioration through charging of the sample. Disadvantages include the requirement for the use of heavy metal stains, such as Osmium Tetroxide and Uranyl Acetate, in order to create contrast between intracellular structures. Immunolabelling with colloidal gold is a useful tool in the labelling of specific proteins for imaging by TEM. Modern adaptations of TEM include serial tomography. This method involves imaging serial sections to produce a 3-dimensional reconstruction of the ultrastructure throughout the whole sample. This is a challenging and laborious procedure and factors, such as electron beam damage, stain contamination or inhomogeneous sectioning, may hinder the production of a complete and non-distorted stack. Tomography may also be carried out on samples where SEM images are collected following sectioning of a sample block. This enables the high-resolution imaging of the sample surface; advantages of this technique include imaging of large sample areas and imaging at lower voltages, resulting in less sample damage. Each of these methods will be discussed in the following sections.

The resolution gained by TEM has been instrumental in the study of protein function and interactions during neuronal stimulation. Synapsin isoforms I and II have been linked to the regulation of synaptic vesicle endocytosis and delivery in active zones through interaction of synapsins and actin filaments in the presynaptic terminal.

Dephospho-synapsin polymerises actin and may create cross-linking between vesicles and actin, thus acting to maintain vesicle clusters. Dephosphorylation, regulated by $Ca^{2+}$ results in the loss of affinity of synapsin for vesicles, whereas phosphorylation increases affinity and promotes synapsin interaction with vesicles (Hirokawa 1989, Greengard et al. 1993).

### 1.7 Correlative light and electron microscopy

Live cell dynamics can be imaged by fluorescence microscopy, at a resolution of ~250 nm. SRM techniques can increase the resolution to ~20 -40 nm, although this is seldom achieved in SRM techniques using live cells; a resolution closer to 100 nm is more frequently quoted. The SRM techniques suffer from poor temporal resolution, and although strategies to improve time resolution are coming to the fore, they are still not ideal for live cell imaging. Although these techniques may increase the achievable resolution, it is not common, as with conventional fluorescence microscopy, to achieve direct correlation between SRM fluorescence images and EM images. As a result separate protocols have been created for samples imaged by each method, which give some insight into the relation between cellular structure and function, but remain un-correlated.

The development of correlative light and electron microscopy (CLEM) techniques has bridged the gap between cellular function and protein dynamics, by combining visualisation of targeted fluorescent proteins by fluorescence light microscopy (FLM), with high resolution imaging of cellular structure by EM. This may be achieved through a variety of biological imaging methods, ideally achieving direct correlation of the two data sets in one sample.

Method development to date has focussed on two pathways; either the preparation of samples that will be imaged primarily by FLM, by application of a method that allows conversion of fluorescence to electron dense material, or the preparation of samples for EM, using a probe that is visible by both FLM and EM. More recent developments have focussed on the integration of fluorescence and electron microscopes in one instrument (Liv et al. 2013; Zonnevylle et al. 2013).

Probes have been developed which enable correlation between fluorescence microscopy and EM by undergoing chemical conversion to convert fluorescence signal to electron dense material. Typically, use of these probes involves the photoconversion of fluorescent dyes with diaminobenzidine (DAB) (Deerinck et al. 1994). A separate approach in attaining correlation of light microscopy and EM is the use of probes which can be observed by both imaging methods, such as quantum dot labelling of FLAsH and ReASH tags added to protein targets (Adams et al. 2002; Gaietta et al. 2002). MiniSOG (mini singlet oxygen generator) is also an important technique involving genetic engineering of the native protein phototrophin-2 (Shu et al. 2011). This probe may be used to produce fluorescence images but also enables photoconversion of the singlet probe through light stimulated excitation of miniSOG to create an electron dense material visible by EM (Shu et al. 2011).

### Immunocytochemistry for use in CLEM - FluoroNanoGold and hybrid labelling

To enable detection of a probe by both microscopes requires the probe to be pre-embedded in the sample during sample processing. This may be achieved through various methods at different stages of processing. Hybrid labelling systems developed to enable CLEM emerged in the form of the conjugation of GFP with immunogold cluster compounds, such as FluoroNanoGold (FNG) (Nanoprobes) (Cheutin et al. 2007). These cluster compounds are an alternative to colloidal gold. Cluster compounds may be synthesized with a defined size, via the deposition of individual gold atoms to create a cluster of gold particles, which may have a diameter of less than 1 nm. Colloidal gold particle sizes may vary as the size of these clusters is determined by aggregation of colloidal gold in solution through chemical reduction. As this synthesis method is less directed than the formation of gold clusters the diameter of colloidal gold aggregates may vary (Mingos 2014). Each gold cluster may be functionalised to enable use in biological research; this includes the attachment of  monolayers (alkanethiolate) (Templeton et al. 2000) and antibodies to the particles (Zhou et al. 2009). The attachment of antibodies along with fluorophores has enabled the use of nanogold clusters in biological research (Thomas & Kamat 2003). It is observed that fluorescence is diminished in the presence of colloidal gold due to quenching, although if the fluorophore is spaced far enough away from the gold quenching is minimised (Albrecht et al. 1989; Powell et al. 1997; Powell et al. 1998) and as reviewed by Chevrier et al. (2012).

Biological samples are often prepared by thin sectioning at low temperatures. Human tissue samples have been prepared by sectioning on a ultramicrotome and labelled with fluoronanogold (FNG) (Robinson and Takizawa 2009). Although this is a versatile method that allows both fluorescence and electron microscopy, it has remained limited to fixed cells only, due to the requirement for chemical enhancement of the Nanogold to amplify signal for visualisation in ultra-thin sections. The thickness of the sample sections also results in out of focus fluorescence; even when semi-thin sections are obtained the improvement is not great enough to resolve separate cellular structures (Takizawa et al. 1998; Takizawa & Robinson 2000). Development of the tetracysteine-ReAsH system by the Tsien group provided an alternative labelling system with more flexibility for use in CLEM. This is a tetracysteine tag, containing the binding motif Cys-Cys-Pro-Gly-Cys-Cys, which may be genetically fused with target proteins; the tag may then bind with membrane permeable, bi–arsenical derivatives of fluorescein (e.g. ReAsH-EDT2, a red derivative) (Griffin et al. 1998; Adams & Tsien 2008). The fluorescent marker is incubated with DAB, then reacts with the osmium fixation to form electron dense material and easily visualised by EM.

### Quantum Dots

An alternative labelling method for CLEM is the use of Quantum dots (Qdots). These are electron dense non-genetically encoded probes, synthesised from semi-conductor materials (Ekimov et al. 1985), which produce a variety of fluorescence emission wavelengths, commonly CdSe (460- 515 nm), InP (560 - 750 nm) and InAs (800– 1800 nm) (Murray et al. 1993). The emission wavelength is directly determined by the size of the Qdot (between 2- 6 nm), the smaller the Qdot the higher energy wavelength emitted; therefore the larger the Qdot the longer the wavelength emitted (Peng et al. 1998). The emission bandwidth is altered by the epitaxical growth of semi-conductor materials such as Indium arsenide (InAs), Indium phosphide (InP) and Cadmium selenide (CdSe) around the core of the Qdot to form a high band gap outer shell with discrete size dependent properties (Hines & Guyot-Sionnest 1996), as shown in Figure 1.8.1 and reviewed by Alivisatos A. P. 2005.

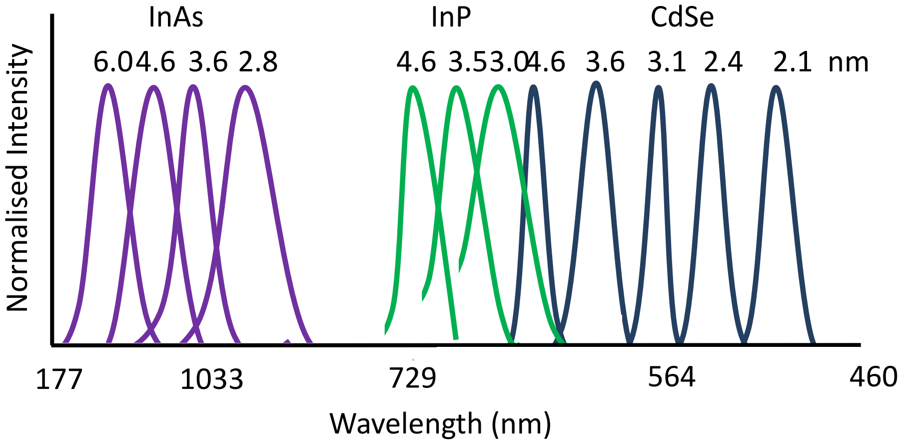

**Figure 1.8.1 Emission spectra and particle size of quantum dots.** Examples of wavelengths produced by semiconductor materials (InAs, InP and CdSe) used to create quantum dot shells. Each set of wavelength variations is also dependent on the diameter of the Quantum dot. Figure hand drawn, based on Alivisatos A.P. (2005).

Qdots have optical qualities superior in comparison to fluorescent proteins, such as broader excitation ranges, narrower emission bandwidths, longer fluorescence lifetimes and reduced photobleaching (Dahan et al. 2001). Negative aspects of using Qdots include the fact that they are prone to photoblinking, where the Qdots randomly alternate between emitting and not emitting fluorescent states. The large sizes and hydrophobic surface layer also means the Qdots are not easily used in live cell studies, although the development of hydrophilic biologically functional coatings has been shown to enable biological penetration and interaction with antibodies, which is significant for the application of Qdots for live cell fluorescence imaging and also for applications in CLEM, (Ballou et al. 2004;  Nisman et al. 2004) for example the study of endogenous proteins in the mapping of protein localisation (Giepmans et al. 2005).

## Cryofixation

Transmission electron microscopy (TEM) of biological samples enables high resolution imaging of ultra-thin sections, which may be aided by the use of finder coverslips. However during preparation for imaging by TEM the sample no longer retains a true representation of the live cell state. This is mainly due to the protocols involved in preparation of biological samples, such as chemical fixation with paraformaldehyde or gluteraldehyde, dehydration through an ethanol wash series and resin embedding along with heavy metal staining. Sample preparation may negatively affect the clear imaging of ultrastructural detail as this may result in the addition of artefacts.

Alternatives to chemical fixation include cryo-fixation and high pressure freezing (HFP) (Verkade 2008), both of which are applied with the aim of preserving the cellular ultrastructure in thick samples, thus maintaining the native biological state (Studer et al. 2008). This method may be advantageous as rapid cooling of water within samples results in the formation of water crystals smaller than ~5 nm, allowing high resolution imaging to take place without the presence of artefacts. HPF is achieved by freezing samples with liquid nitrogen under high pressure (~2,000 bars). This method enables fixation of samples up to 200µm in thickness (Studer et al. 2008). Cryo-fixation involves the removal of heat from water to form amorphous vitreous ice, the rapid cooling results in the solidification of the ice and rapid (within milliseconds) immobilisation of cell molecules (Moor 1987). This is classically followed by freeze substitution, where all water content is substituted by solvents such as acetone or methanol, dehydrating the sample, yet maintaining the frozen hydrated state (Bohrmann & Kellenberger 2001). This process occurs at approximately -40°C, where the thermal energy of proteins and lipids are low enough to prevent movement, further reducing the production of artefacts (Kellenberger 1987).

Recent research has demonstrated preservation of GFP fluorescence in resin embedded (Peddie et al. 2014) and plastic embedded samples (Watanabe et al. 2014). This was achieved in HeLa cells expressing GFP and mCherry; to maintain fluorescence through freeze substitution a shorter freeze substitution protocol was applied (McDonald & Webb 2011), which resulted in the preservation of fluorescence after freeze substitution and resin embedding. This enabled the visualisation of fluorescence in direct correlation with high resolution imaging by TEM, although it must be noted that it was not possible to precisely localise the fluorescence to one particular organelle (Peddie et al. 2014). The accuracy of correlation is also affected because when imaging these samples by TEM, as with all samples in cryo-EM, the frozen hydrated sample must be sectioned at low temperature (-140°C) in a cryoultramicrotome. Imaging requires high quality interpretative skills, as despite removing artefacts usually caused by chemical addition, scratches from the sectioning knife and distortions remain (Dubochet et al. 2007). Also depth of imaging is low (<1µm) with low contrast difference generated between the sample and the surrounding ice. An alternative method was demonstrated in a study into the kinetics and localisation of LAMP-1 (Rijnsoever, Oorschot, and Klumperman 2008). This was a multistep process where cells are cultured on Formvar coated grids on coverslips, and primarily imaged by FLM. The samples are then fixed and resin embedded, allowing specific areas of the coverslip to be mapped and the identified for sectioning and imaging by TEM. An alternative method of direct correlation of fluorescence with TEM ultrathin sections is by the application of integrated light and electron microscopy (iLEM), developed by FEI. This method involves the use of an LED based wide-field fluorescence microscope which is situated in the sample holder of a TEM column. By this imaging method fluorescence and electron microscopy may be perform sequentially without movement of the sample (Faas et al. 2013).

These methods allow the successful correlation between FLM and EM and enable the correlation of live cell dynamics with high resolution snapshot imaging, although each process involves laborious protocols which are relatively low throughput in both volume and sample number. Other caveats include the fact that samples are required to undergo ultra-thin sectioning for imaging by TEM and SEM, thus only a small representative area of the cellular structure is imaged. To improve on this electron tomography and 3D electron tomography may be used to acquire high resolution images of the serial sections throughout a sample in order to computationally reconstruct a full picture of the original sample (McIntosh et al. 2005). Advances in these applications have led to the development of various CLEM methods including cryo –electron tomography (cryo-ET), as reported by Plitzko, Rigort, and Leis (2009). This method results in the accurate preservation of cellular architecture by obtaining frozen hydrated samples through thin film plunge freezing and high pressure freezing in conjunction with cryo-sectioning (Dubochet et al. 1988). This protocol enables the acquisition of TEM images; as each of these are of frozen hydrated samples the electron beam exposure must remain low, to reduce damage. In addition to this, because the biological sample cannot be stained by conventional EM methods, the contrast is low. Following acquisition of a series of images with different orientations, a tomographic reconstruction of the sample may be achieved. Although tomography reveals a high resolution reconstruction of the hydrated state sample, the true extent of cellular features imaged within the processed sample, which may create additional background contrast, which may ultimately hinder the identification of target proteins (Ellis 2001).

In order to overcome problems in maintaining fluorescence in embedded samples, methods have been developed where the FLM is conducted prior to fixation and EM. This method has significant advantages as the fluorescence of target proteins in a biological sample is acquired by live cell imaging, therefore demonstrating the true live cell dynamic. This technique enables the capture of live cell events by fluorescence for direct correlation by high resolution EM imaging, by rapid transfer cryo-fixation within 4 seconds of initial FLM (Verkade 2008). As cryo-fixation removes the need for fixative, the ‘live-state’ of the sample is maintained, allowing preservation of the ultrastructure and best correlation with fluorescence localisation. TEM can also permit 3D imaging and has now been commercialised with 3D tomography that permits fluorescence imaging of stained sections. This is achieved through the imaging of multiple sections and gathering information from various set angles, this information may then be processed through commercial computational algorithms to enable the reconstruction of a 3 dimensional image; as reviewed by Midgley & Weyland (2003) this imaging method may be very profitable when used in conjunction with optical fluorescence techniques (Braet et al. 2014; Kopek et al. 2012).

### Focussed Ion Beam/ Serial block face

To overcome some of the limitations of CLEM using TEM, methods have been developed such as the application of scanning electron microscopy (SEM) in conjunction with milling of rapidly frozen close to 'live state' cryo-EM samples, enabling imaging of thin cell sections from deep within the sample (Rigort et al. 2012). Serial block face (SBF) (Denk & Horstmann 2004) and FIB microscopy (Orloff et al. 1996) are powerful techniques for the acquisition of images from serial sample sections. SBF is an SEM based imaging technique, where a focused electron beam is scanned across the surface of a sample with the image formed by collection of backscattered electrons by a detector above the sample. The removal of material through milling with a gallium ion beam results in incremental removal of material ranging between 20 nm and 100 µm in depth. Here, the milling beam lies parallel to the imaging beam, allowing imaging of the milled region (Heymann et al. 2006; Knott et al. 2008). In the case of SBF this may be achieved by the integration of a microtome within the SEM vacuum chamber. These imaging techniques produce serial images throughout the whole of the sample. This may then be realigned computationally to reconstruct a 3D image, revealing high resolution detail of ultrastructure in the sample (Bushby et al. 2012). FIB and cryo-soft X-ray microscopy have recently been combined in the development of CLEM techniques, where fluorescence may be localised within the high resolution reconstruction (Peddie & Collinson 2014). SBEM has been instrumental in revealing detailed information in complex structures (Denk & Horstmann 2004). In a study by Wilke et al. (2013) SBEM was used to image synapse formation and organisation in hippocampal mossy fibre terminal. This revealed an increase in presynaptic and postsynaptic connections following the association of mossy fibre boutons with dendritic protrusions. This shows the value of a combined imaging approach in the ability to gain detailed information from complex samples.

## 1.8 The development of correlative microscopy techniques

Correlative microscopy techniques have enabled the combination of various fluorescence and electron microscopy techniques to achieve high resolution with the ability to probe live cell dynamics. This is helping further our understanding of ultrastructural rearrangements, protein interactions and vesicle recycling during synaptic activity. A large range of applications are becoming available, but most rely on the sample being presented within the vacuum chamber. There is significant interest in the development of applications to enable correlative light and electron microscopy where the sample remains in a hydrated state during each imaging stage. These include development of specialised membranes for the presentation of unprocessed samples for TEM imaging, systems to image biological samples at atmospheric pressure and the integration of both light and electron microscopes into one instrument.

### Correlative light and electron microscopy in hydrated samples.

CLEM is now at the forefront of the study of cellular structure and function due the coupling of live cell fluorescence microscopy with the fine detail of high resolution electron microscopy (Sartori et al. 2007). Recent developments in electron microscopy have enabled the study of hydrated biological samples at high resolution whilst maintained at atmospheric pressure. For example, biological samples have been successfully imaged in enclosed capsules, which maintain atmospheric pressure under vacuum. A disadvantage of this method is the small sample volumes involved (Katz et al. 2007) and (Thiberge et al. 2004). The development of atmospheric scanning electron microscopy has enabled the observation of biological samples in an open chamber dish (Murai et al. 2011 and 2013). This is advantageous to the study of biological samples as it enables the visualisation of three dimensional cellular processes in aqueous environment by ASEM, many of which may be directly correlated to fluorescence microscopy.

Quantomix capsules are a purpose built capsule in which samples may be cultured and imaged whilst remaining in culture. The capsule may be sealed prior to imaging to form a chamber which remains at atmospheric pressure. This protects the sample whilst imaged by SEM under vacuum. The sample is imaged through the underside of a light and electron permeable grid window, which is a thin (typically around 100 nm) polyimide membrane, on which the sample is cultured (as shown in Figure 1.9.1). This also means that fluorescence microscopy may be conducted on the sample prior to SEM, although this must be performed after fixation and labelling for SEM, therefore losing the benefits of TEM imaging.

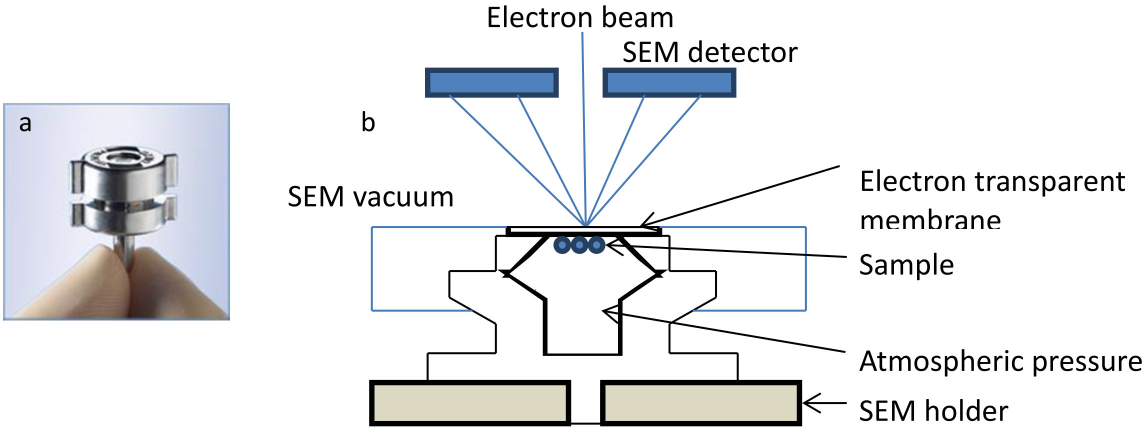

**Figure 1.9.1 Quantomix capsule.** a) example of a sealed Quantomix capsule (image provided by Quantomix Ltd). b) Schematic of a Quantomix capsule within an SEM, enabling imaging of a sample at atmospheric pressure. Figure hand drawn, based on Dyab & Paunov (2010).

Samples can be imaged by light microscopy before insertion in the SEM chamber, although the sample cannot be further manipulated. The design of the standard SEM vacuum chamber allowed the development of integrated light and electron microscopy systems following the installation of the objective lens below the sample, with the SEM sitting above the sample. This approach has been exploited by Kanemaru et al. 2009, Zonnevylle et al. 2013 and Delmic (Delft, Netherlands). The latter has taken this one step further by introducing a flow chamber that permits the sample to be manipulated whilst in the SEM chamber.

A major advance in CLEM methods is the development of a system by Liv et al. (2014) for correlative FLM and SEM of biomarkers in liquid. This was achieved by holding the sample liquid between a coverslip and silicon nitride film. FLM is performed from below the sample though the coverslip; SEM is performed from above the sample, through the silicon nitride film window, which is electron permeable whilst maintaining a vacuum.

A similar approach is demonstrated by the JEOL ClairScope; a novel technology which allows imaging of the same hydrated sample in situ by fluorescence and scanning electron microscopy at atmospheric pressure (Suga et al. 2011; Nishiyama et al. 2014a). The development of atmospheric scanning electron microscopy (ASEM) has enabled the observation of biological samples in an open chamber dish (Nishiyama et al. 2010; Murai et al. 2011 and 2013). This is possible due to the design of the technology which incorporates light microscopy and an SEM in the same machine, allowing in-situ dual microscopy. Biological cell samples may be cultured in a special petri dish, under normal culture conditions and retained in culture media throughout imaging. The petri dish contains a central silicon nitride window over which the sample is cultured; this window is 250 µm square and 100 nm in thickness (Figure 1.10.1a). This window provides an inert silicon oxide base, similar to glass. The silicon nitride film also acts as an electron permeable window which simultaneously maintains a vacuum below the sample, enabling *in situ* atmospheric scanning electron microscopy (ASEM) of the same hydrated sample by detection of back scattered electrons from the sample (panel e), while also allowing imaging from above by wide field fluorescence microscopy; Figure 1.10.1b (Suga et al. 2011; Morrison et al. (2012); Nishiyama et al. 2014). Therefore, once inserted into the ClairScope the dish allows observation of live cell fluorescence from above by wide field optical microscopy which can be directly correlated with high resolution SEM imaging of specific fluorescently labelled targets in a three dimensional hydrated cell sample. ASEM images are created though detection of backscattered electrons; the electron beam passes through the film window into the hydrated sample.

Electrons that come into contact with the sample are deflected back through the film window and are detected by a detector situated below the sample window; Figure 1.10.1.

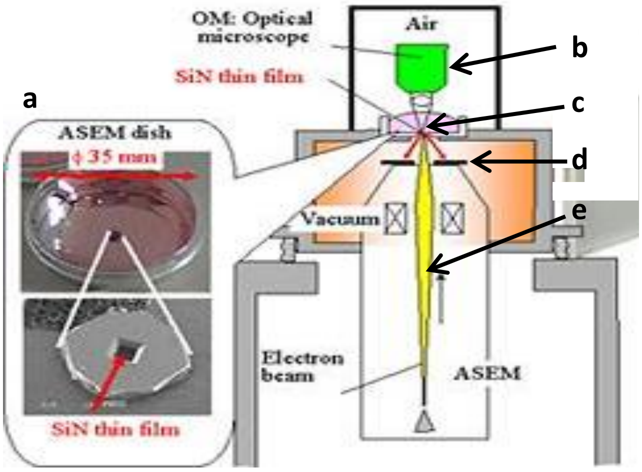

**Figure 1.10.1. JEOL ClairScope.** Directly correlative light and scanning electron microscopy by atmospheric scanning electron microscopy (ASEM). a) Specialised petri dish containing 100 nm thick silicon nitride (SiN) film window. b) Upright optical microscope above sample in petri dish. c) biological sample in culture medium. d) Backscattered electron detectors. e) Inverted SEM electron beam in vacuum chamber. (Image provided by JEOL)

This technology has been successfully used in the study of biological samples as it enables the visualisation of cellular dynamics in aqueous environment by ASEM at high resolution in a study by Nishiyama et al. (2010). Here, COS7 cell surface glycans were labelled with 15 nm WGA- colloidal gold conjugates, revealing an ‘achievable’ resolution of 8 nm, measured between two gold particles. This novel system has been used by a number of research groups to investigate biological processes, including the study of mycoplasma (Sato et al. 2012), the cytoskeleton and chaperone proteins in the endoplasmic reticulum (Maruyama, et al. 2012a), cell surface microvilli and cell adhesion (Murai et al. 2013), neuronal differentiation, proplatelet-formation and phagocytosis (Hirano et al. 2014) cell filopodia and flagella (Nishiyama et al. 2014b), neuronal axonal partitioning in Drosophila, Rubella virus replication and clathrin internalisation in primitive endoderm cells (Kinoshita et al. 2014) during cancer diagnosis (Memtily et al. 2015). Also fluorescently labelled neurons have been studied, to visualise the localisation of nuclei by fluorescence microscopy and ASEM, following heavy metal staining (Ebihara et al. 2015). Other studies have investigated the radiation-induced self-organisation of inorganic solder (non-biological) particles (Suga et al. 2011) and also crystal formation by lysozymes, lipase B and histone chaperones in crystallisation buffers (Maruyama, et al. 2012b).

Correlative light and electron microscopy is now at the forefront of the study of cellular structure and function due the coupling of live cell dynamics of fluorescence microscopy with the fine detail of high resolution electron microscopy (Sartori et al. 2007).

This project focusses on the adaptation of simple immunofluorescence labelling methods with the aim of developing an electron SRM (eSRM) approach, combining the benefits of SRM with the high-resolution imaging of electron microscopy. The project will investigate the localisation of vesicles and target proteins in differentiated B104 neuroblastoma cells in relation to cell structure by ASEM using the novel JEOL ClairScope imaging technology. This approach to studying vesicle and protein dynamics will be a good model system as a wealth of research into vesicle dynamics using fluorescence microscopy and electron microscopy already exists, and can therefore be used for benchmarking this novel correlative imaging system. This may provide a novel perspective in correlating light and electron microscopy, which is particularly important in the study of vesicle recycling and protein dynamics in neuronal- like cells such as neuroblastoma cells. These provide a stable cell line which can be utilised to develop imaging techniques that may be applied to the imaging of such systems in primary neuronal cultures and therefore show new insight into the cellular dynamics involved in learning and memory.

The aim of the first results chapter is to develop a robust and reproducible imaging method using simple immunogold labelling and to define the imaging conditions required for optimal image acquisition using the JEOL ClairScope. The second results chapter describes the work done to apply the labelling techniques and image optimisation developed in Chapter 3. This focusses in particular on the application of these novel techniques with the aim of identifying vesicle pools within differentiated B104 neuroblastoma cells which have undergone active recycling through chemical stimulation. The third results chapter investigates the role and localisation of PKA regulatory subunits during the differentiation of B104 neuroblastoma cells by SRM techniques in fluorescence microscopy will also be investigated by the application the developed labelling and imaging protocols.

## 2.0 Materials and Methods

### 2.1 Materials.

**Bovine serum albumin.** Sigma. Ref: 05482-100 g

**Dibutyryl-cAMP (dib-cAMP).** Biolog Lifescience Institute. Ref: D009-100

**Dimethylsulfoxide (DMSO).** Fisher Scientific**.** Ref: D/4121/PB08

**Dulbecco's Modified Eagle Medium (DMEM)**. Gibco/ Life Technologies. Ref: 41966029

**DMEM (Complete).** DMEM containing 1 % Penicillin (v/v) / 1 % Streptomycin (v/v) and 10 % Foetal Bovine Serum (v/v)

**EcoTransfect**. Oz Biosciences. Ref: ET11000

**Foetal Bovine Serum.** Mycoplex. Ref: A15-105

**LB Agar.** (1000 ml) (10 g NaCl, 10 g Tryptone, 5 g Yeast Extract, 20 g Agar)

**LB Medium.** (1000 ml) (10 g NaCl, 10 g Tryptone, 5 g Yeast Extract)

**Phosphate Buffered Saline.** (10x Stock) (440 g NaCl, 10 g KCl, 72 g $Na_2HPO_4$, 12 g $KH_2PO_4$, in 5 L UP $H_20$, pH 7.4)

**Paraformaldehyde (PFA).** Fisons Scientific Equipment. Lot: P/0840/53. Ref: 27352062 (4 g PFA, 200 ml dH2O. 1 M NaOH. 50 ml 2x PBS. 4 g sucrose, pH 7.4.)

**Penicillin /Streptomycin.** Gibco/ Life Technologies. Ref: 15140-122

**Rhodamine phalloidin.** Biotium. Cat: 00027

**Stable diaminobenzidine (DAB).** Invitrogen. Cat: 750118

**SynaptoRed™ C2.** Sigma. Product Ref: 6689 CAS: 162112-35-8. 10 mg $mL^{-1}$

**TritonX-100.** Sigma. CAS 9002-93-1.

**Trypsin/EDTA.** Gibco. R001100

**Type 2 Ultra pure water (UP $H_20$)**. PureLab Option. ELGA DV35. Resistivity 18 MΩ.cm (0.055 µS/cm)

| Antibody | 1° | Host Species | Isotype | Specificity | Manufacturer/ Reference N°.<br>Stock concentration | Working Dilution | Applications |
|---|---|---|---|---|---|---|---|
| GFP | 1° | Mouse | Monoclonal<br>3E6, IgG$_{2a}$ | GFP | Invitrogen<br>A-11120<br>100 µg (200 µg mL$^{-1}$) | 1:1000 | IF, ASEM |
| GFP | 1° | Rabbit | Monoclonal<br>IgG | GFP | Jack Fransen<br>*Radboud umc, Netherlands | 1:1000 | IF, ASEM |
| Actin | 1° | Mouse | Monoclonal<br>IgG1 | Actin | Abcam<br>(ACTN05 (C4)) ab3280<br>0.5 ml at 0.2 mg mL$^{-1}$ | 1:1000 | IF, ASEM |
| FLAG | 1° | Mouse | Monoclonal<br>IgG1 | FLAG | Sigma<br>F1804-1MG. 50 µg<br>(1 mg mL$^{-1}$) | 1:1000 | IF, ASEM |
| RIα | 1° | Mouse | Monoclonal<br>IgG2b | Mouse PKA (RI) subunit. Aa 225-381 | BD Transduction labs 610669<br>50 µg (250 µg mL$^{-1}$) | 1:1000 | IF |
| AKAP 149 | 1° | Mouse | IgG1 | AKAP 149 | BD Transduction labs 610720<br>50 µg (250 µg mL$^{-1}$) | 1:1000 | IF |
| AKAP 220 | 1° | Mouse | IgG1 | AKAP 220 | BD Transduction labs 610704<br>50 µg (250 µg mL$^{-1}$) | 1:1000 | IF, ASEM |

Refs: *Jack Fransen, Institute for Molecular Life Sciences, Radboud umc, Nijmegen, The Netherlands. http://www.rimls.nl/people/f/fransen/

**Table 2.1 Primary antibodies.** Detailing isotype, specificity, working concentration and manufacturer. Immunofluorescence (IF). Atmospheric scanning electron microscopy (ASEM). Antibody names stated are used throughout thesis.

| Antibody | 2° | Host Species | Isotype | Specificity | Manufacturer/ Reference N°.<br>Stock concentration | Working Dilution | Application |
|---|---|---|---|---|---|---|---|
| Mouse 594 | 2° | Goat | Polyclonal<br>IgG H+L | Mouse | Invitrogen A-11005. 0.5 ml | 1:500 | IF |
| Rabbit 594 | 2° | Goat | Polyclonal<br>IgG H+L | Rabbit | Invitrogen A-11012. 0.5 ml | 1:500 | IF |
| Mouse 488 | 2° | Goat | Polyclonal<br>IgG H+L | Mouse | Invitrogen A-11029. 0.5 ml | 1:500 | IF |
| 20 nm Gold | 2° | Goat | Polyclonal<br>IgG H+L | Mouse | Abcam ab27242<br>500 µl at 0.015 mg $mL^{-1}$ | 1: 5 | ASEM |
| 15 nm Gold | 2° | Goat | Polyclonal<br>IgG H+L | Mouse | Abcam ab27236<br>500 µl at 0.019 mg $mL^{-1}$ | 1: 5 | ASEM |
| 1.4 nm Gold | 2° | Goat | Polyclonal<br>IgG | Mouse | Nanoprobes<br>2002. 80 µg $mL^{-1}$** | 1:4 | ASEM |

**Table 2.2 Secondary antibodies.** Detailing isotype, specificity, working concentration and manufacturer. Immunofluorescence (IF). Atmospheric scanning electron microscopy (ASEM). Antibody names stated are used throughout thesis. Antibody names stated are used throughout thesis. **Stated in references

## 2.2 Methods

### 2.2.1 Molecular Biology Protocols

**Preparation and application of 4 %** (w/v) **Paraformaldehyde/ 4 %** (w/v) **Sucrose**

In all cases where cell samples were fixed, 200 µl of a solution of 4 % paraformaldehyde/ 4 % sucrose (4 % (w/v) PFA/ 4% (w/v) sucrose) was used. The fixative solution components and PBS buffer are listed in the Section 2.1. Sample fixation was conducted for 20 min at room temperature (18 °C).

### 2.2.2 Bacterial transformation

DNA plasmids were transformed into competent *Escherichia coli* (*E. coli*) strain XL-10 for all DNA expression steps (Table 2.3). 1 ng of purified plasmid was added to 50 µl *E. coli* and incubated on ice for 15- 30 min. Heat shock was carried out for 45 s at 42 °C followed by incubation on ice for 2 min. 400 µl LB media was added and the mixture was incubated at 37 °C in a shaking incubator at 200 revolutions per min (rpm) for 1 h. 100 µl of the culture was then plated on an agar plate containing appropriate selective antibiotics and incubated at 37 °C overnight as specified in Table 2.3.

| **Plasmid** | **Construct name** | **Abbreviated Names** | **Vector details** | **Insert details** | **Resistance** | **Transfection conc.** |
|---|---|---|---|---|---|---|
| Synapto-pHluorin | pCI-super ecliptic Synapto-pHluorin | (pCI)<br>Synapto-phluorin | pCI | super ecliptic Synapto-pHluorin | Ampicillin | 1 µg mL$^{-1}$<br>1 µg mL$^{-1}$ |
| IP-1 CFP | pmCer-C1-iPRI | Cerulean plasmid (pm Cer) (CFP)<br>*iPRI (IP-I) | pmCer-C1 | iPRI | Kanamycin | 1 µg mL$^{-1}$ |
| GFP actin | GFP-Actin | Green fluorescent protein (GFP)<br>Actin | GFP | Actin | Kanamycin | 1 µg mL$^{-1}$ |
| RIα CFP | pmCer-RIa | Cerulean plasmid – N1 terminal (pmCer- N1)<br>**PKA RIα (RIα) | pmCer-N1 | RIa | Kanamycin | 1 µg mL$^{-1}$ |
| RIα FLAG | pFLAG-N1-RIa | FLAG plasmid – N1 terminal (pFLAG)<br>**PKA RIα (RIα) | pFLAG-N1 | RIa | Kanamycin | 1 µg mL$^{-1}$ |

**Table 2.3. List of plasmids utilised for transfections.** Plasmid construct, vector and insert details of plasmids used. *Inhibitory Peptide 1 (IP-1); Cerulean is quoted as (Cer) as vector name and (CFP) as fluorescent protein throughout thesis; **Protein kinase A regulatory subunit RIα stated as (PKA RIα) throughout thesis. All plasmids were synthesised and confirmed by PCR sequencing, in-house by Evans lab.

### 2.2.4 Plasmid purification

Plasmid DNA was purified from transformed *E. coli* cultures. Single colonies were selected and incubated at 37 °C overnight in 100 µl LB. Plasmid DNA was purified using a Nucleobond, Xtra midi Plus, nucleic acid and protein purification kit (Qiagen). DNA was eluted in 10 mM Tris (pH 7.4) and stored at -20°C. DNA quantification was carried out using a Nanodrop, (Thermo Scientific) measuring absorbance at 260 nm. Quality control of all purified DNA was performed by testing for specific molecular weights on agarose gels.

## 2.3 Cell Culture Methods

### 2.3.1 B104 neuroblastoma and U251 glioblastoma cell culture

B104 neuroblastoma (sourced from Evans lab) and U251 glioblastoma cell lines (provided by Jack Fransen, Radboud UMC, Netherlands) were maintained in 25 $cm^2$ or 75 $cm^2$ flasks, cultured in complete DMEM at 37 °C in a humidified atmosphere containing 5.2 % $CO_2$ with 1 % Penicillin (10,000 U/ $mL^{-1}$)/ Streptomycin (10,000 µg/ $mL^{-1}$). The cultures was passaged and split 1:3 when confluent. Cells were detached from the culture flask with 1 ml of 1 % Trypsin/ EDTA (pre-warmed to 37 °C), this action being stopped by addition of culture medium. Cells were centrifuged at 18 °C at 133 xg for 3 min to form a pellet. Supernatant was discarded and the pellet resuspended in 1 ml complete DMEM. For plating the cells were counted using a haemocytometer and seeded at a density of 2 x $10^4$ per 13 mm circular glass coverslip in a 24 well plate. Coverslips were sterilised in an oven at 190 °C. Differentiation of neuroblastoma cells was achieved by 4 day culture in complete DMEM in the presence of 1 mM dib-cAMP (stock concentration 100mM in 1 ml UP H20) at 37 °C in a humidified atmosphere containing 5.2 % $CO_2$.

### 2.3.2 Transient transfection of B104 neuroblastoma cells

B104 neuroblastoma cells were plated at the desired density as previously described and cultured in complete DMEM at 37 °C in a humidified atmosphere containing 5.2 % $CO_2$. After 24 h cells were transfected using EcoTransfect (Oz Biosciences) according to the manufacturer's instructions. Single transfections were carried out using 1 µg plasmid DNA with 2 µl transfection agent in each 50 µl DMEM. Double transfections were carried out using 1 µg of each plasmid and 4 µl transfection reagent. Each solution was mixed and incubated at room temperature (18 °C) for 15 min before pipetting into 500 µl complete DMEM in each well of a 24 well plate and incubated at 37 °C in a humidified atmosphere containing 5.2 % $CO_2$. For all experiments cells were transfected for 8 h.

### 2.3.3 Immunocytochemistry

Transfected cells were cultured in 24 well plates in complete DMEM at 37 °C in a humidified atmosphere containing 5.2 % $CO_2$. Culture medium was removed and cells washed 3 times in phosphate buffered saline (PBS) by addition and immediate, complete aspiration of 200 µl PBS. This was followed by fixation in 4 % (w/v) paraformaldehyde (PFA) 4 % (w/v) sucrose for 20 min at room temperature (18 °C). Cells were washed and blocked with 1 % (w/v) Bovine Serum Albumin (BSA) in PBS. Cells were permeabilised with 1 % (v/v) Triton X-100 in PBS for 10 min followed by washing and blocking with 1 % (w/v) BSA in PBS for 30 min. Primary antibodies were applied in 1 % (w/v) BSA in PBS for 2 h at 37 °C in a humidified atmosphere. Working concentrations and specificity are shown in Table 2.2. Fluorescently conjugated secondary antibody specific for the primary antibody host species was then applied in 1 % (w/v) BSA in PBS in the dark for 1 h at concentrations shown in Table 2.2. Initial labelling experiments were carried out over varying antibody concentrations to establish the optimal working concentration. All samples were stained with 4'-6' diamidino-2-phenylindole (DAPI) at a dilution of 1:10 (stock concentration 1 µg $mL^{-1}$). Coverslips were then removed from the wells and washed 6 times in UP $H_20$ and mounted on microscope slides using Mowiol

(0.2 M Tris, pH 8.5, 12 % w/v Mowiol, 33.3 % w/v glycerol) and allowed to set overnight at 4 °C.

### 2.3.4 Immunogold labelling

Cells were cultured in complete DMEM at 37 °C in a humidified atmosphere containing 5.2 % $CO_2$ on ClairScope™ dishes. Culture media was removed and the cells washed 3 times in PBS by addition and immediate, complete aspiration of 200 µl PBS. This was followed by fixing with 4 % PFA (w/v) 4 % sucrose (w/v) for 20 min. Cells were permeabilised by incubation with 1 % TritonX-100 for 10 min, followed by 3 washes in PBS by addition and immediate, complete aspiration of 200 µl PBS. Primary anti-GFP antibody (stock concentration; 200 µg $mL^{-1}$) was applied at a dilution of 1:1000 for 1 h at 37 °C in a humid environment, followed by washing 3 times in PBS by addition and immediate, complete aspiration of 200 µl PBS. Secondary immunogold antibody (stock concentrations; 15 nm at 0.019 mg $mL^{-1}$ and 20 nm at 0.015 mg $mL^{-1}$) suspended in a solution of 1 % (w/v) Triton 1 % (w/v) BSA in PBS was added to the samples for 1 h at a dilution of 1:5. Samples were washed thoroughly 6 times with PBS by addition and immediate, complete aspiration of 200 µl PBS prior to imaging. The immunogold particles are covalently and specifically linked to goat IgG polyclonal secondary antibodies specific for mouse IgG (heavy and light chains) (Abcam).

### 2.3.5 1.4 nm Nanogold labelling and gold enhancement

Cells were cultured in complete DMEM at 37 °C in a humidified atmosphere containing 5.2 % $CO_2$ on ClairScope™ dishes. Culture media was removed and the cells washed 3 times in PBS by addition and immediate, complete aspiration of 200 µl PBS. This was followed by fixing with 4 % PFA (w/v) 4 % sucrose (w/v) for 20 min. Cells were permeabilised by incubation with 1 % TritonX-100 for 10 min, followed by 3 washes in PBS by addition and immediate, complete aspiration of 200 µl PBS. Primary anti-GFP antibody (stock concentration; 200 µg $mL^{-1}$) was applied at a dilution of 1:1000 for 1 h at 37 °C in a humid environment, followed by washing 3 times in PBS by addition and immediate, complete aspiration of 200 µl PBS. Secondary anti GFP Fab’ fragment 1.4 nm immunogold particles suspension was applied to the samples at a dilution of 1:4 (stock concentration 80 µg mL$^{-1}$) in 1 % (w/v) BSA in PBS and incubated at room temperature (18 °C). Samples were washed thoroughly 3 times for 5 min each with 1 % (w/v) BSA in PBS by addition and immediate, complete aspiration of 200 µl 1 % (w/v) BSA in PBS.

Gold enhancement of the Fab’ fragment 1.4 nm immunogold particles was achieved using GoldEnhance™ (Nanoprobes). Cells previously labelled with Fab’ fragment 1.4 nm immunogold particles were washed 3 times for 5 min each with UP $H_20$ by addition and immediate, complete aspiration of 200 µl UP $H_20$. The GoldEnhance™ solution was applied firstly as solution A, then B for 5 min, followed by solution C, then D, followed by incubation for 5 min. Samples were washed 6 times with UP $H_20$ by addition and immediate, complete aspiration of 200 µl UP $H_20$ prior to imaging,

### 2.3.6 FM 5-95 staining and imaging

Cells were cultured at a density of 2 x $10^4$ in 8 chambered coverslips (Labtek) in complete DMEM at 37 °C in a humidified atmosphere containing 5.2 % $CO_2$ and differentiated for 5 days by addition of 1 mM dib-cAMP on day 2 of culture. A 25 mM stock solution of FM 5-95 (SynaptoRed™ C2) was prepared in 71 µl pure DMSO (supplied at a concentration of 10 mg mL$^{-1}$) for use at a working concentration of 25µM. Stimulation of cellular endocytosis was induced by addition of the dye in 90 mM KCl buffer for 30 s. Termination of endocytosis was carried out by removal of the solution and washing with 500 µl PBS 6 times in PBS to remove extracellular FM dye. Cells were then fixed in 4 % PFA (w/v) 4 % sucrose (w/v) for 20 min, followed by washing 3 times in PBS by addition and immediate, complete aspiration of 200 µl 1 % (w/v) BSA in PBS.

Confocal fluorescence microscopy of cell samples stimulated in the presence of FM 5-95 on glass coverslips and also on ClairScope™ dishes was achieved by using a Zeiss 710 Confocal inverted microscope with a Plan- Apochromat 20x (NA 0.8) oil DIC lens. Fluorescence was excited using Argon ion laser at 594 nm with a 595 nm main beam splitter (MBS) excitation filter and fluorescence emission collected using a 605 – 740 nm bandpass emisson filter.

### 2.3.7 Actin microfilament staining with rhodamine phalloidin.

Cells were cultured in complete DMEM at 37 °C in a humidified atmosphere containing 5.2 % $CO_2$. The culture media was removed and cells fixed in 4 % PFA (w/v) 4 % sucrose (w/v) for 20 min, followed by washing 3 times in PBS by addition and immediate, complete aspiration of 200 µl PBS. Permeabilisation was achieved by incubation with 1 % (v/v) Triton X-100 in PBS for 20 min. Cells were washed by addition and immediate, complete aspiration of 200 µl PBS and blocked with 1 % (w/v) BSA in PBS by addition and immediate, complete aspiration of 200 µl 1 % (w/v) BSA in PBS. Rhodamine phalloidin (Biotium) was applied using 5 µl methanol diluted stock (6.6 µM) for every 20 µl DMEM, followed by incubation for 30 min at room temperature (18 °C) in the dark. Cells were washed 3 times by addition and immediate, complete aspiration of 200 µl PBS prior to imaging.

## 2.4. Imaging Techniques.

### 2.4.1 Atmospheric scanning electron microscopy

To obtain 3D resolution of the cells using the ClairScope™ dishes, samples were examined beforehand by confocal methods. Confocal fluorescence microscopy of synaptopHluorin containing cells on ClairScope™ dishes was achieved using a Zeiss 510 Confocal upright microscope with a 40x water dipping Achroplan 40x, (0.8NA) water objective. Fluorescent imaging was achieved using an Argon ion laser at 488 nm with a 488 nm MBS excitation filter and a 505 nm long pass (LP) emission filter.

Correlative fluorescence and atmospheric scanning electron microscopy (ASEM) was achieved using the JEOL JSM 6200 ClairScope™. Fluorescence images were acquired with a 40x water dipping LUMPLFLN 40x, (0.8NA) water lens using an Argon ion laser at 488 nm with a 488 nm MBS excitation filter and a 505 nm long pass (LP) emission filter for GFP fluorescence and using an Argon ion laser at 350 nm with a -401 nm MBS excitation filter and a 405 nm long pass (LP) emission filter for DAPI fluorescence. Exposure times were adjusted for each image, typically 5 s for GFP and 1 s for DAPI. ASEM images were acquired using an inverted SEM with accelerating voltage and spot size conditions optimised as discussed in Chapter 3.

A representative image gained by this technique refers to one image (250 µm x 250 µm) collected on multiple cells in a single sample; gained at either 350x magnification or 20,000x magnification at an AC (kV) of 30 kV and at spot size (SS) 35. Small areas were used to gain best focus and then full scan acquired at 20,000x magnification, 80 s scan speed. To collect negative control data and test for specificity of immunogold labelling, focus was achieved using the edge of the film window as a target and 10 focal planes in each direction on fine focus were imaged by changing the focus through one turn of the focus wheel for each focal plane. It should be noted that the JEOL focus wheel cannot be calibrated, and hence the click count was used as a standard focal change at each point. This technique was also implemented, using the immunogold particles as a central focal point when obtaining z-stacks by ASEM.

ASEM images of immunogold were analysed by a version of SPFI (Cherry et al, 1996). In this method, a small area of pixels around a central bright object are fitted with a 2 dimensional Gaussian with the following adjustable parameters: background ($B_0$), x, y-position ($x_0$, $y_0$), intensity (B) and Gaussian width (w):

$$z = B_0 + B \exp \{-[(x-x_0)^2 + (y-y_0)^2]/ 2w^2\}$$

Here, z is the pixel at position x, y. The computer algorithm optimises the values of the parameters, and also determines the standard error of these parameters in the fit.

Signal to noise ratios were calculated from these fitted intensities and the standard deviation of the background signal. In cases where the background was uneven, the background parameter was replaced by a sloping formula (to account for an uneven background intensities during analysis), using Θ as the gradient and Φ as the direction of the slope:

$$z = B_0 \{1 + \tan\Theta\ [\cos\Phi\ (x-x_0) + \sin\Phi\ (y-y_0)\} + B \exp \{-[(x-x_0)^2 + (y-y_0)^2]/ 2w^2\}$$

### 2.4.2 FEGSEM (ESEM)

Atmospheric scanning electron microscopy of B104 cells in Quantomix capsules was performed using a JEOL JSM 7600-F FEGSEM. Magnification and focus were optimised for each sample using working distances of 7.9mm and 18mm with a voltage of 30kV and backscatter and lower angle backscattered electron (LABE) detectors. Cell samples for imaging in Quantomix capsules were cultured, transfected and prepared for imaging identically to as described in Section 2.3.3.

### 2.4.3 Fluorescence recovery after photobleaching (FRAP)

FRAP was performed using a Zeiss 710 invert microscope using the 63x plan apochromat (NA 1.4) objective. Images were typically collected with scan speed 9, line averaging 4, 12 bit, bi- directional scanning. 20 scans were collected pre- bleach using an Argon ion laser at 458 nm with a 459 nm MBS excitation filter and 465- 575 nm bandpass emission filter. Bleaching was achieved with a laser diode at 405 nm at 50 % power with a -405 nm MBS excitation filter. 25 bleaching iterations were conducted in a region of interest that was typically 17 x 17 pixels$^2$. This was followed by ~200 post bleach images using an Argon ion laser at 458 nm with a 458 nm MBS excitation filter and 465- 575 nm bandpass emission filter, in all conditions zero time intervals were used to obtain maximum image collection speed.

FRAP images were analysed by ImageJ (version 1.47) by evaluating the intensity of the puncta in each timeframe, adjusting the position as the object moved from frame to frame. The mean intensity post-bleach ($F_t$) was fitted with an exponential recovery curve to determine the recovery time constant (T):

$$F_t = F_0\{1- \exp(-t/T)\}$$

where $F_0$ is the depth of bleach and T is the time constant. $t_{1/2}$ is calculated from:

$$t_{1/2} = T\log_e 2$$

### 2.4.4 Fluorescence loss in photobleaching (FLIP)

FLIP was performed using a Zeiss 710 invert microscope using the 63x plan Apochromat NA (1.4) lens. Pre- bleach imaging was performed using an Argon ion laser at 458 nm with a 458 nm MBS excitation filter and 465- 575 nm bandpass emission filter, typically acquired with scan speed 9, line averaging 4, 12 bit, bi-directional scanning. Bleaching was achieved in a region of interest that was away from the RIα-CFP puncta after an initial 5 scans using a laser diode at 405 nm at 50 % power with a 405 nm MBS excitation filter with 100 iterations. Repeat bleaching was performed after every 3 scans. Post bleach imaging was performed using the same settings as pre-bleach imaging, allowing for a 30 second interval between each image.

FLIP images were analysed by ImageJ to trace RIα-CFP fluorescence puncta; the intensity decrease of the puncta was measured from frame to frame in the time series. Regions of interest in the cytoplasm and the puncta were monitored parallel to the punta measurements; the cytoplasmic regions of interest identified were not adjacent to the puncta, and were the same in diameter as the region of interest required for the puncta in each individual data set.

### 2.4.5 TEM

Samples were fixed in 4 % PFA (w/v) 4 % sucrose (w/v) for 20 min and washed 3 times in 1 % (w/v) BSA in PBS. Samples were labelled with primary mouse, anti-GFP antibody and anti-mouse 20 nm immunogold secondary antibody. Secondary fixation was by 1 % $OsO_4$ (w/v) (dissolved in UP $H_20$) for 1 h on ice. Fixed samples were washed twice in PBS and dehydrated in an ethanol series of 25 %, 50 %, 75 %, 90 % ethanol, 15 min each. Three 15 min washes in 100 % ethanol were followed by two changes in epoxy propane for 5 min each. Infiltration of resin was conducted by incubation in 50 % epoxy-propane/ 50 % epon araldite for at least 30 min. Polymerisation of resin was achieved in fresh 100 % Epoxy resin at 60 °C overnight. Following thin sectioning using a ultramicrotome (Leica EM UC7), 70 nm sections were collected and stained with 1 % Uranyl Acetate (w/v) (dissolved in UP $H_20$) for 10 min, followed by thorough washing in UP $H_20$ and air drying at room temperature (18 °C) under glass. Sections were imaged using a Technai G2 transmission electron microscope with Mega View III Soft Imaging System.

### 2.4.6 Neuronal imaging.

Rat cerebellar neurons were prepared for fluorescence imaging by Dr GJO Evans and transfected with CFP. Imaging was carried out using a Zeiss 710 inverted confocal microscope. Images were acquired by compiling 5x5 tiled images with bi-directional imaging, using 63x Plan Apochromat (NA 1.4) objective, an Argon ion laser at 458 nm with a 458 nm MBS excitation filter and a 482 -569 nm emission bandpass filter.

Images were analysed using the ImageJ plugin NeuronJ to measure the number and length of neurites of 30 neurons in each sample set. Statistical analysis was performed by one way ANOVA tests using SigmaPlot.

### 2.4.7 RIα-CFP puncta imaging and quantification

B104 neuroblastoma cells were cultured in complete DMEM at 37 °C in a humidified atmosphere containing 5.2 % $CO_2$. Cells were transfected with RIα-CFP, RIα-FLAG or IP-I-CFP on the second day of culture and differentiated for 4 days by incubation with 1 mM dib-cAMP. Samples were fixed in 4 % PFA (w/v) 4 % sucrose (w/v) for 20 min at room temperature (18 °C). Cells were washed 3 times by addition and immediate, complete aspiration of 200 µl PBS and blocked 3 times with 1 % (w/v) BSA in PBS by addition and immediate, complete aspiration of 200 µl 1 % (w/v) BSA in PBS. Labelling was performed with primary and secondary antibodies as described in Chapter 5 and Table 2.1 and 2.2. Images were acquired using a Zeiss 710 inverted confocal microscope to compile 5x5 tiled images with bi-directional imaging, using 20x Plan Apochromat (NA 0.8) lens, an Argon ion laser at 458 nm with a 458/594 MBS nm excitation filter, and a 482- 569 nm emission bandpass filter for CFP and 612- 740 nm for Alexa 594 imaging. Colocalisation studies were carried out by manual observation of puncta using typically 10 images per condition.

### 2.4.8 Volocity

Microscopic colocalisation was done using the computational analysis program Volocity. Using this program in 'colocalisation' mode the cellular area (either, the whole cell for antibody internalisation in Chapter 4, or puncta analysis in Chapter 5) to be measured was selected. The thresholds of each fluorescence emission channel were then adjusted for each sample. Threshold statistics were then obtained for the measured area including the Pearson's Correlation number. This number is a measure of the relationship between two sets of data, with a value range between -1 and 1, with anti-correlation indicated by negative values, and colocalisation shown by positive values up to the perfect colocalisation value of 1.

# 3.0 Development of methods for high resolution protein localisation by atmospheric scanning electron microscopy.

## 3.1 Introduction.

The development of super resolution microscopy (SRM) techniques have significantly improved the spatial resolution of optical imaging to ~20 nm in non-biological systems as discussed in Chapter 1. Techniques such as stochastic optical reconstruction microscopy (STORM) and photo-activated light microscopy (PALM) have revealed the 3D organisation of the actin cytoskeleton in cellular sheet-like protrusions (Xu et al. 2012) enabling greater accuracy in protein localisation (Betzig et al. 2006). In comparison, Bayesian localisation microscopy, employs computational algorithms to resolve cellular structures; this can offer an achievable resolution of ~50 nm, using wide field fluorescence microscopy (Cox et al. 2012). Techniques such as stimulated emission depletion microscopy (STED) (Hell & Wichmann 1994) and structured illumination microscopy (SIM) (Gustafsson 2000) have greatly improved the precision of optical microscopy, reviewed by Eggeling et al. (2013). Although SRM techniques have vastly improved the achievable resolution of optical microscopy, there still remains a gap between resolution gained by optical microscopy of live biological samples and the fine detail provided by electron microscopy of separate, processed biological samples.

Advances in imaging technology have led to the development of various methods employing light and electron microscopy in conjunction (Plitzko et al. 2009; Robinson and Takizawa 2009; Rijnsoever, et al 2008) with the aim to improve resolution to ~2 nm and broaden the information gained by both fluorescence and EM techniques. This approach has seen the development of sophisticated techniques of high-throughput loading and freezing (Verkade 2008) in order to achieve direct correlation of fluorescent samples with a frozen, yet ‘hydrated state’ sample in electron microscopy.

EM itself often involves laborious sample processing including dehydration, resin embedding and ultra-thin sectioning which may be detrimental to biological samples and can result in various artefacts. Firstly, fixation, depending on the technique used, may result in the loss or redistribution of soluble proteins (Schnell et al. 2012; Melan and Sluder 1992). Secondly, the process of dehydration of the sample results in shrinkage and loss of the original, live cell state, so protein localisation cannot be directly compared to that determined by live cell fluorescence studies. Thirdly, immunofluorescence of live cells cannot be directly and truly correlated with study of the ultrastructure gained by either standard EM or cryo-EM. To better preserve ultrastructural detail, cryo-EM and high pressure freezing are often used. This results in the production of an entirely separate sample from those imaged by live cell fluorescence, which may no longer represent a hydrated cell state. As ultra-thin sections are imaged by TEM only a snapshot of a single focal plane within a sample is obtained.

In this study immunofluorescence labelling methods were adapted to develop a directly correlative method for light and electron microscopy for application in the study of structure and function in differentiated neuroblastoma cells. This was achieved by imaging samples by atmospheric scanning electron microscopy (ASEM) using the novel imaging technology the JEOL ClairScope™; Figure 1.10.1. This technology enables the development of a technique, analogous to laser scanning confocal microscopy, whereby the electron beam is replaces the laser beam in fluorescence microscopy. This then allows the acquisition of SRM images of hydrated state biological samples simply labelled with antibodies, which can be correlated directly with fluorescence of previously imaged live cells. This is without the need for further processing and at much faster acquisition rates, with the aim to develop a novel SRM technique that utilises the e-beam, whilst also permitting a degree of ultrastructural detail not possible with most other SRM techniques if followed by additional staining with heavy metal stains in order to create contrast in biological samples.

## 3.2 Aims and objectives of research described in Chapter 3.

Aim:

Development of a specific immunogold labelling protocol to prove eSRM imaging using the ASEM.

Objectives

1) Specific immunogold labelling of ultrastructural detail using actin filaments in U251 glioblastoma cells.

2) Specific immunogold labelling of whole cell vesicle population in differentiated neuroblastoma cells.

3) Achieve high resolution imaging and identification of individual vesicles labelled with 20 nm immunogold through the 3 dimensional hydrated cell structure.

## 3.3 Results

### 3.3.1. Development of eSRM imaging and Immunogold Labelling Protocol.

Successful bioimaging by ASEM using the ClairScope™ requires the imaging conditions to be adapted for each sample to achieve optimal image quality and resolution. The energy potential of the electron beam (acceleration voltage; AV) is instrument limited and may be set at one of three levels 10AV, 20 AV, 30AV. The resolution achieved may also be optimised by altering the electron beam spot size (SS). Initial tests to determine the optimum AV and SS for the detection of immunogold were carried out using 20 nm immunogold particles adhered to a ClairScope™ dish window by a poly-L-lysine layer. The particles were imaged by ASEM at increasing SS and AVs, as shown in Table 3.1. Values for the width, intensity and signal to noise were obtained by SPFI analysis of the images, and averaged for typically 100 particles for each image.

| AV | Spot Size | Mean Width (nm) | Mean Intensity (Counts) | Mean Signal to Noise Ratio |
|---|---|---|---|---|
| 30 | 25 | 28 ± 10 | 144 ± 43 | 2.88 ± 0.86 |
|  | 30 | 23 ± 7 | 270 ± 120 | 4.15 ± 1.85 |
|  | 35 | 23 ± 5 | 440 ± 170 | 4.68 ± 1.81 |
|  | 40 | 32 ± 7 | 640 ± 170 | 4.48 ± 1.19 |
|  | 45 | 40 ± 10 | 630 ± 240 | 4.06 ± 1.55 |
| 20 | 35 | 24 ± 5 | 290 ± 70 | 5.00 ± 1.21 |
|  | 40 | 28 ± 6 | 350 ± 70 | 4.93 ± 0.99 |
|  | 45 | 36 ± 7 | 290 ± 90 | 5.47 ± 1.70 |

**Table 3.1 Imaging of 20 nm immunogold at increasing accelerating voltage and spot size.** Mean width, mean intensities and mean signal-to-noise values with calculated standard error of the mean (s.e.m) of particles imaged at increasing SS and AV at 20,000x magnification (n = 3). Images could not be obtained at 10AV, and at smaller spot sizes at 20AV.

The optimal imaging conditions with regards to signal to noise for imaging gold particles, where no pixel saturation occurred, was found to be 20AV at SS35. These conditions also gave good resolution with a mean width of 24 ± 5 nm. 30AV, with a SS35 achieved best resolution with a mean width of 23 ± 5 nm, but slightly decreased signal to noise. These settings were used for each ASEM image acquisition onwards in these studies. A similar resolution was also observed at 30AV with SS30, although the intensity above background is much improved at SS35.

### Optimising GFP labelling of synaptopHluorin transfected B104 neuroblastoma cells with 1.4 nm nanogold particles.

Due to the small size of the vesicles, reported as ~50 nm (Darcy et al. 2006b), it was desirable to use as small a probe as possible. Initial attempts focussed on 1.4nm diameter nanogold. Vesicles labelled with this probe would be observed clustered together in the presynaptic terminal and would therefore produce a significant and detectable signal. B104 neuroblastoma cells were successfully transfected with synaptopHluorin as shown in Figure 3.3.1.1. However, only a small minority of cells were transfected. Initial imaging concentrated on direct imaging of 1.4 nm immunogold labelled cells. These cells provided too little contrast for ClairScope™ imaging. Therefore gold enhancement was required to increase the particle diameter for sufficient signal generation, thus improving detection. This treatment increases the diameter of gold particles through the deposition of gold ions in solution to form an outer layer on the original gold particles.

B104 neuroblastoma cells transfected with synaptopHluorin were fixed (4 % (w/v) PFA/ 4 % (w/v) sucrose) and permeabilised (1 % (v/v) Triton X-100) and then labelled with mouse anti-GFP Fab fragments, followed by anti-mouse IgG coupled to 1.4 nm immunogold particles (NanoProbes Ltd). Samples were visualised using the ClairScope™ to identify the optimum experimental conditions required. Unlabelled control cells, B104 neuroblastoma cells fixed (Figure 3.3.1.1a) and B104 neuroblastoma cells fixed and treated with gold enhance only for 5 min (Figure 3.3.1.1b) were tested alongside labelled B104 neuroblastoma cells fixed and permeabilised with 1 % (v/v) Triton for 20 min at room temperature (18 °C) (Figure 3.3.1.1c) or ice cold methanol for 10 min (Figure 3.3.1.1d).

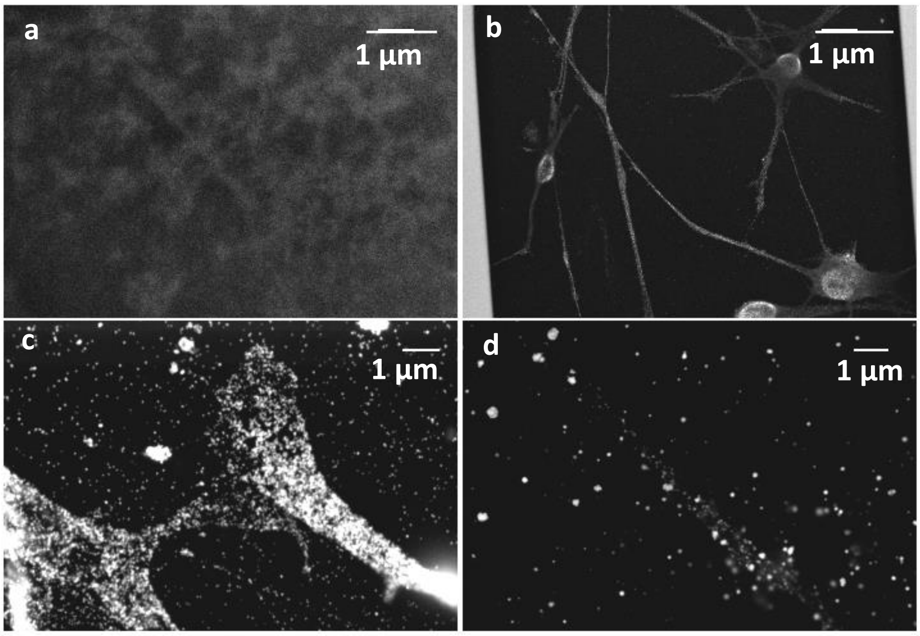

**Figure 3.3.1.1. Visualisation of 1.4nm with gold enhance. Representative images** a) B104 neuroblastoma cells fixed in 4 % (w/v) PFA/ 4 % (w/v) sucrose only. b) B104 cells fixed in 4 % (w/v) PFA/ 4 % (w/v) sucrose incubated with gold enhance. c) B104 cells fixed in 4 % (w/v) PFA/ 4 % (w/v) sucrose, permeabilised with 1 % (v/v) Triton and incubated with 1.4nm nanogold followed by gold enhance. d) B104 neuroblastoma cells fixed and permeabilsed with methanol and incubated with 1.4nm nanogold followed by gold enhance. n = 3 biological replicates for each condition.

It was observed that gold enhancement created significant non-specific labelling throughout samples (Figure 3.3.1.1b-d) even with no immunogold present. Specific labelling would be expected to be localised to the vesicles alone, with distinct punctate patterning within the cell body. In contrast, labelling was observed across the whole of the cells with equal contrast. Individual vesicles could not be identified due to the non-specific nature of gold enhance. Technical assistance at Nanoprobes suggested a number of variations to the standard method, such as washing with EDTA to remove any non-specific metal ions, although no improvements were obtained. Therefore, in order to overcome this problem and permit simple direct labelling of proteins of interest and targeted specifically to synaptic vesicles, larger, 20nm gold particles, covalently linked to IgG anti mouse specific antibodies were used.

### 3.3.2. Specific labelling of βIII tubulin in B104 neuroblastoma cells with 20nm immunogold particles.

The working concentration of 20nm immunogold for use on hydrated cells was determined by analysis of cells on the ClairScope™. Due to the low transfection rate of B104 neuroblastoma cells with synaptopHluorin (spH) (~3 %) and the limited working area on the ClairScope™ dish windows (250µm x 250µm square) this method was deemed too low throughput to determine specific binding and optimisation of the antibody concentration was needed. Therefore non-transfected B104 neuroblastoma cells cultured on ClairScope™ dishes were labelled with mouse primary antibody targeted against βIII tubulin (a protein specifically expressed in neuronal cells followed by anti-mouse secondary 20nm immunogold conjugate. Imaging of immunogold labelled cells was conducted using the ClairScope™. Initial imaging displayed very little contrast on the cells themselves (Figure 3.3.2.1a). The addition of Uranyl acetate (UA) increased the contrast and allowed focussing on the cells themselves (Figure 3.3.2.1b); treatment with 0.001 % (w/v) UA for 30 seconds improved contrast and enabled image focussing and acquisition.

Cells were clearly visible due to contrast created by the UA staining, which enabled focussing on cell membranes (Figure 3.3.2.2). Once focussed, electron dense puncta were observed that corresponded to the expected labelling area of immunogold labelling of βIII tubulin throughout the cell membrane. The samples were imaged at increasing magnifications in order to detect electron dense areas which would indicate the presence of gold particles. Electron dense puncta could be seen on the focussed sample (red highlighted area in Figure 3.3.2.1a and b, shown in Figure 3.3.2.2a, with electron dense peaks indicated by red arrows) when imaged at 30,000x magnification. Importantly, this process was reproducible on multiple samples, with the similar electron dense puncta visible over the UA background (illustrated in Figures 3.3.2.2b and 3.3.2.2c, with electron dense peaks indicated by green and yellow arrows respectively).

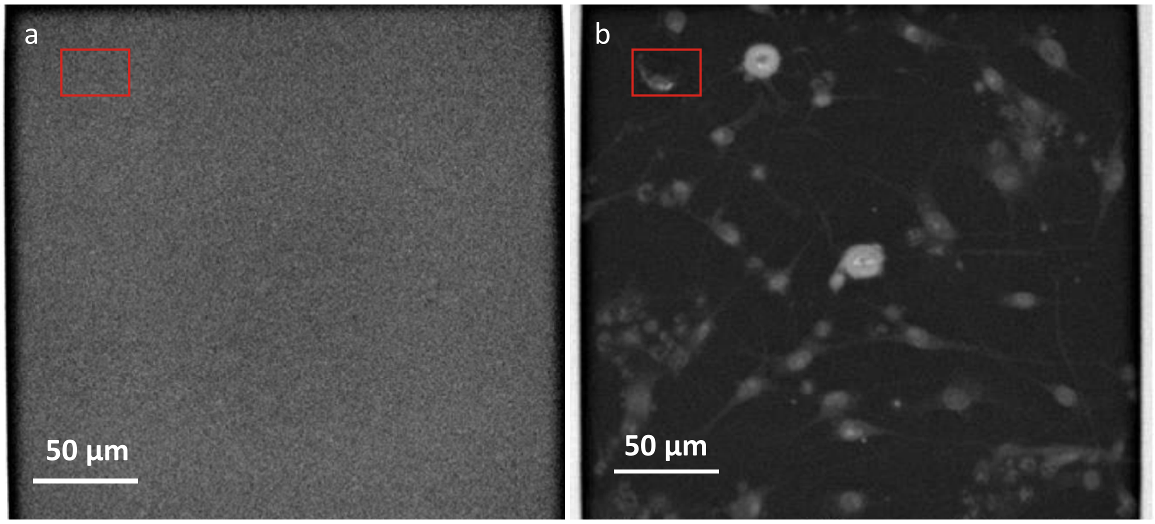

**Figures 3.3.2.1. ASEM of Unstained Cells and UA Stained Cells.** Representative images (a) ASEM of ClairScope™ dish silicon nitride film window with unstained cells. (b) ASEM of the same ClairScope™ dish silicon nitride film window with cells stained with UA. Red box highlights intended area of further analysis.

Electron dense peaks were observed at 30,000x magnification (Figure 3.3.2.2) indicated by arrows. To positively identify potential gold particles from background intensities, analysis was performed using an algorithm often used in super resolution microscopy (SRM) techniques which measures and fits the mean diameter of a defined peak intensity associated with the object imaged using a 2D-Gaussian curve (Morrison et al. 1994). Data analysis performed on these areas of interest measured the width of each bright peak and also the intensity of each area above local background intensity. The calculated mean width, mean intensity above background, background intensities and signal to noise for each data set was determined and displayed in Table 3.2 and Figure 3.3.2.2.

| **Image 3.3.2.2** | **Mean Width (nm)** | **Mean Intensity Above Background (Counts)** | **Mean Background Intensity (Counts)** | **Signal to Noise Ratio** |
|---|---|---|---|---|
| **a** | 29 ± 9 | 123 ± 34 | 470 ± 60 | 2.1:1 |
| **b** | 35 ± 10 | 97 ± 21 | 840 ± 80 | 1.2:1 |
| **c** | 32 ± 4 | 180 ± 49 | 840 ± 110 | 1.6:1 |

**Table 3.2. Parameters for images of 20 nm immunogold labelling neuroblastoma cells.** Mean width, mean intensities and mean signal to noise with calculated standard error of the mean (s.e.m) for the images shown in Figure 3.3.2.2. Letters refer to the three Figure panels.

Control areas in cells labelled with the secondary gold label only were imaged, which confirmed specific immunogold labelling of the anti β tubulin primary antibody was successful, although the specificity of the labelling remained undetermined by this method due to high background contrast as a result of UA staining. This background also increases the noise, therefore hypothetically, better signal to noise would be found in the absence of UA staining.

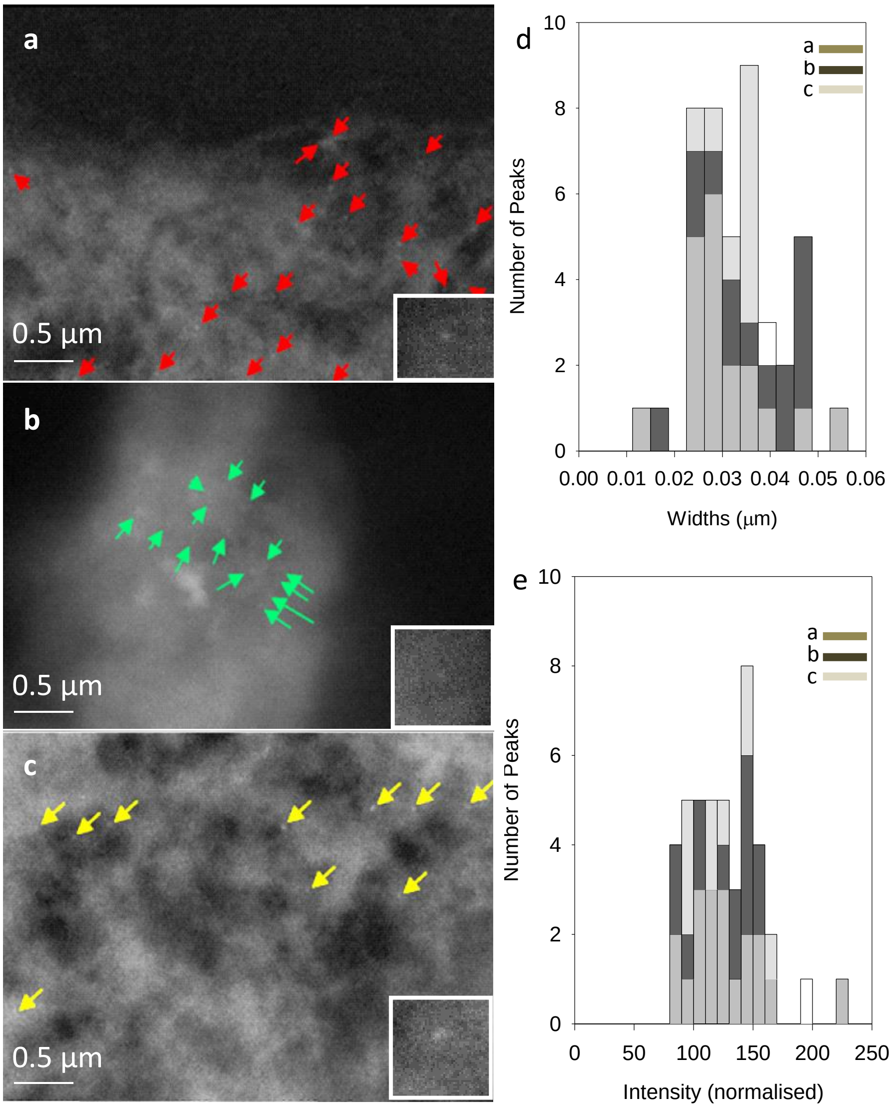

**Figure 3.3.2.2. Electron dense peaks observed in UA stained neuroblastoma cells labelled with mouse anti β tubulin and anti mouse 20 nm immunogold.** ASEM images of B104 neuroblastoma cells stained with UA, shown in a -c. Labelled with mouse, anti β tubulin, primary antibody and anti mouse 20nm immunogold particles. Electron dense areas are labelled by coloured arrows. Scale bar 0.5 µm. d) Stacked histogram displaying widths of each peak measured indicated by coloured arrows in the three images. e) Stacked histogram of intensities above background, normalised to the mean intensity in the first image (as brightness and contrast varies between each image). Number of measurements per sample; a) n= 9 b) n= 13 c) n= 19. a), b) and c) are 3 separate biological replicates.

### 3.3.3 Visualisation of fluorescently labelled actin filaments in U251 glioblastoma cells

The protocol for labelling βIII tubulin with 20 nm immunogold was developed in B104 neuroblastoma cells not expressing fluorescent proteins. The aim was to use this technique for correlative fluorescence and scanning electron microscopy, thus further optimisation of the protocol to enable specific labelling of fluorescent proteins was done using U251 glioblastoma cells stably expressing YFP-Lifeact. This is a 17 amino acid sequence, from the C terminal actin binding domain of Abp 140 (MGVADLIKKFESISKEE), derived from *Saccharomyces cerevisiae* (Izeddin et al. 2011). To ensure that the binding of the expressed LifeAct-YFP actin labels all actin filaments and has no effect such as steric hindrance; this would prevent maximum antibody labelling. Cells were cultured on glass cover slips and stained with rhodamine phalloidin and 4',6-diamidino-2-phenylindole (DAPI) prior to imaging by confocal fluorescence microscopy, shown in Figure 3.3.3.1. Co-localisation of rhodamine phalloidin and YFP was observed and quantified using Volocity software (Methods section 2.4.8), which correlates with previously published research into the binding dynamics of the LifeAct peptide and conjugated fluorophores (Riedl et al. 2008) and (Delgado-Álvarez et al. 2010).

To develop a protocol for labelling fluorescent proteins with 20 nm immunogold particles U251 cells were labelled with primary mouse, anti-GFP antibody and anti mouse, secondary Alexa 594 antibody. This experiment was conducted with the aim of revealing any steric hindrance of anti-GFP binding caused by binding of LifeAct YFP to F-actin sites. Results showed complete antibody saturation and colocalisation of YFP and Alexa 594 fluorescence at a labelling concentration (1:1000 dilution) of stock primary antibody (Figure 3.3.3.1b). These results also confirm that no steric hindrance resulting from LifeAct YFP peptide binding itself, therefore this labelling method was carried forward for use with 20 nm immunogold particles. Confirmation of specific actin binding of primary and secondary antibody to Lifeact YFP expressed in U251 cells was used to develop a protocol for labelling fluorescent proteins with 20 nm immunogold. U251 cells were cultured on ClairScope™ dishes, fixed and permeabilised with 1 % (v/v) Triton and labelled with increasing concentrations of 20 nm immunogold and imaged on the JEOL ClairScope™. Cells were stained with 0.001 % (w/v) UA to increase the contrast of cells for ASEM imaging, which can be seen in Figure 3.3.3.1a. Results of control tests where non-fluorescent areas were imaged are also shown in Figure 3.3.3.1b.

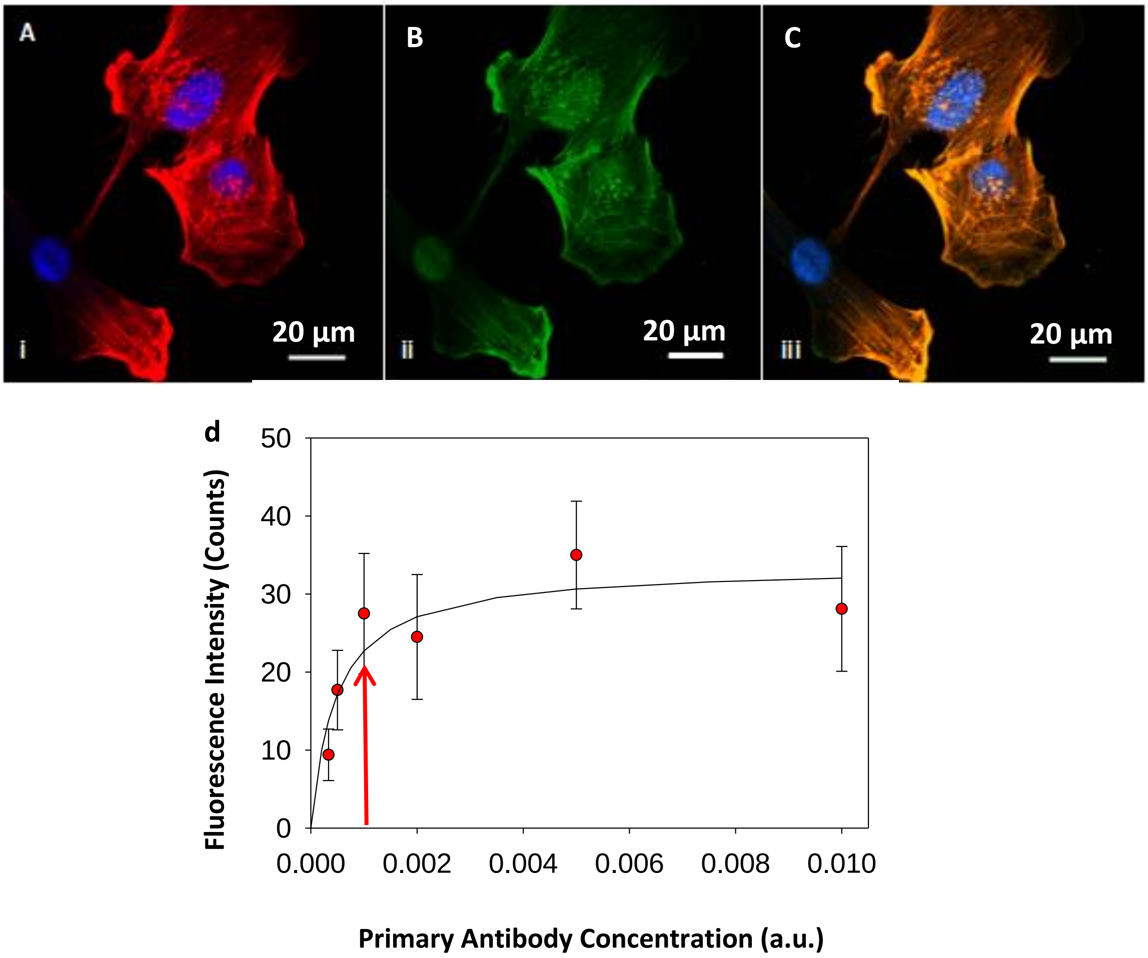

**Figure 3.3.3.1 Colocalisation of rhodamine phalloidin with LifeAct YFP.** Representative images a) U251 cells showing DAPI and rhodamine phalloidin, b) the same cells showing LifeAct YFP. c) Colocalisation of LifeAct YFP actin and rhodamine phalloidin. d) anti-GFP /YFP binding curve. **d) Anti-GFP primary antibody binding titration.** Typical images for 90 measurements made on 3 separate biological replicates. Titration curve of anti GFP binding labelling LifeAct YFP expressed in U251 glioblastoma cells. Optimum binding was observed at a dilution of 1:1000 of stock antibody (indicated by red arrow).

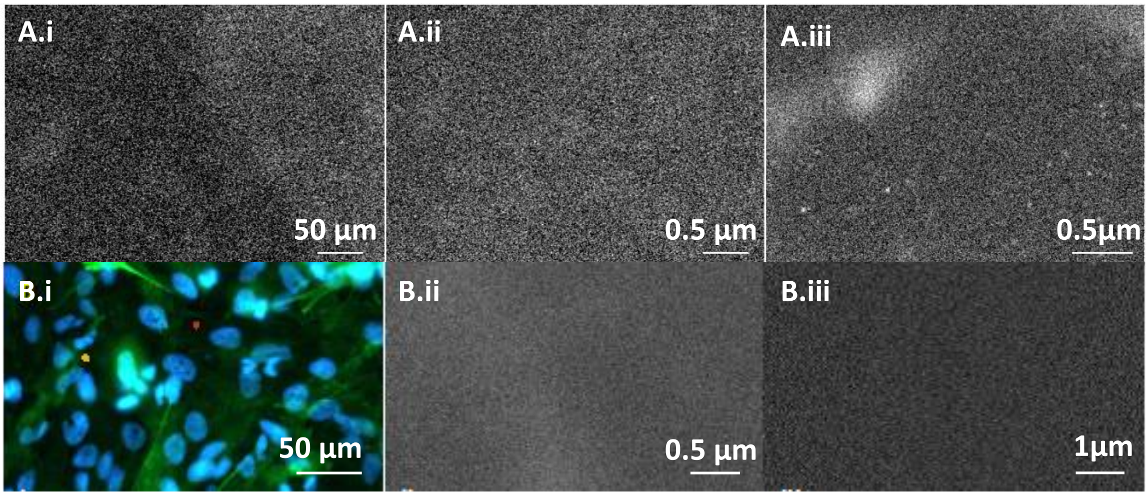

**Figure 3.3.3.2. Titration of 20 nm immunogold. A) i)** ASEM of U251 cells expressing LifeAct YFP actin, labelled with primary mouse anti GFP and anti mouse 20 nm immunogold secondary antibody at a stock dilution of 1:50. **A) ii)** ASEM of U251 cells expressing LifeAct YFP actin, labelled with primary mouse anti GFP and anti mouse 20 nm immunogold secondary antibody at a stock dilution of 1:10. **A) iii)** ASEM of U251 cells expressing LifeAct YFP actin, labelled with primary mouse anti GFP and anti mouse 20 nm immunogold secondary antibody at a stock dilution of 1:5. **B i)** Wide-field fluorescence image of U251 cells expressing Lifeact- YFP actin, stained with DAPI. Red and yellow spots indicate non-fluorescent areas for imaging by ASEM. **B ii** and **B iii)** Areas indicated by red (ii) and yellow spots (iii) in b i) imaged by ASEM using the JEOL ClairScope™ at 30,000x.

### 3.3.4 Evaluation of 20 nm immunogold labelling of LifeAct YFP actin in U251 glioblastoma cells

Replicate LifeAct YFP actin samples were labelled with 20 nm immunogold. Fluorescence images of LifeAct YFP actin were acquired using the ClairScope™ (Figures 3.3.4.1a and 3.3.4.1b). A higher magnification image of the highlighted area in 3.3.4.1a is shown in 3.3.4.1b. Imaging by ASEM of the example areas highlighted in 3.3.4.1b was carried out (Figures 3.3.4.1 c- f). It was observed that the immunogold labelling was present in areas containing fluorescent actin filaments and that the backgrounds were non-uniform due to the UA staining. Positive identification of potential immunogold particles from background variation and possible staining artefacts, was performed using the super resolution algorithm described in Figure 3.3.4.1.

Analysis of electron dense peaks imaged in Figure 3.3.4.1 revealed mean widths and intensities above background for each measured peak displayed as histograms in Figure 3.3.4.2c –j and also in Table 3.3. Mean intensities above background for each data set are also shown in a stacked histogram in Figure 3.3.4.2b.The average widths of between 23 nm and 35 nm and the specific immunogold membrane labelling suggest that the electron dense peaks imaged are individual 20 nm immunogold particles, with some doublets or higher aggregates.

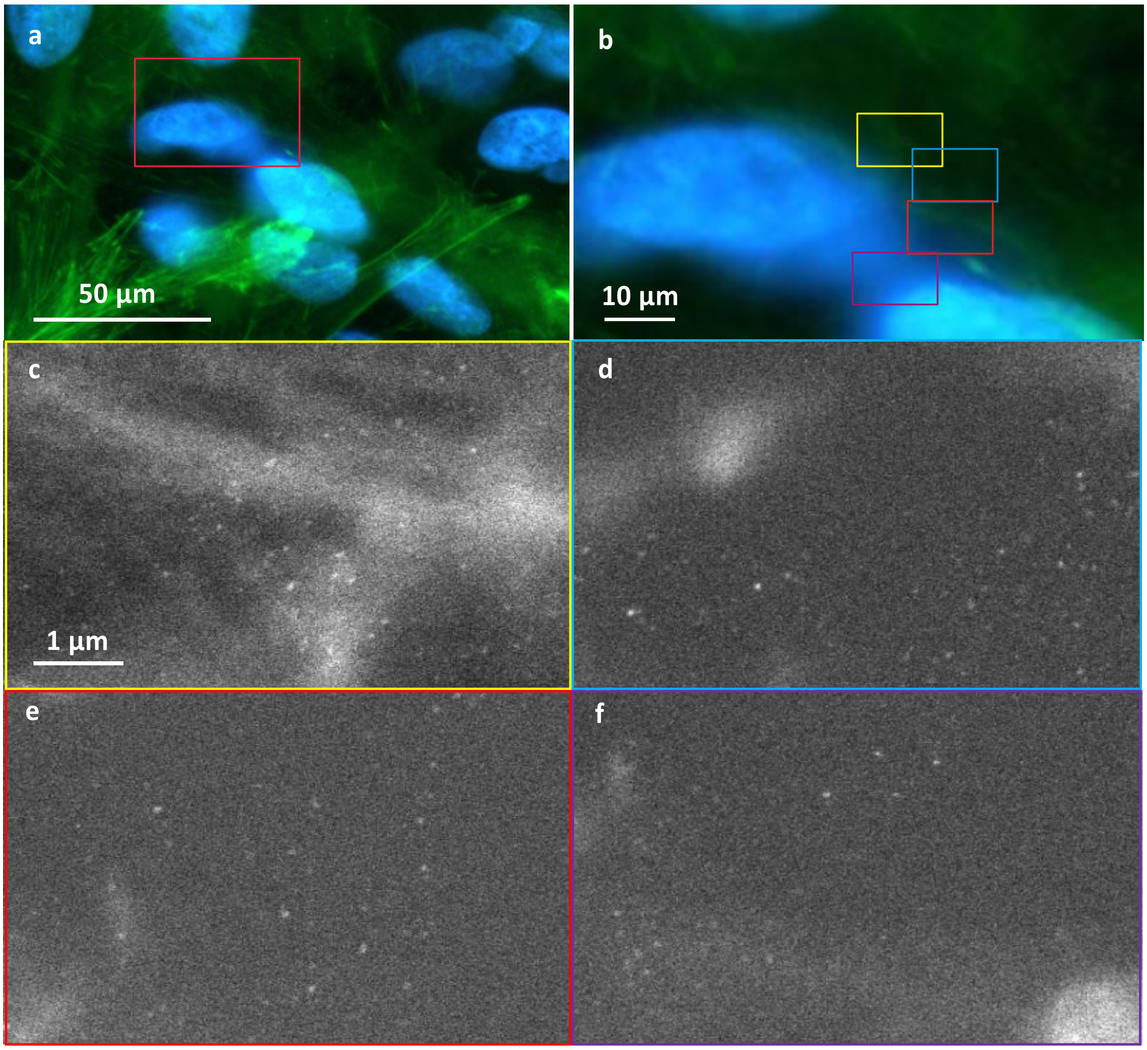

**Figure 3.3.4.1. Correlative fluorescence and ASEM images of immunogold labelled U251 cells.** a) Fluorescence image of U251 cells stably transfected with LifeAct YFP actin and stained with DAPI. b) Red boxed area in a). c-f ASEM images of immunogold labelling of YFP actin at 20000x magnification. c) Yellow highlighted area in b). d) Blue highlighted area in b). e) Red highlighted area in b). f) Purple highlighted area in b). Electron dense areas are visible in ASEM images indicating immunogold labelling of YFP actin. Scale c)-f) 1 µm

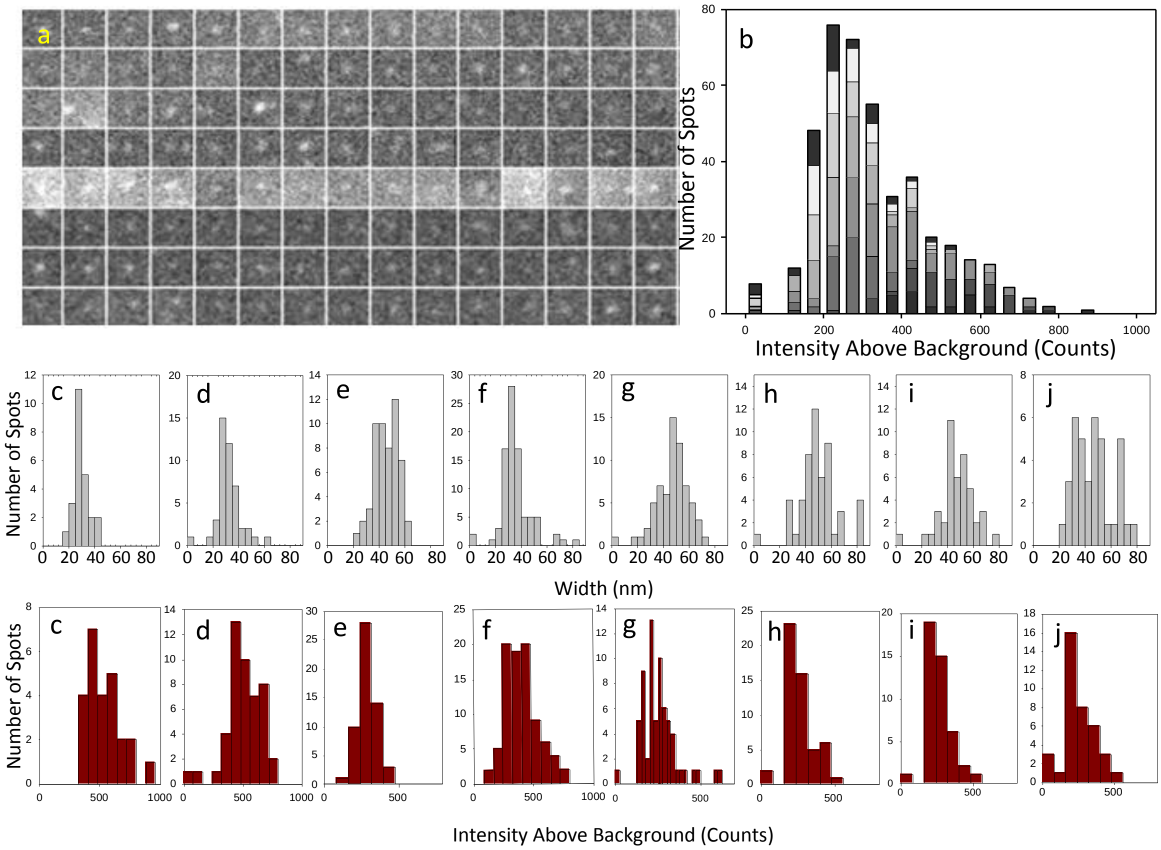

**Figure 3.3.4.2. Analysis of electron dense peaks present in ASEM images of immunogold labelled U251 cells.** a) Montage of electron dense regions imaged in several areas of immunogold labelled U251 cells. b) Stacked histogram of intensities above background of each data set. c)- j) Histograms of widths and intensities of peaks measured in four areas of two different images. Histograms show analysis of 300 (typically 100 per sample) measurements of electron dense peaks made on 3 separate biological replicates.

| Image 3.3.4.2 | Mean Width (nm) | Mean Intensity Above Background (Counts) | Mean Background Intensity (Counts) | Mean Signal to Noise Ratio |
|---|---|---|---|---|
| **c** | 20 ± 4 | 490 ± 130 | 550 ± 60 | 6.5:1 |
| **d** | 25 ± 8 | 360 ± 130 | 580 ± 30 | 4.8:1 |
| **e** | 33 ± 10 | 250 ± 60 | 750 ± 100 | 3.3:1 |
| **f** | 23 ± 6 | 490 ± 130 | 580 ± 50 | 6.5:1 |
| **g** | 35 ± 9 | 250 ± 100 | 630 ± 20 | 3.3:1 |
| **h** | 35 ± 10 | 230 ± 80 | 660 ± 30 | 3.1:1 |
| **i** | 34 ± 9 | 230 ± 80 | 690 ± 40 | 3.1:1 |
| **j** | 34 ± 10 | 230 ± 90 | 700 ± 30 | 3.1:1 |

**Table 3.3. Parameters for images of 20 nm immunogold labelling glioblastoma cells** Mean widths, mean intensities with calculated standard error of the mean (s.e.m) and mean signal to noise for images shown in Figure 3.3.4.2. Letters refer to the panels in Figure 3.3.4.2.

### 3.3.5 GFP specific 15 nm immunogold labelling in GFP actin transfected B104 neuroblastoma cells

The protocol developed for the specific labelling of YFP actin with 20 nm immunogold particles was developed with the aim to produce SRM images which revealed the localisation and organisation of cellular ultrastructure at nanometer resolution in hydrated samples of cells of neurological significance. Differentiated B104 neuroblastoma cells were transfected with GFP actin, in the ClairScope™ dish, and imaged on a Zeiss 510 upright confocal microscope to identify potential areas for high resolution imaging in the ClairScope™. The cells were then fixed and permeabilised, and labelled with anti-GFP primary antibody, as described in Methods section 2.3.3. A secondary gold antibody was then applied; in an attempt to improve resolution, 15 nm immunogold was used in the absence of UA. Assumed immunogold puncta were clearly seen on non-UA stained samples (Figure 3.3.5.1).

It was observed that 15 nm immunogold specifically labelled the expressed GFP actin, although resolution was not improved beyond 20 nm; 3.3.5.1e. The calculated mean width for each electron dense peak was 34 ± 15 nm. The calculated mean intensity was 228 ± 7 counts with a background value of 230 ± 80 counts, with a signal to noise ratio of 2.85:1. Negative controls were conducted on areas of no fluorescence; ten focal planes at 20,000x magnification were imaged using identical settings after finding the best focus at the edge of the film window. Immunogold was not observed in control areas (non YFP expressing cells within the same experimental samples), suggesting GFP-actin specific labelling.

The increased contrast given by the more densely immunogold labelled sample enabled the images to be focussed without the need of UA.

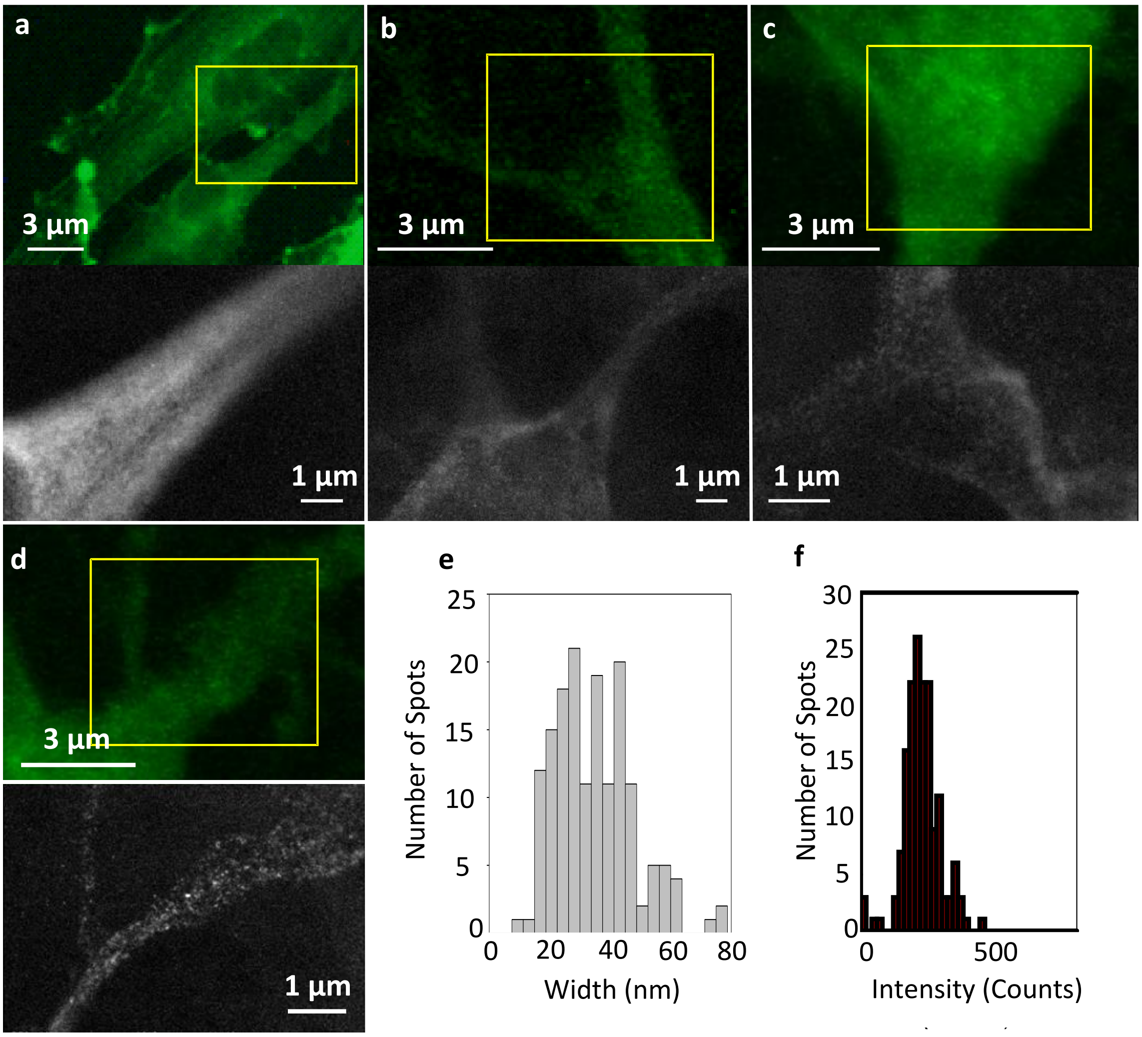

**Figure 3.3.5.1 Specific Immunogold labelling of B104 neuroblastoma cells transfected with GFP actin.** a) –d) Fluorescence images of B104 neuroblastoma cells transfected with GFP actin. Actin filaments appear as green fluorescent areas. Fluorescence images were acquired with a 40x water dipping lens using a Zeiss 510 upright confocal microscope. Directly correlated images of actin specific immunogold labelling are shown below each fluorescence image, acquired by ASEM on the ClairScope™. e) Measured widths of peaks imaged in ASEM image d. f) Measured intensities for each measured peak in ASEM image d) minus the background intensity. n = 100 measurements made on one biological replicate.

### 3.3.6 Immunogold labelling of a population of vesicles in B104 neuroblastoma cells transfected with synaptopHluorin

To visualise vesicle localisation within neuroblastoma cells, with a resolution of ~30 nm, B104 neuroblastoma cells were cultured on ClairScope™ dishes, transfected with synaptopHluorin and differentiated for 4 days in complete DMEM with 1mM cAMP. Samples were fixed and permeabilised to allow labelling of spH with primary mouse anti-GFP antibody followed by anti-mouse 20 nm immunogold, as previously described. No UA staining was used prior to imaging by ASEM as the direct staining provided sufficient contrast. 15 nm immunogold was not used in these experiments as, although labelling intensity was improved, as shown in Figure 3.3.5.1, the particles in the images were poorly defined, and it was not possible to carry out full analysis on the majority of the electron dense peaks imaged.

Images of labelled cells are shown in Figure 3.3.6.1 over multiple replicates. Electron dense peaks were observed by ASEM and analysed as previously described except that very densely labelled areas had to be avoided. To confirm the specificity of immunogold labelling for spH, non-transfected cells were imaged through 10 focal planes; these results showed no immunogold. These results suggest that specific labelling of synaptic vesicles with immunogold in cells transfected with spH is achievable. 20 nm immunogold was imaged successfully at a magnification of 20,000x; histograms of mean widths, intensities above background values (Figure 3.3.6.1). Values of mean widths and intensities and signal to noise are displayed in Table 3.4.

| **Image 3.3.6.1** | **Mean Width (nm)** | **Mean Intensity Above Background (Counts)** | **Mean Background Intensity (Counts)** | **Mean Signal to Noise Ratio** |
|---|---|---|---|---|
| **a** | 25 ± 9 | 410 ± 180 | 240 ± 30 | 13.7:1 |
| **b** | 24 ± 10 | 730 ± 250 | 650 ± 100 | 7.3:1 |
| **c** | 20 ± 4 | 250 ± 110 | 260 ± 30 | 8.3:1 |

**Table 3.4. Parameters for images of 20 nm immunogold labelling neuroblastoma cells** Mean width, mean intensities with calculated standard error of the mean (s.e.m) and mean signal to noise for the images shown in Figure 3.3.6.1. Letters refer to the Figure panels. n = 100 measurements made on 3 biological replicates.

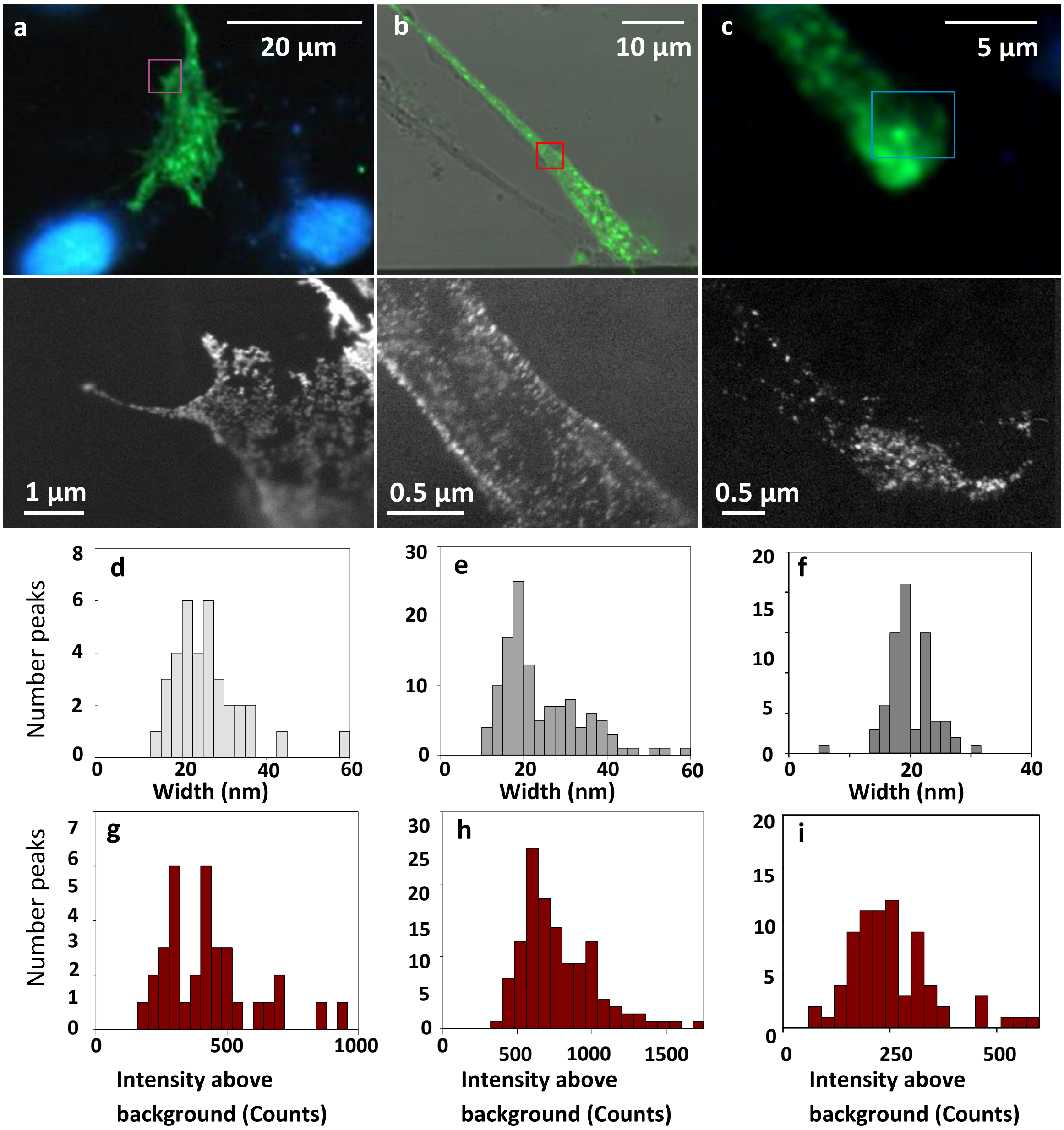

**Figure 3.3.6.1. Immunogold labelling of B104 neuroblastoma cells transfected with SynaptopHluorin (spH).** a)- c) Fluorescence images of spH transfected B104 neuroblastoma cells and the directly correlating images acquired by ASEM imaged on the ClairScope™. d-f) Measured widths of electron dense peaks in each data set. g-i) Measured intensities above background for each data set. n = 100 measurements made on 3 biological replicates.

### 3.3.7 Spatial distribution of immunogold labelling showing localisation of vesicles within the cell body

To investigate the organisation of vesicles, analysis was carried out to assess the localisation of immunogold labelling throughout the fixed hydrated, 3D cell structure in B104 neuroblastoma cells. A non-calibrated z-stack was acquired by ASEM; focus was changed until all visible electron dense peaks had lost focus, and a series of images were then acquired at focal planes, through best focus to the focal plane where all visible peaks were once again out of focus. This allows a projection of the serial images to be compiled to determine the localisation of immunogold labelled vesicles and furthermore identify the 3 dimensional organisation of labelled vesicles.

B104 neuroblastoma cells were cultured on ClairScope™ dishes, as previously described, transfected with spH, stained with DAPI (Figure 3.3.7.1a) and labelled with primary anti GFP antibody and secondary 20 nm immunogold particles. Using the SPFI algorithm previously described, the peaks measured were linked between each focal plane image; changes in width and intensity, and also any drift caused by repeated exposure to the electron beam were tracked, for individual particles, which enabled a maximum intensity projection to be produced; Figure 3.3.7.1b. Widths and intensities of the electron dense peaks in each image of the stack were measured as previously described. The measured intensities shown in 3.3.7.1d show a trend inverse to that seen in 3.3.7.1c, suggesting that as focus is achieved intensity above background intensity increases whilst the width decreases. The intensity graphs were fitted by a Gaussian peak. The z-position of each particle was taken as the value of the intensity maximum along the frame number axis, and the errors as the width of this Gaussian shape. The distribution of the immunogold labelling throughout the cell is described in Figures 3.3.7.1e and f, showing a small range of focal planes throughout the sample where specific labelling has occurred in the presence of spH labelled vesicles. It was observed that the immunogold particles were at best focus between focal planes 12-14; shown by dashed lines in Figure 3.3.7.1c. At this focal plane the calculated mean width was 24 ± 8 nm with a calculated mean intensity of 460 ± 180 counts with a background intensity of 690 ± 174 counts, signal to noise ratio 2.9:1.

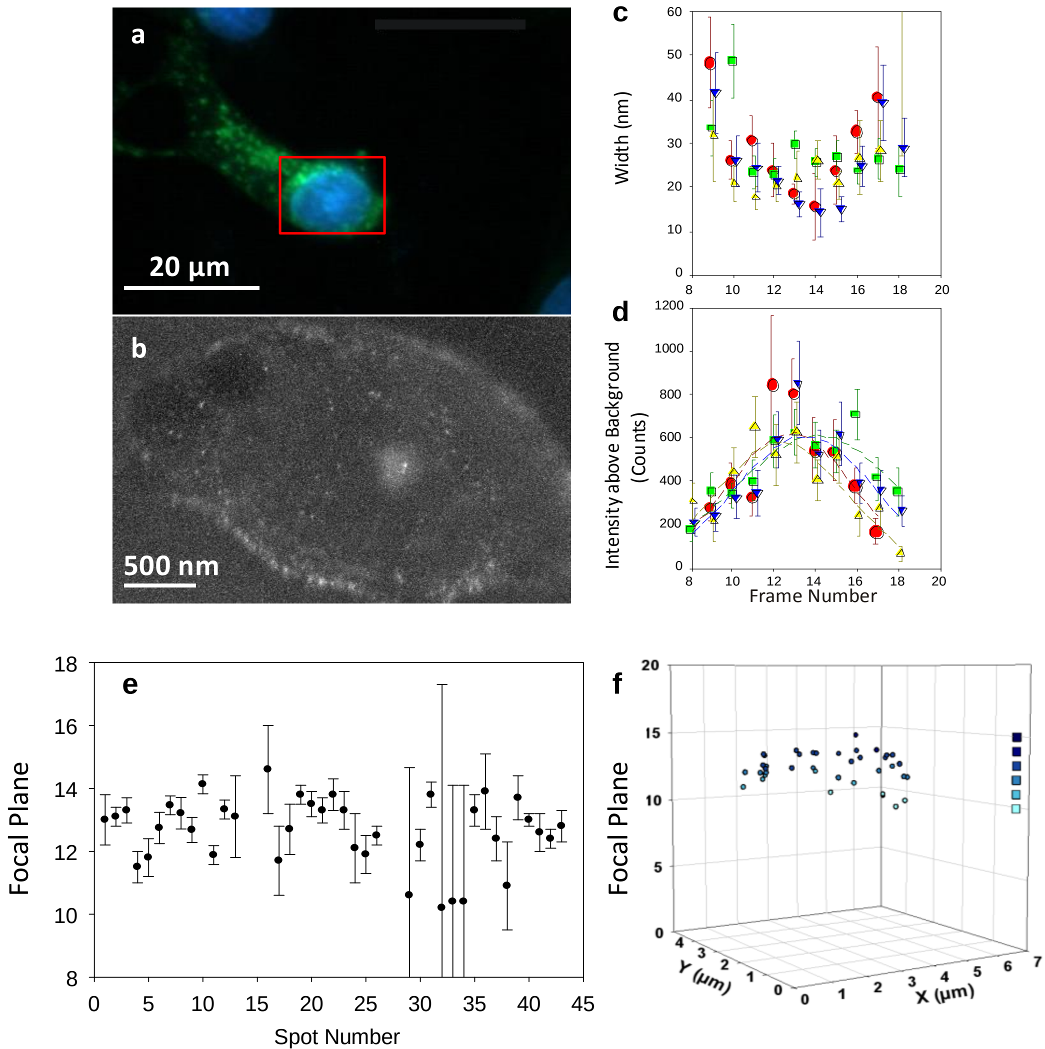

**Figure 3.3.7.1. Analysis of widths and intensities of immunogold labelling throughout an ASEM Z stack.** a) Fluorescence image of B104 neuroblastoma cells transfected with spH and stained with DAPI imaged using the JEOL ClairScope™. b) Z stack projection, showing the complete extent of spH specific immunogold labelling throughout the 3D hydrated cell structure. c) Widths of immunogold particles analysed plotted against focal position. d) Fitted intensity of immunogold particles plotted to determine best focus. Error bars indicate the standard deviation of peak width or intensity found in each Z plane by the fitting algorithm. Dashed lines show best fit of a Gaussian peak to the intensity points, to find the maximum intensity and optimum focal plane. e) Scatter plot of best-fitted focal section for the identified spots. Error bars show standard error found by the fitting process for 40 measurements made on 1 biological replicate (n = 1). f) 3D representation of immunogold labelling distribution throughout the hydrated cell sample.

## 3.4 Discussion

In this project immunofluorescence labelling methods were adapted to incorporate established techniques in fluorescence microscopy followed by *in situ* scanning electron microscopy of the hydrated sample using the novel imaging technology the JEOL ClairScope™. This technology enables *in situ* imaging of the same hydrated sample by both wide field fluorescence and scanning electron microscopy at atmospheric pressure.

### Development of eSRM and immunogold imaging on the JEOL ClairScope™.

20 nm immunogold particles were imaged on the ClairScope™ in order to ascertain the optimum conditions for achieving successful imaging and best resolution. The 20 nm immunogold was adhered to a poly-L-lysine coating on the silicon nitride film window which allowed the acquisition of images at various accelerating voltages and spot sizes. The particles detected in these images were analysed by an algorithm used in the analysis of super resolution microscopy (Morrison et al. 1994). This enabled the width and intensity of each peak to be analysed without the need to convolve the object shape with the electron beam shape, as the particle sizes were close to the resolution limit of the ASEM. This revealed that best resolution was achieved using 30AV and spot size 35. However, the best signal to noise was observed using 20AV and 35SS, although with 30AV the signal-to-noise ratio is still acceptable, with increased intensity above background and improved mean width in comparison to that gained at 20AV. At higher energy potentials more contrast is created, as a higher proportion of electrons were backscattered from the immunogold labelled sample to the detector, although greater sample damage may be caused, due to the generation of free radicals in the hydrated environment. In conventional SEM the SS is larger at lower magnifications, whereas smaller spot sizes are used at higher magnifications to decrease the overall interaction volume and therefore increase resolution. Thus the AV used for each sample may require further investigation if sample damage is likely to be a significant factor.

### 1.4 nm Nanogold labelling of B104 neuroblastoma cells transfected with synaptopHluorin.

In this study, traditional immunofluorescence techniques, where a primary antibody targeted for a specific cellular protein is labelled with a secondary antibody conjugated to a fluorophore, were adapted; electron dense gold particles conjugated to the secondary antibody were used in place of a fluorophore in order to visualise the localisation of fluorescent proteins in hydrated cells, fixed and permeabilised as for standard light microscopy, and then directly correlated with eSRM images using ASEM.

Initial investigations into the immunogold labelling of B104 neuroblastoma cells transfected with synaptopHluorin (spH) involved labelling mouse, anti-GFP primary antibody followed by incubation with 1.4 nm nanogold. The small diameter of the immunogold was considered to be important to ensure passage of the immunogold particle and conjugated secondary antibody through the permeabilised cell membrane and successfully label spH on vesicle lumen membranes. In a study by Nishiyama et al. (2010), the approximate resolution achievable by the ClairScope™ was established as ranging from 8-10 nm, measured by the analysis of a partition between two immunogold particles, or gold/ silver enhancement of metal particles. Therefore probes ideally need to be less than 10 nm otherwise the probes itself becomes the limiting factor when determining resolution. However, visualisation of 1.4 nm Nanogold did not generate sufficient back scattered electrons and so the diameter of the immunogold particle had to be increased. To achieve this gold enhance solution was used to increase the diameter of 1.4 nm Nanogold to 3 -20 nm through the addition of gold ions in solution, which are catalytically deposited as metallic gold on the surface of the Nanogold particles.

It was observed that following the addition of gold enhance solution under several test conditions, Figure 3.3.1.1, contrast was created by deposits of gold enhance across the whole cell. This is particularly evident in Figure 3.3.1.1b which was incubated with gold enhance only, where contrast through the sample and background was observed. This suggests that the gold enhancement of the 1.4 nm immunogold produces non-specific results; chelating methods designed to remove all excess metal ions remaining on the silicon nitride window resulted in no improvement in non-specific enhancement. Due to this complication, extra sample handling and lack of direct imaging, this approach was not deemed ideal for future studies in this investigation. Similar results were observed in studies where primary mouse neurons, megakaryocytes and bone marrow derived dendritic cells were labelled using Nanogold particles and gold enhance, although here the labelling protocol was only required for non-specific labelling for visualisation of cell samples by ASEM, rather than for specific protein localisation (Kinoshita et al. 2014). Although gold enhance produces positive results in the deposition of gold to increase immunogold diameters, the method is not trouble-free due to the non-specific enhancement of background materials and possibly cellular structures, meaning that in this project, specific labelling cannot be readily achieved through this method. Resolution of 8 nm was also determined by measuring the 'apparent' clear distance between two spots, but this may not reflect the true resolution limit when considering two sources of signal in close proximity. For this, the definition of resolution given by Ernst Abbe and the Rayleigh criterion probably reflect a more accurate measurement of achievable resolution of two distinct spots, even within an electron microscope.

**20 nm immunogold labelling of Beta tubulin**

To overcome the requirement of gold enhancement of 1.4 nm immunogold particles, and non-specific results, 20 nm immunogold particles were used. 20 nm gold particles were proven to generate a sufficient signal for imaging when deposited on the membrane itself and thus should generate sufficient signal within biological specimens. In addition, due to low transfection rates in B104 neuroblastoma cells and to enable the development of a successful immunogold labelling protocol, it was decided to label the microtubule protein βIII tubulin, a protein exclusively expressed by neuronal cells (Karki et al. 2013). Heavy metal staining with Uranyl Acetate (UA) was required in the initial studies, to create contrast and facilitate focussing on the cell membrane, as shown in Figure 3.3.2.1. Successful labelling of βIII tubulin gave electron dense peaks against the background of the cell membrane (shown in Figure 3.3.2.2). These peaks were analysed using the SRM algorithm previously described (Morrison et al. 1994), enabling positive identification as immunogold particles from background intensities due to UA staining of the membrane and possible staining artefacts, giving results shown in Table 3.2. Analysis of the peaks showed fairly uniform widths of between 29 to 35 nm, but much greater variable intensities, ranging from 97 to 180 counts above background. The background itself varied from 470 to 840 counts and then was no correlation between this and the particle intensity.

These variances could arise from two operator dependent factors in the imaging process. The first is focus; the small variation in measured width (a mean of 10-30 nm) may be due to less than perfect focus. This effect can be can be seen in the later experiment (Figure 3.3.7.1c) where deliberate defocussing increased the apparent width from 20 nm to almost 50 nm. The background and intensity parameters depend on the contrast and brightness settings, which are chosen to give a good image and are not calibrated. Increasing the contrast in particular (changing the gain of the detector amplifier) will increase the noise in the image. The signal to noise also varies from sample to sample depending on the sample itself, e.g. the UA staining, and hence the background signal; conditions were chosen to give a good image where the particles were clearly seen and focus could be achieved. The intensity was used to identify possible double particles in any one image, which could not be compared between images.

Double particles should give rise to a greater number of backscattered electrons and thus we should be able to identify them on intensity. Potential doubles or aggregates could be seen in the analysis as significantly brighter spots. Unlike fluorescence, where the intensity should double as the excitation photons are not obscured, the intensity of doublets using the e-beam may not increase in a linear fashion due to the variation of the interaction of the interaction volume between the particle and the electron beam, and also if the first particle obscures both the incoming e-beam and emitted backscattered electrons. The use of smaller probes would therefore minimise this problem.

Development of this novel method for the imaging of target proteins in hydrated cells at atmospheric pressure by ASEM has been achieved by a simple immunogold labelling process akin to that used in light microscopy. This builds on, significantly simplifies and removes potential defects shown in similar publications by Nishiyama et al. (2010), Maruyama et al. (2012), Akita et al. (2013) Kinoshita et al. (2014) and Hirano et al. (2014); these studies have shown successful immunogold labelling in hydrated samples using the JEOL ClairScope™, the samples were gold labelled and enhanced with heavy metals to achieve the contrast required for imaging. This may result in the introduction of artefacts and non-specific labelling (Nishiyama et al. 2010a). In this study the successful immunogold labelling of βIII tubulin, confirmed that intracellular immunogold labelling was achievable using 20 nm immunogold particles, although the specificity of the labelling remained undetermined by this method as there is no fluorescence correlation and no distinct pattern or localisation is marked by labelling βIII tubulin meaning the concentration of immunogold labelling is impossible to determine by this method. Control experiments where only the secondary immunogold was applied also showed no immunogold labelling.

### Colocalisation of rhodamine phalloidin with LifeAct YFP.

To optimise the antibody concentration required for immunogold labelling and allow the correlation of fluorescence and atmospheric scanning electron microscopy, U251 glioblastoma cells constitutively expressing LifeAct YFP (Riedl et al. 2008) (a C terminal YFP fusion to 17 amino acids of actin binding protein Abp140) were used. In this system YFP labelling is achieved through the expression and binding to F-actin. The extent of LifeAct YFP binding across all cellular F-actin was investigated by staining with rhodamine phalloidin; Figure 3.3.3.1. It was clearly observed that the antibody could bind the YFP despite the dual labelling. This proved that steric crowding would not be an issue for further studies at similar densities. This was also shown in studies in the the binding dynamics of LifeAct by Riedl et al. (2008), although it must be recognised the 20 nm gold is larger than phalloidin.

To determine if LifeAct YFP-peptide binding to F-actin affects the binding of primary and secondary antibodies used in immunofluorescence labelling by suboptimal binding or steric hindrance, Anti-GFP (clone 3E6) mouse IgG2a, monoclonal antibody (Invitrogen) was applied as primary antibody followed by secondary fluorophore anti-mouse Alexa 594; Figure 3.3.3.1. Complete colocalisation of LifeAct YFP fluorescence with secondary fluorophore fluorescence was observed when the stock anti-GFP primary antibody was used at a dilution of 1:1000 (Figure 3.3.3.1b), this was determined using co-localisation software (Methods section 2.4.8). This provides evidence that colocalisation was complete even if saturation could not be guaranteed. Ideally, flow cytometry study would show the requirements for saturation of binding to each fluorophore (Chattopadhyay et al. 2008). This was an important control to establish; optimal immunogold labelling there should be optimal binding of secondary antibody and no steric hindrance caused by the YFP LifeAct binding to F actin sites. This may affect the binding of immunogold, possibly resulting in poor labelling or detection of false positives.

### 20 nm Immunogold labelling of LifeAct YFP in U251 glioblastoma cells.

As the ClairScope™ is a novel imaging technology the working concentration of immunogold for use in ASEM could only be established by imaging samples labelled samples by the same protocol used for the labelling of βIII tubulin, with varying dilutions of immunogold. This was achieved by imaging U251 glioblastoma cells expressing LifeAct YFP labelled with mouse anti GFP primary antibody and anti mouse 20 nm immunogold particles at dilutions from 1 part in 50 of PBS 1 % (v/v) Triton, to 1 part in 5. Immunogold labelling was observed at a working concentration 1:5; Figure 3.3.3.2aiii. Further increase in concentration of secondary gold conjugated antibody would be impractical. However, 1:5 gave good labelling, but again could not guarantee saturation. Control areas within no fluorescence was observed were imaged and no immunogold labelling was observed, demonstrating specific labelling of YFP actin only.

Further labelling of LifeAct YFP (YFP actin) was carried out on replicate samples. U251 cells were labelled with immunogold and imaged by ASEM; this showed successful labelling of YFP actin filaments with 20 nm immunogold in correlation with fluorescent actin filaments (Figure 3.3.4.1). It was observed that the areas imaged by ASEM in Figure 3.3.4.1, highlighted by coloured boxes do not correlate with areas of brightest fluorescence on the ClairScope™ dish window; this is because the areas which are seen to have brightest fluorescence are cellular structures which are not lying close to the silicon nitride film window. Those cells that are lying close on the silicon nitride film window have less z-depth and appear less fluorescent in comparison. The sparse immunogold labelling may also be due to the high resolution achieved by ASEM, resulting in the detection of gold particles at individual binding sites therefore the filamentous patterns usually observed by fluorescence microscopy are not as easily visualised; the higher the magnification the more spatially distant the particles will appear (Small 1988). This has been determined to be a side binder of F-actin, which has been shown to localise to both actin patches and cables (Moseley & Goode 2006). The regeneration of actin filaments occurs as a ‘treadmill’ of polymerisation at the positive end and disassembly at the negative end, (Holmes et al. 1990; Vishwasrao et al. 2012). Therefore the appearance of sparse immunogold labelling may be due to sub-saturation of binding of immunogold to the primary anti GFP antibody. This could arise if there was insufficient permeabilisation of the cell membrane. This could inhibit the penetration of 20 nm immunogold particles through the membrane and bind to its epitope, or poor affinity of either the primary or secondary antibody (analysis of the peaks is shown in Table 3.3).

It was observed that significant variation in the intensity above background between peaks remains, as also shown in the montage of a selection of electron dense peaks imaged in several of areas of immunogold labelled U251 cells, Figure 3.3.4.1a, which is most likely a result of background UA staining. This variation is expressed further in variation of measured widths and intensity above background. The stacked histogram (3.3.4.1b) showed intensity above background and number of electron dense peaks in each data set. The calculated mean intensity is 270 ± 70 counts with a range from

230 ± 80 to 490 ± 130 with calculated signal to noise ranging from 3.1:1 to 6.5:1. The width expected from the interaction of the electron beam with a 20 nm immunogold particle is not easy to define, but the uniformity of the result shows that the electron dense peaks were individual immunogold particles. Wider widths may be due to possible clustering of particles, which would occur if more than one secondary anti-mouse immunogold antibody bound to an anti-GFP primary antibody. Limitations of sensitivity of the ClairScope™ compared to conventional SEM must also be considered when analysing the electron dense peaks, as the electron beam is scattered on passing through the silicon nitride film window and also by imaging in an aqueous environment at atmospheric pressure.

**Immunogold labelling of B104 neuroblastoma cells transfected with GFP actin**

Following successful immunogold labelling of YFP actin in U251 glioblastoma cells the method was carried out using B104 neuroblastoma cells transfected with GFP actin. To increase the density of immunogold labelling within the permeabilised cell sample and reduce the requirement for heavy metal staining, 15 nm immunogold particles were used, with no heavy metal staining. Successful immunogold labelling of B104 neuroblastoma cells transfected with GFP actin was achieved (Figure 3.3.5.1). Electron dense peaks had a calculated mean width for each electron dense peak of 34 ± 15 nm. The calculated mean intensity was 230 ± 80 counts with a signal to noise ratio 2.85:1 and an overall background value of 230 ± 80 counts. It was observed that there is a wide population of widths Figure 3.3.5.1e, ranging from 20 nm – 60 nm, in comparison to data collected from samples labelled with 20 nm immunogold, where the widths ranged from 29 nm to 35 nm. This variance may be due to the intensity of the immunogold labelling; clearer patterns of labelled actin filaments were visible, although the intensity of labelling complicates analysis of single particles. This intensive labelling may be due to the use of 15 nm immunogold particles. It may be possible that the smaller diameter enabled a greater number of particles to penetrate the cell membrane to bind the target epitope. The intensity of immunogold labelling must also be emphasised as in these samples no heavy metal staining was required for imaging by ASEM.

### Immunogold labelling of B104 neuroblastoma transfected with synaptopHluorin

Immunogold labelling of GFP actin resulted in intense labelling and high contrast images of actin filaments in B104 neuroblastoma cells. This protocol was taken forward for the labelling of B104 neuroblastoma cells transfected with synaptopHluorin (spH), with the aim to use the labelling protocol as a method for identifying vesicle dynamics within differentiated neuroblastoma cells. To achieve good resolution using the ClairScope™, 20 nm immunogold particles were used in each of these experiments with no heavy metal staining.

Successful immunogold labelling was observed throughout samples transfected with spH, (Figures 3.3.6.1 and 3.3.6.2). Analysis of the images (Figures 3.3.6.1 d-f) showed that the overall mean calculated width of peaks analysed was 23 ± 8 nm ranging from 20 ± 4 nm to 25 ± 9 nm, showing little variance. The overall mean intensity above background was calculated to be 460 ± 180 counts above background; however these ranged significantly from 250 ± 110 counts to 730 ± 250 counts, with signal to noise ratios varying from 8.3:1 to 7.3:1. The overall mean background intensity was calculated as 380 ± 50 counts with a range from 240 ± 30 to 650 ± 100 counts. It was observed that although the contrast of the immunogold particles against the background values is increased, the measured widths in each sample remain above 30 nm. As there is no background staining from UA staining the widths must be assumed to be due to the resolution limitations of the ClairScope™ and imaging in a wet environment at atmospheric pressure, which scatters the electron beam and lowers the resolution. Individual immunogold particles are observed demonstrating specific labelling of transfected vesicles and also that the ClairScope™ has the sensitivity to resolve individual 20 nm immunogold particles. Also the contrast created by the 20 nm immunogold is increased in comparison to 15 nm immunogold, as used in GFP actin labelling, which resulted in more successful and clearer analysis of electron dense peaks. Clustering of immunogold particles is observed at the edge of the cell membrane, which may be due to the curvature of the hydrated cell structure, resulting in an increased concentration of vesicles in this focal plane and hence the appearance of clustered immunogold particles, as several particles will be present in the same x, y positions, but different z positions.

### Spatial distribution of immunogold labelling showing localisation of synaptic vesicles with in the cell body

Successful immunogold labelling has been achieved in hydrated cell samples at atmospheric pressure, demonstrating labelling of target proteins with electron dense particles. This allows the visualisation of hydrated cells by fluorescence microscopy whilst improving the imaging resolution to the nanoscale by *in situ* ASEM. Although this imaging method allows the visualisation of cellular organisation in a hydrated state, when only one focal plane is imaged, this produces a snapshot of only one focal plane in the 3D cell. Therefore a method was devised to acquire serial images of sequential focal planes to create a z-stack and reveal the true extent of labelling throughout the entire 3D hydrated cell structure.

B104 neuroblastoma cells transfected with spH were cultured on ClairScope™ dishes and labelled with 20 nm immunogold as previously described, and a z-stack of serial focal planes was acquired using the ClairScope™. Fluorescence images show spH and DAPI staining (Figure 3.3.7.1a), and the highlighted area is shown as a compound image of immunogold labelling throughout the z-stack in Figure 3.3.7.1b. Scatter plots of measured widths and intensities of measured electron dense peaks display the distribution and organisation of vesicles within the hydrated cell body. It is important to observe in Figure 3.3.7.1 that as the focal plane changes the majority of immunogold particles are brought in to focus, seen by a narrowing of peak width between focal planes 13 and 15. Where best possible focus is achieved the average width of particles was calculated as 24 ± 8 nm. This narrowing of peak width is observed in 3.3.7.1d by an increase in intensity inversely proportional to the change in peak width; the maximum intensity is uniform even when peaking in different z-planes. This indicates that the immunogold particles are dispersed across several focal planes, as has been determined by traditional TEM methods of sectioning and imaging of ultrathin sections. This means that results from an ASEM z-stack can be displayed in a manner by which 3 dimensional distribution may be observed.

We can now use this method as a functional application to identify the full population of vesicles present within a differentiated neuroblastoma cells by fluorescence and electron microscopy, overcoming resolution limitations of light microscopy, with the development potential to apply this model system to visualise synaptic vesicles in neuronal synapses. This will complement studies of cell dynamics using fluorescence recovery after photo-bleaching (FRAP) where it has been possible to determine the dynamics of synaptic vesicles within hippocampal boutons (Jordan et al. 2005), although there still remains the requirement for detrimental processing for EM. The method development in this project is an important step in the development of visualisation of synaptic vesicle activity by fluorescence and eSRM. This can significantly expedite correlative imaging processes and produce results with greater precision and negate potential EM artefacts.

## 4.0 Applying methods in correlative light and atmospheric scanning electron microscopy to visualise stimulated cellular activity.

### 4.1 Introduction

Synaptic activity and response to stimulation is crucial in neuronal plasticity, although the true extent of the relationship between presynaptic structural organisation and the functional dynamics within the presynaptic terminal remains unclear. Synaptic vesicles fill the presynaptic terminal; they have uniform shape and size at ~40-50 nm in diameter and contain neurotransmitters such as glutamate and γ- aminobutyric acid (Shulman et al. 2004; Schafer and Jones 1982). Exocytosis and endocytosis of synaptic vesicles occurs in a specialised area of the presynaptic membrane known as the active zone (AZ), resulting in the release of neurotransmitter into the synaptic cleft, a process classically visualised by electron microscopy, as shown in Figure 4.1.1 (Heuser and Reese 1973).

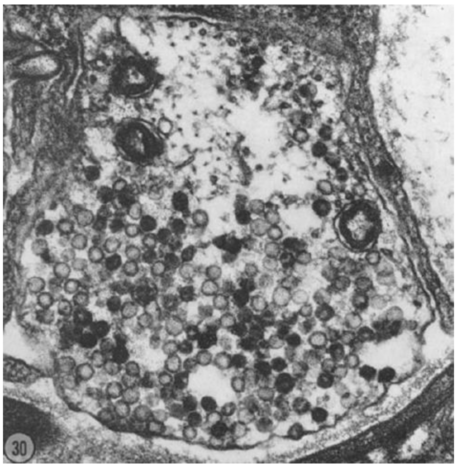

**Figure 4.1.1. Frog neuromuscular nerve terminal containing synaptic vesicles.** Stimulation in the presence of horse radish peroxidase (HRP) shows that some vesicles (dark circles) have undergone exocytosis and endocytosis with the plasma membrane and therefore contain HRP through recycling of the plasma membrane. Image from Heuser & Reese (1973). Disclaimer: Third parties may use our (Journal of Cell Biology) published materials under a Creative Common Attribution-Non commercial-Share Alike 3.0 Unsupported License six months after publication. (Full attribution given in bibliography)).

## Visualising synaptic activity

The distribution and dynamics of vesicles during stimulated synaptic activity have been successfully observed by using fluorescent markers to label vesicle membrane proteins. An example of such is the fluorescent marker synaptopHluorin (spH), a protein fusion of a pH sensitive GFP mutant with the luminal domain of the vesicle associated membrane protein (VAMP), also known as synaptobrevin (Miesenböck et al. 1998). Application of this fluorescent probe has successfully enabled the fluorescent identification of individual synaptic vesicle fusion events at the presynaptic membrane, (Miesenböck et al. 1998).

This is achieved through changes in pH levels; during intracellular stages the vesicular luminal compartment remains at pH 5.5, and hence quenched non-fluorescent state is maintained. On synaptic vesicle exocytosis the lumen bound spH is exposed to the synaptic cleft, where the pH is pH 7.4; this change in pH results in synaptopHluorin fluorescence. This fluorescence is observed until re-acidification of vesicles occurs, following endocytosis, re-establishing the non-fluorescent state. The fluorescent tagging of vesicles by spH has aided the study of active vesicle recycling in hippocampal small synapses under electrical and chemical stimuli (Gandhi and Stevens 2003). Other related studies using fluorescent markers have resulted in the identification of stimulated bulk endocytosis in response to varying stimuli (Clayton, Evans, and Cousin 2008).

Direct measurement of synaptic vesicle turnover has also been studied in the presynaptic terminal by measuring internalisation of fluorescently labelled antibody specific for the luminal epitope of the vesicular protein synaptotagmin (Malgaroli et al. 1995). This ratiometric measure of antibody uptake during incubation with neuronal cells allowed direct measurement of changes in synaptic vesicle recycling activities by immunofluorescence detection during known changes in stimulation. Similarly the internalisation of synaptotagmin specific antibody probes was used to successfully monitor the synaptic vesicle recycling events at cerebellar granule cell synapses in the absence of action potentials. Internalised antibody was labelled with fluorescent markers to reveal the true extent of vesicle recycling and localisation with PKA in the presynaptic terminal in both resting state and stimulated conditions. This enabled measurement of the spontaneous vesicle exocytosis rate in comparison to vesicle dynamics induced by the addition of cAMP (Chavis et al. 1998).

**FM Dyes**

Fluid phase fluorescent markers which bind the presynaptic membrane have played a major role in the study of synaptic vesicle dynamics. An example of such a fluorescent maker is the FM dye, named after Fei Mao, the chemist who originally synthesised the dyes. These are non-toxic, water soluble dyes, which are non-fluorescent when unbound in aqueous media. Their lipophilic head region allows insertion into hydrophobic domains, such as the plasma membrane where they become intensely fluorescent (Wu et al. 2009), as shown in Figure 4.1.2.

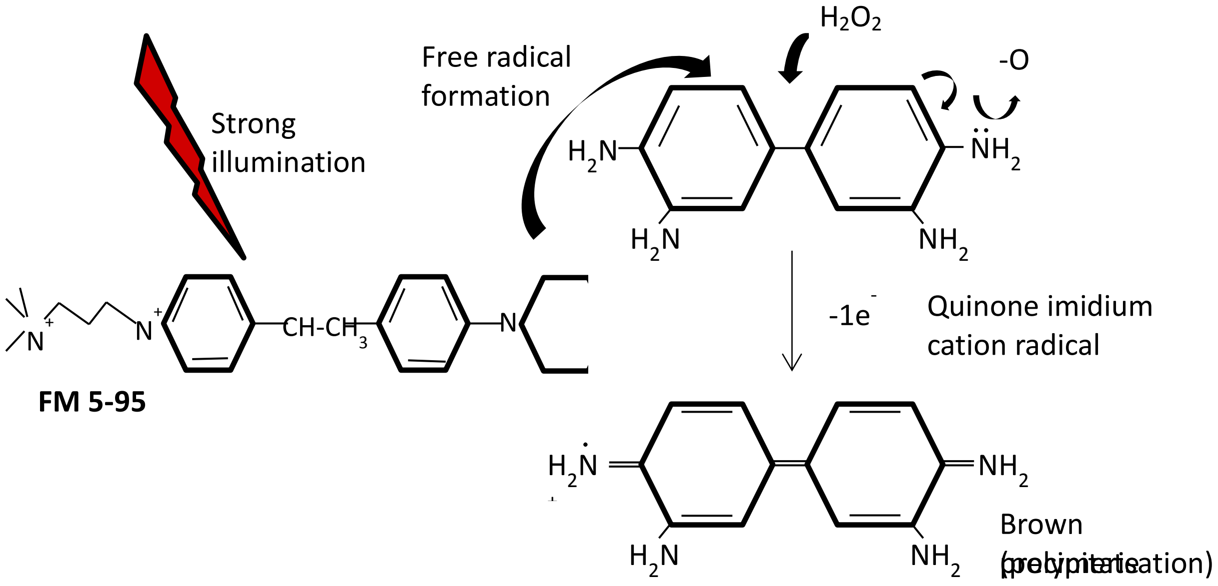

**Figure 4.1.2. FM dye fluorescence and photoconversion.** FM dye fluorescence occurs through the excitation and movement of free electrons ($N^+$ end) which is freed once the dye is inserted in the membrane. Strong illumination in the presence of diaminobizidine (DAB) results in the production of free radicals, which oxidises the DAB in the immediate surrounding environment to form the dark brown complex. (Schematic hand drawn)

FM dyes allow the visualisation of exocytosis and endocytosis by measurement of dye uptake and release from synaptic vesicles during stimulated vesicle recycling. FM dyes have also been used to measure the rate of active synaptic vesicle recycling in both active and silent synapses; the stimulation of active and silent synapses was achieved by treatment with forskolin to increase cellular levels of cyclic adenosine monophosphate (cAMP), which activates synaptic vesicle exocytosis in a protein kinase A dependent manner. This resulted in an increase in active synaptic vesicle recycling and release of neurotransmitter under secondary stimulation (Cousin & Evans 2011).

### Visualising vesicle organisation and localisation at high resolution

FM dyes may also be converted into electron dense material by photoconversion. This is due to the production of free radicals by the fluorophore when under intense illumination. When this occurs during incubation with diaminobenzidine (DAB) the DAB immediately surrounding the dye is oxidised by the free radicals to produce a dark brown electron dense material (Hoopmann et al. 2012) as shown in Figure 4.1.1. This conversion enables analysis of initially fluorescent samples by EM and therefore correlation between fluorescence and structural detail (Hoopmann et al. 2012). This method has been used in the study of the organisation of synaptic vesicles within the presynaptic terminal. This is considered essential for neurons to maintain neurotransmitter release under stimulation. Studies have shown synaptic vesicles localise in distinct ‘pools’ within the presynaptic terminal comprising of the readily releasable pool, reserve pool and the recycling pool (Pieribone et al. 1995). These are supported by interactions between synaptic vesicles and actin filaments. It is thought that these actin filaments undergo structural rearrangements during cell depolarisation, enabling synaptic vesicles trafficking and recycling events (Shupliakov et al. 2002; Tatavarty et al. 2009; Bleckert et al. 2012).

Photoconversion of FM dye has been found to be a robust and reliable method for marking functional synapses or individual recycled synaptic vesicles at the presynaptic

AZ, which has demonstrated that vesicle recycling may not be constrained entirely to individual presynaptic terminals (Harata et al. 2001), but shared between spatially separated neuronal boutons as a mobile superpool (Darcy et al. 2006 and Staras et al. 2010). This approach was also used to study the ultrastructural detail of synapse formation in hippocampal neurons (Nikonenko et al. 2005) and also the organisation of ultrastructure in relation to the function of synaptic vesicle pools (Marra et al. 2014). In a similar study the spatial arrangement of synapses in respect to adjacent recycling pools of synaptic vesicles was imaged by application of FM 1-43. This showed a strong correlation between the number of neighbouring synapses and the size of the recycling pool and its organisation at the presynaptic active zone (Marra et al. 2012). It was also observed that vesicle rich synapses were organised around neighbouring synapses with large recycling pools. This distinct feature was confirmed by the detection of live cell antibody staining in conjunction with synaptopHluorin, further confirming the spatial arrangement of synapses in recycling pools, suggesting a possible link to functional plasticity (Welzel et al. 2010).

A novel method using FM dyes for studying the ultrastructural organisation of synaptic vesicles has seen the incorporation of fluorescence recovery after photobleaching (FRAP) with EM imaging. This enabled vesicle dynamics to be studied via fluorescence, followed by photoconversion and the high resolution observation of areas where FRAP had taken place by EM. This method allowed the localisation of specific vesicles and their function in relation to the cellular ultrastructure (Darcy et al. 2006).

These approaches maintain a reliance on the use of samples processed for transmission electron microscopy, which may not reveal the true extent of vesicle dynamics due to the processing involved. Due to ultra-thin sectioning only a very small representative area, a snapshot of cellular activity, is imaged in each section; this is often expanded upon by imaging serial sections of samples by techniques such as FIB-SEM and SBF-SEM. Such techniques enable the computational assembly of a 3 dimensional representation of labelled proteins throughout a sample, as previously discussed in the introduction. These techniques enable the acquisition high resolution images, although these methods require the production of series of exposed sample surfaces for imaging; these are generally achieved through the milling of the sample by ion beams, there destroying the sample at each new imaging surface. The application of novel technologies such as the JEOL ClairScope™ aim to remove this destructive step in 3 dimensional high resolution imaging. This chapter focuses on applying and adapting the novel high resolution imaging techniques previously developed using the ClairScope™ to visualise the activation dependent recycling of vesicles in hydrated B104 neuroblastoma cells.

## 4.2 Aims and objectives of research described in Chapter 4

Aim: Determine localisation of actively recycled population of vesicles by directly correlative light and atmospheric scanning electron microscopy through photoconversion of FM5-95.

Objectives:

1) Show spH as a marker for activity dependent vesicle dynamics in differentiated B104 neuroblastoma cells by stimulation with 90mM KCl.

2) Develop a method for labelling endocytosis of vesicles in differentiated B104 neuroblastoma cells under stimulation using FM 5-95.

3) Develop a protocol for the photoconversion of FM5-95 by confocal microscopy following stimulation and endocytosis of dye in differentiated B104 neuroblastoma cells cultured on glass coverslips and ClairScope dishes.

## 4.3 Results.

### 4.3.1 Confocal fluorescence microscopy of B104 neuroblastoma cells transfected with synaptopHluorin to visualise synaptic vesicle recycling under stimulation.

In order to visualise synaptic vesicle recycling, organisation and localisation of clustering, a model cell system was used to allow development of imaging protocols. Differentiated B104 neuroblastoma cells were transfected with the pH sensitive mutant synaptopHluorin (spH) and exocytosis was measured as increase in fluorescence. This was achieved through the addition of chemical stimuli such as 90mM KCl, resulting in a change in rise of vesicle pH in the vesicular lumen, shown in Figure 4.3.1.1.

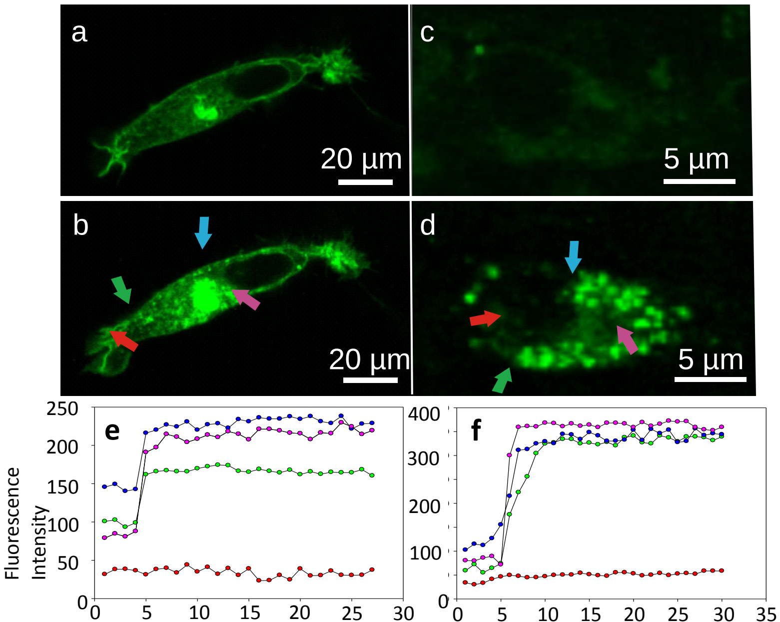

**Figure 4.3.1.1. A measured increase in fluorescence of synaptopHluorin incubation with Ammonium chloride at pH 9.** B104 neuroblastoma cell expressing spH. a) Pre incubation and b) after incubation with Ammonium chloride at pH 9. c) Pre incubation (showing auto-fluorescence) and d) after incubation with 90mM KCl at pH 7.4. Coloured arrows indicate areas measured to assess total fluorescence intensity change in each data set area measured was 4x 4 pixels (3.8 µm), which correspond to measurements shown in e) and f) with increases in fluorescence upon increased pH. For each condition number of biological repeats = 3 and number of areas analysed in each experiment =3. Fluorescent areas are representative of areas of clustered vesicles, fluorescence in pre incubation images is due to autofluorescence.

These results show that due to the change from pH7 to pH 9, vesicles labelled with spH were actively exocytosed and recycled as observed by an increase in fluorescence intensity, shown in Figure 4.3.1.1e by measurements shown in blue, green and pink. Control areas showed no increase in baseline intensities upon exposure to increased pH (Figures 4.3.1.1e and f (red line). 90 mM KCl was also shown to have the same effect as Ammonium Chloride, shown in Figures 4.3.1.1 c, d and f. As this method was established as a working model for visualising actively recycled synaptic vesicles it was carried forward for application in the visualisation of actively recycled vesicles using FM dyes.

### 4.3.2 Confocal fluorescence microscopy of FM 5-95 to visualise synaptic vesicle recycling under stimulation

The application of FM dyes is a direct and ratiometric method that can be used to monitor overall synaptic vesicle recycling. These lipophilic dyes insert into the presynaptic membrane and are endocytosed with cellular membrane upon cell stimulation. This means that the exocytosis of dye containing vesicles may be traced by the measurement of fluorescence decrease as dye is expelled during stimulation.

B104 neuroblastoma cells were cultured on glass slides and differentiated for 5 days in the presence of 1mM cAMP. The cells were loaded with FM 5-95 using a method adapted from a protocol developed by Granata et al. 2008. Uptake of the dye was seen by confocal microscopy as shown in Figure 4.3.2.1. The dye was also seen to be active, as evidenced by a decrease in fluorescence upon stimulation with 90mM KCl (Figure 4.3.2.1 d).

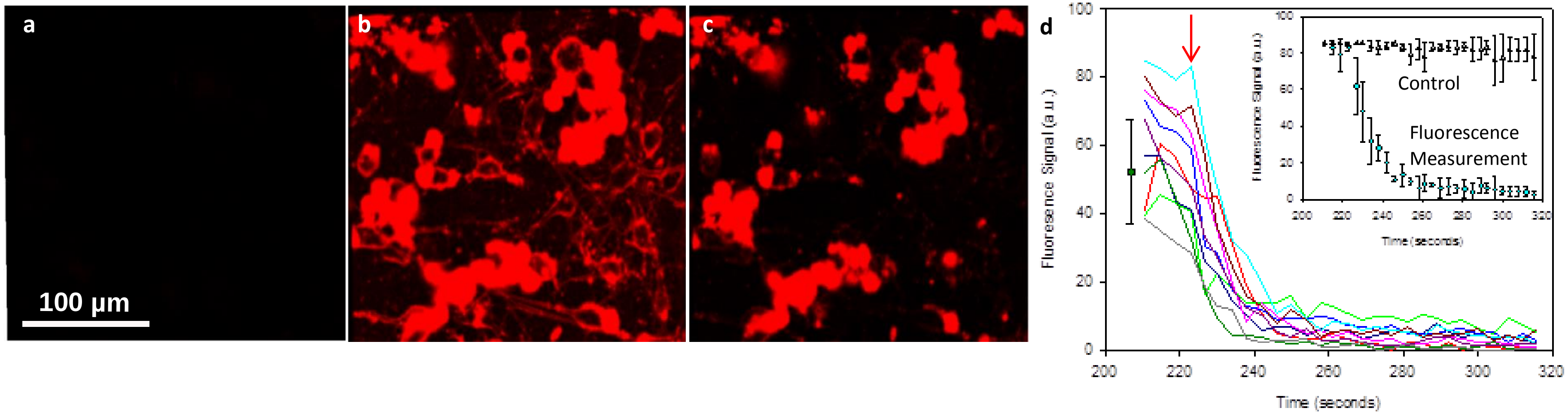

**Figure 4.3.2.1. Stimulated Exocytosis of FM Dye.** (a) Representative fluorescence image prior to addition of FM5-95, no auto fluorescence is seen. (b) Intense fluorescence is observed following addition of dye in stimulation buffer and insertion of dye into cellular outer membrane. (c) Decrease in fluorescence intensity following re-stimulation of cells and exocytosis of FM 5-95 from synaptic vesicle membrane. (d) Fluorescence decrease by stimulated exocytosis of FM dye. A clear decrease in fluorescence in varicosities is recorded following stimulation with 90mM KCl (arrow) shown as coloured line plots. Error bar represents variance in determination of a data point. Inset gives an indication of errors involved in each measurement (circles), and extent of photobleaching for a control area (triangles). Error bars show standard deviation of the mean. Number of biological repeats = 10. Number of areas analysed in each experiment = 10. Fluorescence images over exposed to characterise finer detail in labelled varicosities.

Photoconversion of FM dye to electron dense material by incubation with diaminobenzidine (DAB) has been shown to enable the direct correlation between imaging by fluorescence microscopy and EM in order to correlate FM dye localisation by SEM (Gaffield & Betz 2007). B104 neuroblastoma cells labelled with FM 5-95 were fixed in 4% (w/v) paraformaldehyde, 4% (w/v) sucrose in PBS (0.137 M NaCl, 0.05 M $NaH_2PO_4$, pH 7.4) for 20 minutes at room temperature. For photoconversion cells were incubated in ice cold DAB for 10 minutes. Target regions for imaging were identified and transmitted light images acquired; enabling the identification of FM dye photoconversion by the progressive darkening of dye containing areas. FM 5-95 was photoconverted by illumination with a halogen lamp beam with 488/594 dichroic in place for 10 and 15 minutes in the presence of fresh DAB solution. The target regions were then re-identified and transmitted light images acquired. FM dye converted to electron dense material was seen as darkened areas in transmitted light images (Figure 4.3.2.2) corresponding to the previously fluorescent areas and measured as a change in photo-absorption of between 10 and 50 counts (Figure 4.3.2.2m).

### 4.3.3 Visualisation of actively recycled vesicles by stimulated internalisation of fluid phase markers.

Samples were prepared and imaged by TEM, following methods previously shown to be successful for the visualisation of photoconverted dye in neuronal cells (Hoopmann et al. 2012). To validate the labelling of vesicles in stimulated differentiated neuroblastoma cells by photoconversion of FM dye, B104 neuroblastoma cells were cultured on Melinex film and stimulated in the presence of FM5-95 with 90mM KCl and fixed. Photoconversion was visualised by microscopy and observed by a darkening of previously fluorescent areas after incubation with diaminobenzidine (DAB) and exposure to a mercury lamp beam with 488/594 dichroic in place. Sections were imaged prior to staining with lead citrate and uranyl acetate to identify any areas of electron dense photoconverted FM dye, and again post staining as shown in Figure 4.3.3.1. As observed in Figure 4.3.3.1 vesicles of ~80 nm in diameter were visible in samples which had undergone photoconversion and heavy metal staining

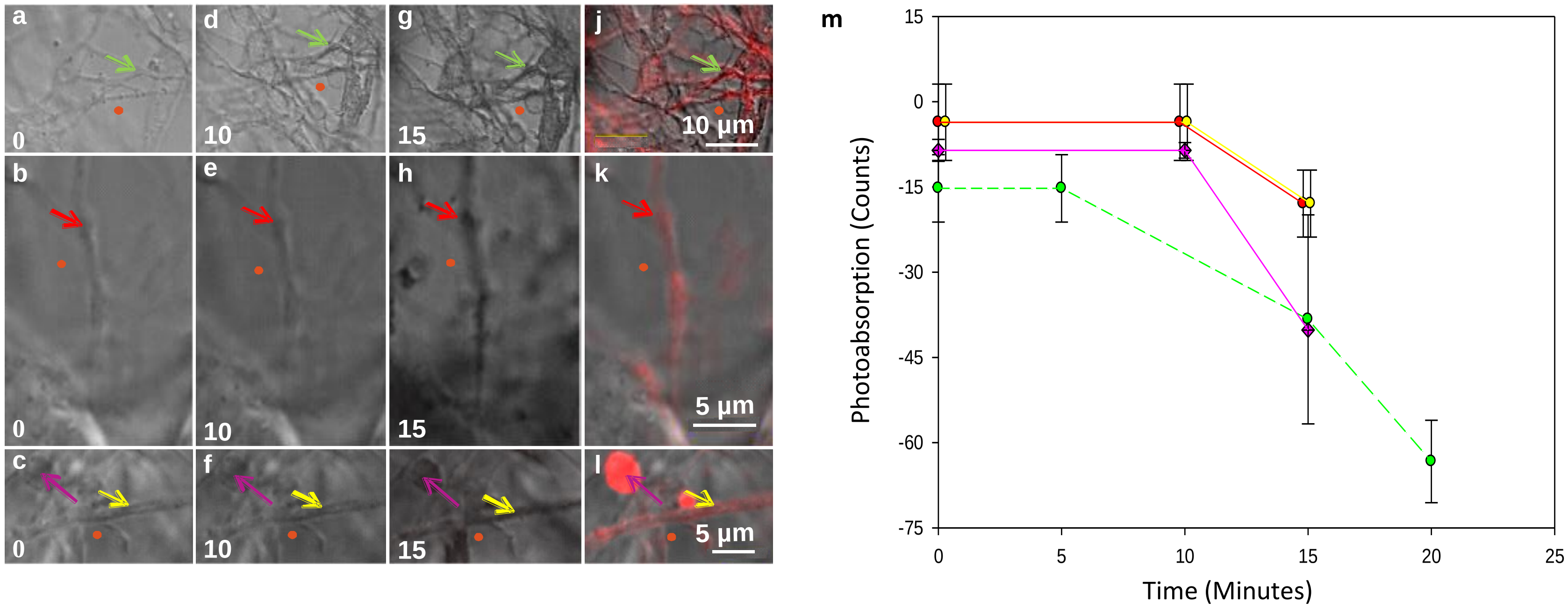

**Figure 4.3.2.2. FM dye photoconversion by confocal microscopy.** Representative images. (a-c) Transmitted light images of differentiated B104 neuroblastoma cells. (d-i)Transmitted light image of the areas in a-c following photo -oxidation by incubation with DAB and illumination by a mercury lamp for 10min (d-f) and 15 min (g-i). (j-l) Transmitted light image with fluorescence overlay. m) Total change in photoabsorption following photo–oxidation (minus background absorbance) in areas indicated by coloured arrows. An extra measurement at 20min shows the continued photo-oxidation following continued fluorescence illumination. Orange spots indicate areas of background measurements. Error bars show standard error of the mean.  Number of biological repeats = 10. Nuber of areas analysed in each data set = 3.

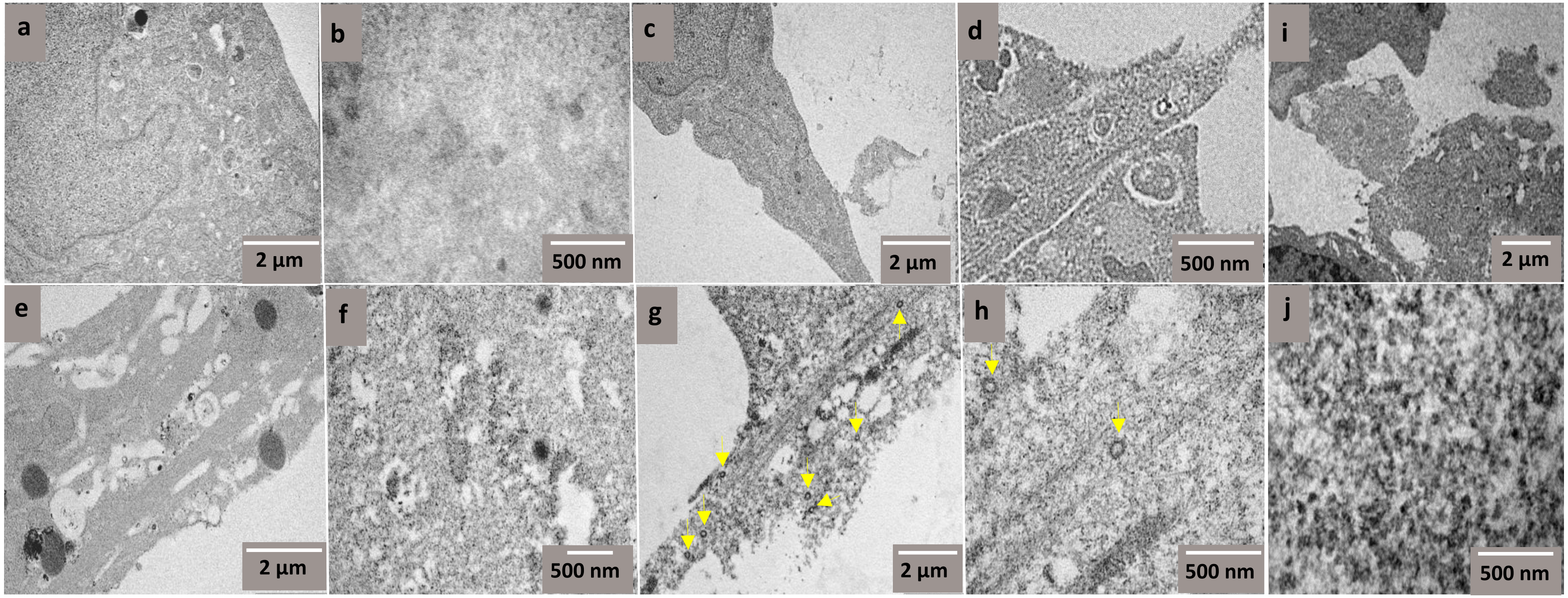

**Figure 4.3.3.1**. **Stimulated endocytosis and photoconversion FM 5-95 imaged by transmission electron microscopy.** a)- b) TEM images of B104 cells following stimulation by 90mM KCl in the presence of FM5-95 and no photoconversion and no heavy metal stain. c)- d) B104 cells following stimulation by 90mM KCl in the presence of FM5-95 and no photoconversion after staining with Uranyl acetate and Lead citrate. e)- f) TEM images of B104 cells following stimulation by 90mM KCl in the presence of FM5-95 after photoconversion with no heavy metal stain. g) -h) B104 cells following stimulation by 90mM KCl in the presence of FM5-95 after photoconversion with DAB, stained with Uranyl acetate and Lead citrate. Vesicles appear ~80nm, indicated by arrows. i)- j) TEM images of B104 cells following stimulation by 90mM KCl in the absence of FM 5-95 after photoconversion with DAB and staining with Uranyl acetate and Lead citrate

TEM of samples which had undergone both photoconversion and heavy metal staining showed electron dense spots. Control samples where no photoconversion or heavy metal staining took place, had no electron dense spots present.

### 4.3.4 Photoconversion of FM 5-95 imaged by fluorescence and correlative ASEM on the JEOL ClairScope

Detection of recycling vesicles by photoconversion of FM5-95 was attempted in B104 neuroblastoma cells cultured on ClairScope dishes, to visualise the electron dense material and indicate the localisation of actively recycled vesicles during stimulation at the presynaptic terminal by directly correlative fluorescence microscopy and ASEM. Photoconversion of FM dye was observed by an increase in absorption when recorded by transmitted light microscopy, as shown in Figures 4.3.4.1. a)-f).

Areas of interest were imaged by ASEM to enable the visualisation of any electron dense material created by photoconversion of FM dye; no electron dense material was observed, as shown in Figures 4.3.4.1c and g. To increase contrast and enable focussing on cellular structures the samples were stained with 0.001% (w/v) uranyl acetate and areas of correlating fluorescence and photoconversion were located and imaged on the ClairScope, Figures 4.3.4.1d) and h). Staining with uranyl acetate created regions of contrast and enabled the outline of the cell membrane to be identified by ASEM, although there were no structures obviously identifiable as clusters of synaptic vesicles. The areas containing electron dense material, intensely bright areas observed in Figure 4.3.4.1d and h show UA stained structures, which are too large to be identified as vesicle clusters, also these areas were only visible through UA staining.

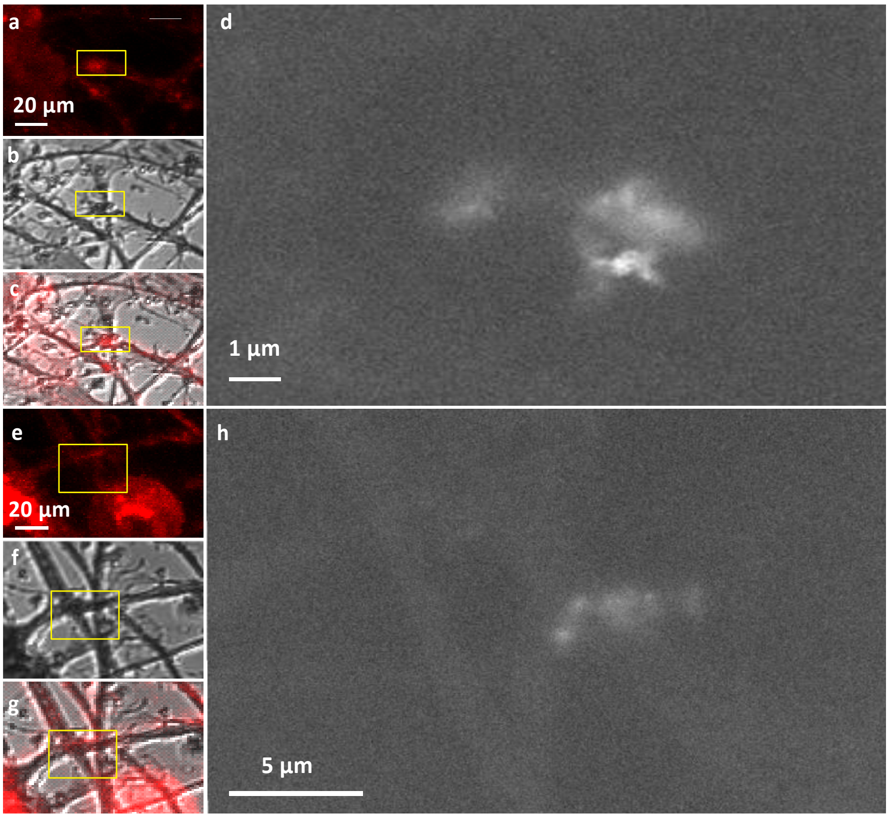

**Figure 4.3.4.1. Photoconverted FM 5-95 following stimulated endocytosis, imaged on the JEOL ClairScope.** a) Fluorescence image acquired by confocal microscopy of B104 cells following stimulation in the presence of FM 5-95 (red) and fixation with 4% PFA/ 4% sucrose on a ClairScope dish. b) Transmitted light image of the same field of view as in a) showing darkened areas of photoconversion. c) Overlay of FM 5-95 fluorescence image in a) with transmitted light image shown in b). d) ASEM image of electron dense areas corresponding to highlighted areas in a) –c). e) Fluorescence image acquired by confocal microscopy of B104 cells following stimulation in the presence of FM 59-5 (red) and fixation with 4% PFA/ 4% sucrose on a ClairScope dish. f) Transmitted light image of the same field of view as in e) showing darkened areas of photoconversion. g) Overlay of FM 5-95 fluorescence image in e) with transmitted light image shown in f). h) ASEM image after UA staining of electron dense areas corresponding to highlighted areas in e) –g).

### 4.3.5 Photoconversion of FM 5-95 imaged by fluorescence and correlative ASEM on the FEGSEM

In order to increase resolution and sensitivity this experiment was repeated using cells cultured in Quantomix capsules and imaged using a JEOL 7600 FEGSEM; the results shown in Figure 4.3.5.1. After UA staining membranous structures were observed (UA interacts with lipids and proteins), using the FEGSEM with a low angle backscatter electron (LABE) detector (Figure 4.3.5.1 d,e,f) which were correlated to previously fluorescent areas. This resulted in clearer correlation between fluorescence and scanning electron micrographs and enabled the correlation of fluorescence with possible electron dense intracellular structures (Figures 4.3.5.1a to e). As in the ClairScope results, there are no structures which could represent clustered or recycled synaptic vesicles (Figure 4.3.4.1). However, intensely electron dense clusters within the fluorescently labelled cell body were observed (Figure 4.3.5.1f). These were compared with control images where no photoconversion was carried out. Here, there were similar electron dense particles in both ClairScope and FEGSEM data. These do not display peri-nuclear clustering; instead they are more dispersed across all control cells and suggest the structures observed are stained membranes or artefacts of UA staining.

These results show that FM 5-95 dye can successfully be used as a marker for endocytosis in stimulated neuroblastoma cells enabling visualisation of endocytosis by fluorescence microscopy. Photoconversion of the dye for visualisation of electron dense material was shown to be successful by fluorescence and transmission microscopy, but not suitable for detection by EM in a hydrated environment. No areas of electron dense material were observed that could be distinguished from UA staining artefacts to be clearly identified as vesicles containing photoconverted FM dye. Control images showed similar UA staining similar to those in samples containing photoconverted FM dye (Figure 4.3.5.2), further verifying that vesicles containing FM could not be positively identified by this imaging method.

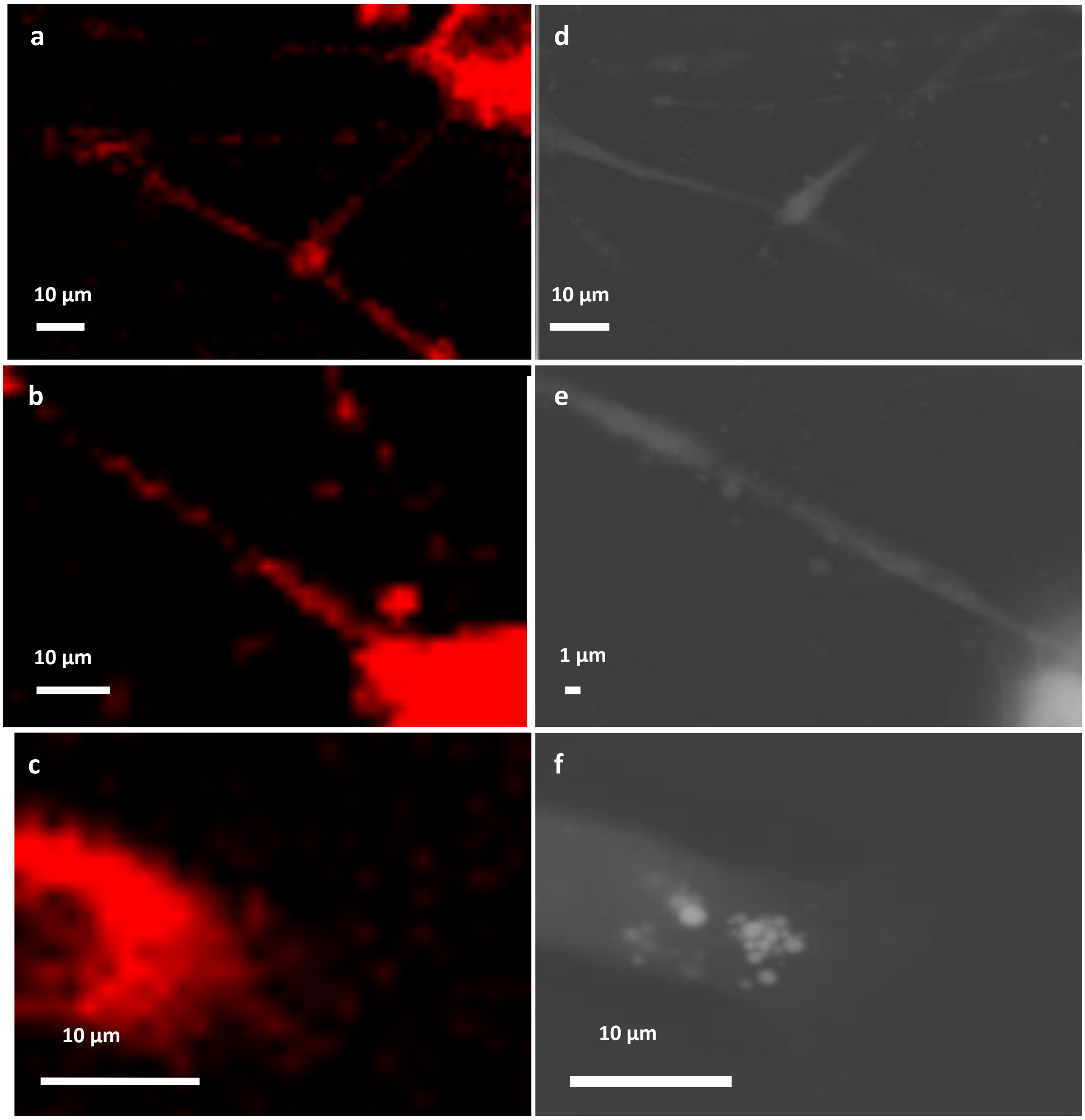

**Figure 4.3.5.1. Correlative fluorescence and FEGSEM images of B104 cells cultured in Quantomix capsules following FM dye photoconversion.** a)-c) show confocal fluorescence images of B104 neuroblastoma cells loaded with FM 5-95 following UA staining. d)-f) Show the same field of view following FM dye photoconversion imaged on a FEGSEM. d) 1,900x, e) 4,500x and f) 20,000x magnification.

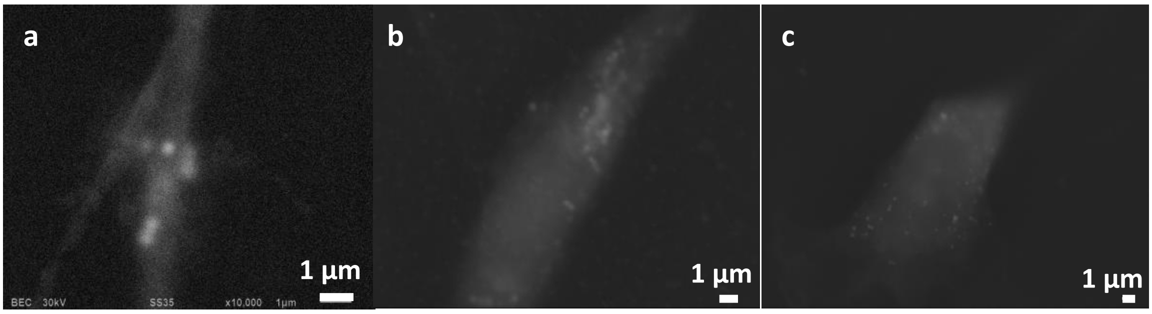

**Figure 4.3.5.2. Imaging UA staining only in FM dye loaded samples.** a) UA staining only on B104 cells where no photoconversion took place, imaged on the ClairScope. b) and c) UA staining only, imaged on a FEGSEM at 5,000x and 3,000x magnification respectively.

### 4.3.6 Intracellular localisation of synaptic vesicles visualised by stimulated antibody internalisation.

Actively recycled vesicle turnover can be identified by measuring internalisation of fluorescently labelled antibody (Malgaroli et al. 1995 and Chavis et al. 1998). An adaptation of these methods was used in order to identify the actively recycled vesicle population by the specific internalisation of anti-GFP primary antibody by B104 neuroblastoma cells transfected with the GFP mutant spH. Two approaches were investigated to optimise this protocol; one approach involved 30 second stimulation with 90mM KCl in the presence of the primary anti-GFP antibody at 37˚C only. The second approach included a 1 hour incubation of primary antibody at 37˚C prior to 30 second stimulation with 90mM KCl. A negative control was included where anti-FLAG (FLAG protein not endogenously present in samples) antibody was substituted for anti-GFP to determine the specificity of antibody internalisation. Results are shown in Figure 4.3.6.1.

Internalisation was studied further by colocalisation studies using Volocity software (PerkinElmer) as described in Methods section 2.4.8. This analysis examined the colocalisation of GFP fluorescence from the cellular spH with fluorescence from secondary labelling of GFP with Alexa 594 anti GFP secondary antibody. The results of the permeabilised and non-permeabilised images, when studied using Pearson's coefficient, a method for statistical determination of co-localisation (as described in Methods section 2.4.8) in Figure 4.3.6.1c, showed little difference and thus suggests a proportion of the antibodies remained membrane bound. However, colocalisation was not seen in other control experiments in stimulated samples. Data was also generated to identify threshold levels and areas of co-localised labelling, this is shown as an intensity profile as seen in Figure 4.3.6.2b. Negative controls using FLAG primary were carried out under identical conditions.

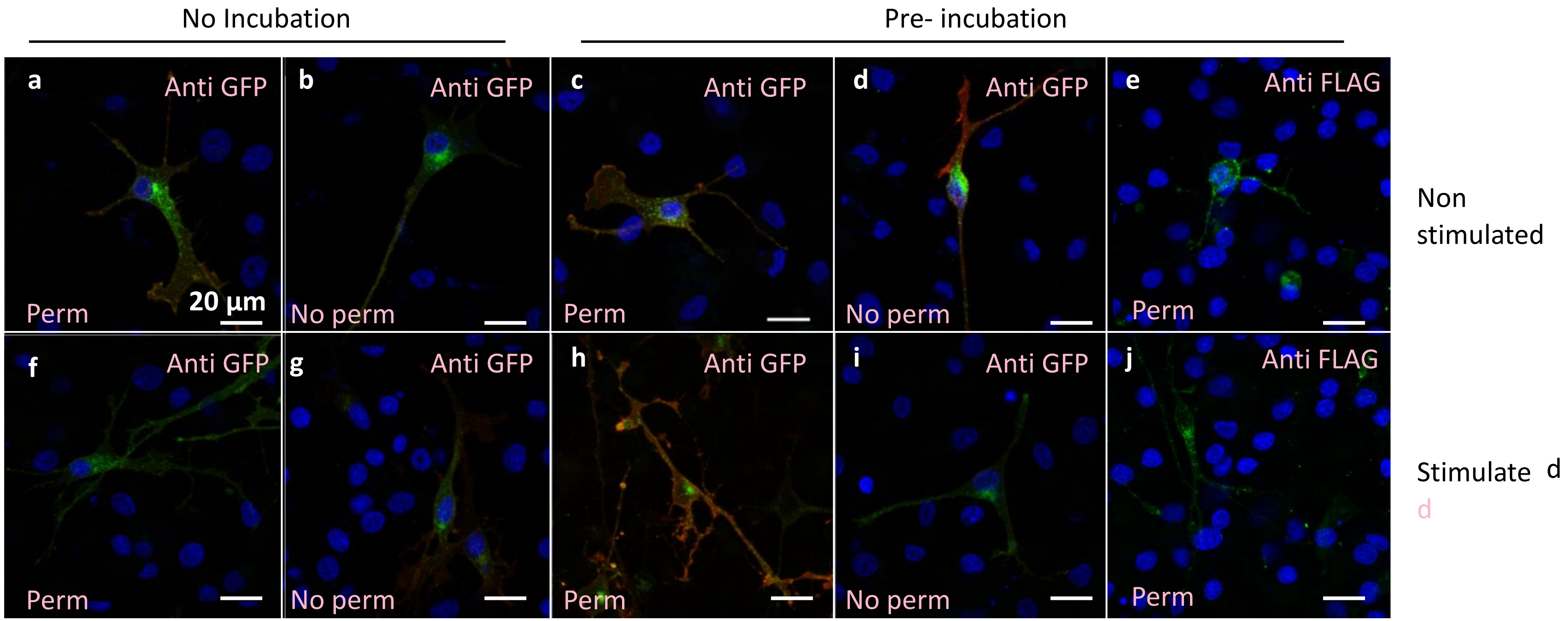
No Incubation
Pre- incubation
a
Anti GFP
Perm
20 µm
b
Anti GFP
No perm
c
Anti GFP
Perm
d
Anti GFP
No perm
e
Anti FLAG
Perm
Non stimulated
f
Anti GFP
Perm
g
Anti GFP
No perm
h
Anti GFP
Perm
i
Anti GFP
No perm
j
Anti FLAG
Perm
Stimulate d
d

**Figure 4.3.6.1. Internalisation of anti-GFP primary antibody in differentiated B104 neuroblastoma cells**. SpH fluorescence is observed by green fluorescence. Internalised anti-GFP antibody is labelled with secondary anti-mouse Alexa 594 following permeabilisation with 1% (v/v) Triton. **Samples a)- e) underwent no stimulation with 90mM KCl**. a) Permeabilised cells incubated with anti GFP antibody at 37˚C at a concentration of 1/100. b) Non- permeabilised cells incubated with anti GFP primary antibody at 37˚C at a concentration of 1/100. c) Permeabilised cells labelled with anti GFP primary antibody following a 1 hour pre-incubation period with primary antibody at a concentration of 1/100 at 37°C. d) Non- permeabilised cells labelled with anti GFP primary antibody following a 1 hour pre-incubation period with primary antibody at a concentration of 1/100 at 37°C. e) Permeabilised cells labelled with anti FLAG primary antibody following a 1 hour pre-incubation period with primary antibody at a concentration of 1/100 at 37°C. **Samples f)- j) were stimulated with 90mM KCl in the presence of primary antibody for 2 minutes at 37˚C.** f) Permeabilised cells incubated with anti GFP antibody at 37˚C at a concentration of 1/100. g) Non- permeabilised cells incubated with anti GFP primary antibody at 37˚C at a concentration of 1/100. h) Permeabilised cells labelled with anti GFP primary antibody following a 1 hour pre-incubation period with primary antibody at a concentration of 1/100 at 37°C. i) Non- permeabilised cells labelled with anti GFP primary antibody following a 1 hour pre-incubation period with primary antibody at a concentration of 1/100 at 37°C. j) Permeabilised cells labelled with anti FLAG primary antibody following a 1 hour pre-incubation period with primary antibody at a concentration of 1/100 at 37°C

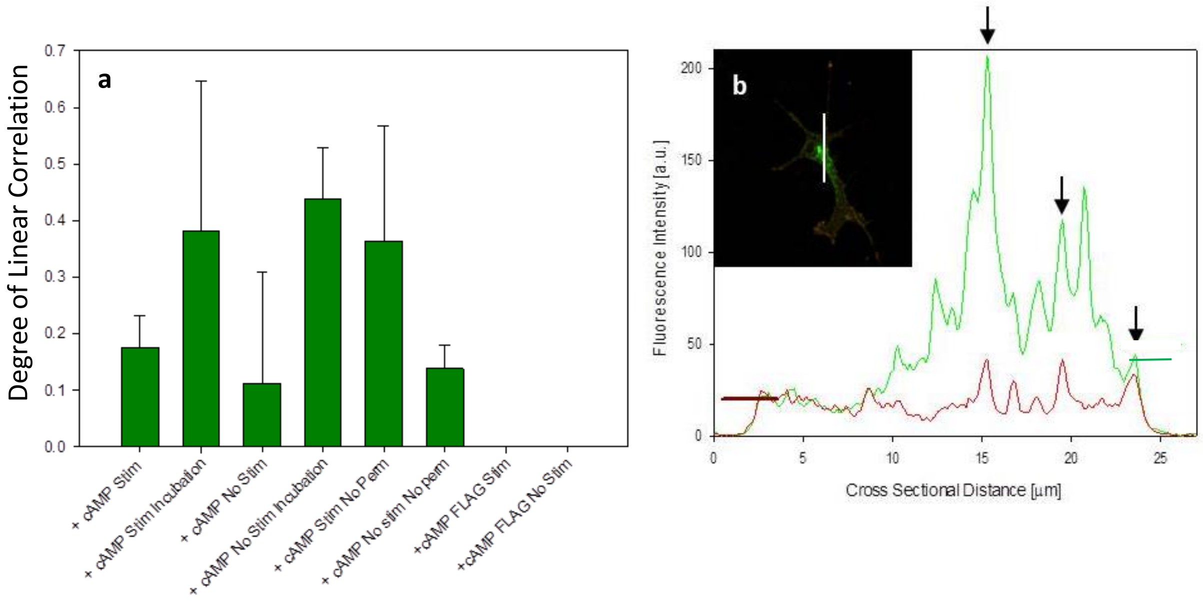

**Figure 4.3.6.2. Colocalisation analysis of spH and Alexa 594 labelling internalised anti-GFP primary antibody in differentiated B104 neuroblastoma cells.** a) Plot showing Pearson's correlation coefficient of colocalisation spH fluorescence with Alexa 594 labelled internalised anti-GFP antibody. Control samples are shown also where anti-FLAG was used as primary antibody for internalisation. Error bars show standard deviation of the mean (n = 30 for each condition). b) Line plot showing the fluorescence intensity of a cross section of an example sample (inset). Threshold values applied during colocalisation analysis are indicated by red and green horizontal bars. Arrows indicate areas of fluorescence intensity colocalisation.

Colocalisation analysis (4.3.6.2a) suggests that anti-GFP antibody was specifically bound by B104 neuroblastoma cells transfected with spH, as control experiments where anti-FLAG replaced the anti-GFP antibody showed no stimulated internalisation. There is a proportion of anti-GFP antibody which was observed to label the membrane of both permeabilised and non-permeabilised cells, although again this was specific only to transfected cells. It was also observed that there was increased colocalisation in samples which were incubated with primary antibody prior to stimulation. No significant difference was seen between the colocalisation of fluorescent labelling in each condition. Cells which were stimulated after no pre-incubation with anti- GFP primary antibody showed no significant difference to those which were not stimulated. A similar trend was observed in the samples which underwent pre- incubation with primary antibody; samples which were stimulated showed no significant difference to samples which were not stimulated. This suggests that only a small amount of primary anti- GFP primary antibody is internalised during stimulation, and also that during periods of pre- incubation primary antibody may bind to surface expressed spH, resulting in inconclusive results. Fluorescence cross-sections of an example cell and the threshold levels set during analysis to determine the fluorescence intensity required for specific colocalisation are shown in Figure 4.3.6.2b. This also shows areas of colocalisation of fluorescence across the cell, indicated by arrows. The thresholds set for each fluorescent marker are set at different levels to compensate for a non-uniform background due to the difference in fluorescence intensities. This method was then taken forward for application with immunogold particles and imaging on the ClairScope, as the large areas of colocalisation following pre-incubation would provide areas for clear labelling and imaging.

Cells were cultured on ClairScope dishes and transfected with spH, the cells were then incubated with primary anti-GFP antibody for 1 hour prior to stimulation in the presence of anti-GFP antibody, as previously described. The samples were then fixed and internalised mouse, anti-GFP primary antibody was labelled with anti mouse 20 nm immunogold. Samples were then imaged by ASEM; no immunogold labelling was observed (Figure 4.3.6.3). Figure 4.3.6.3 shows the highest magnification imaging could not be achieved due to lack of contrast in the cell samples.

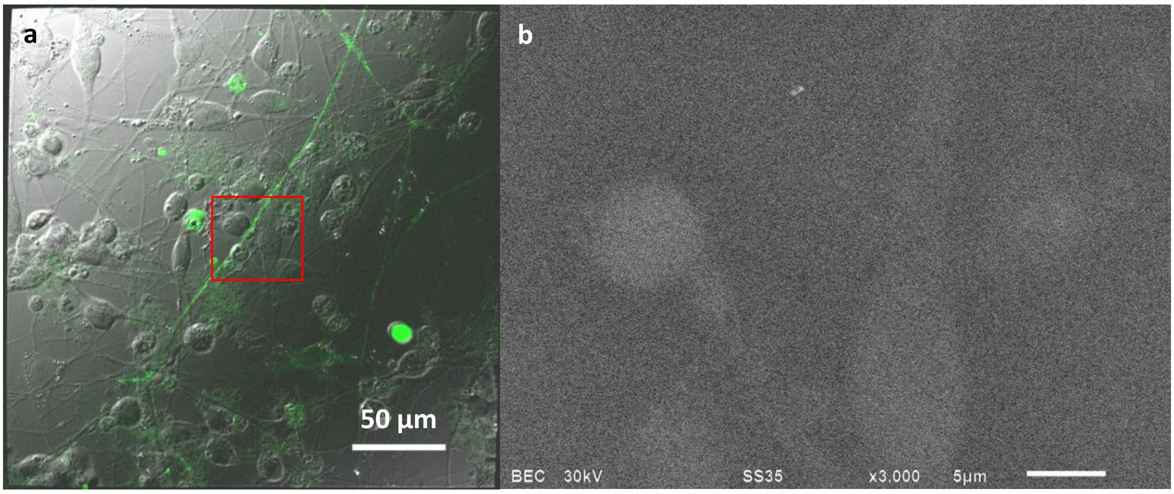

**Figure 4.3.6.3. Specific 20 nm immunogold labelling of internalised anti GFP primary antibody in differentiated B104 neuroblastoma cells transfected with spH.** a) Fluorescence image of differentiated B104 neuroblastoma cells transfected with spH acquired using a 40x NA 0.8, WD lens on a Zeiss 510 upright confocal microscope. b) Example of an area, highlighted in a) imaged by ASEM on the JEOL ClairScope.

## 4.4 Discussion

### Stimulation of B104 neuroblastoma cells transfected with synaptopHluorin with 90mM KCl.

Recycling of vesicles in the neuronal cell is described as the fusion of vesicles at the plasma membrane of the presynaptic terminal and exocytosis, followed by endocytosis of the vesicles and trafficking within the presynaptic terminal for sorting, replenishment of neurotransmitter and subsequent exocytosis (Heuser & Reese 1973). SynaptopHluorin (spH) is a fusion protein of pH sensitive mutant of GFP with the luminal domain of the membrane protein Vesicle Associated Membrane Protein 1 (VAMP1), also known as synaptobrevin (Miesenböck et al. 1998). Stimulation of vesicles labelled with lumen bound spH occurs when the lumen of the vesicle is exposed to a change in pH, from intra luminal pH5.5 to pH7.4 in the synaptic cleft (Miesenböck et al. 1998). This activation of a fluorescent label enables the specific labelling of actively recycling vesicles within stimulated differentiated cells (Denker et al. 2011), and was replicated in these studies (Figure 4.3.1.1). Upon application of ammonium chloride at pH9 there is an increase in measured fluorescence intensity in the lumen (Figure 4.3.1.1b) due to the change in pH of the local cellular environment. Addition of ammonium chloride produced a change in local pH which was seen as an increase in fluorescence intensity. Similarly the addition of 90mM KCl produced an increase in fluorescence intensity (Figure 4.3.1.1.c and d), but here this was due to the stimulation of vesicle exocytosis. Therefore, the increase in florescence intensity is dependent on the exposure of spH to the higher pH when the lumen is exposed in the synaptic cleft during vesicle fusion. These results confirm that synaptopHluorin can be used to detect when vesicles are exposed to the synaptic cleft. However, it is also important to identify vesicles after endocytosis. For this purpose a fluorescent tag must be taken up during endocytosis for visualisation by fluorescence microscopy.

### Labelling vesicles with FM 5-95 to visualise stimulated synaptic vesicle recycling by confocal microscopy

The use of FM dyes as a fluid phase fluorescent marker for the labelling of recycling vesicles under stimulation has been shown to be a robust and effective method in recent studies of the ratiometric measurement and localisation of vesicle dynamics (Branco et al. 2008, Ratnayaka et al. 2011, Marra et al. 2014). In this study an adaptation of a method published by Granata et al. 2008 was used, which enabled the loading of FM dye by stimulated endocytosis and re-stimulation of membrane bound dye in differentiated neuroblastoma cells (Figure 4.3.2.1b- d). A decrease in fluorescence upon re-stimulation was seen after analysis of regions of fluorescence intensity within varicosities of differentiated B104 neuroblastoma cells. This decrease in fluorescence reflects the dissociation of FM 5-95 from the vesicle membrane upon fusion with the presynaptic membrane, as shown in previous studies (Branco et al. 2008). The change in fluorescence intensity in the stimulation dependent manner suggested successful uptake and stimulated release of actively recycling vesicles within the *en-passant* boutons (a non-terminal synaptic junction made between two axons before continuing to the terminal synapse) (Binder et al. 2009). The FM 5-95 will allow identification of the actively recycled vesicles by fluorescence microscopy. To enable correlation of this information with higher resolution images, it is necessary to mark these vesicles for electron microscopy.

### Photoconversion FM 5-95 following stimulated endocytosis

FM dyes have properties which enable imaging by both fluorescence microscopy and electron microscopy, as they may be converted from fluorescent markers to electron dense material by photoconversion (Nobutoshi Harata et al. 2001). Thus FM dyes may be used as fluorescent markers by newly endocytosed vesicles during live cell imaging, and then correlated to electron microscopy after photoconversion into electron dense material. Photoconversion was achieved *in situ* by incubation with stable diaminobenzidine (DAB) and intense illumination, after which dark brown areas were seen in transmitted light images in areas where fluorescence was previously observed (Figure 4.3.2.2).

Photoconversion of FM dyes was validated by transmission electron microscopy (TEM). This identified successful photoconversion of FM dye to electron dense material by DAB (Figure 4.3.3.1), and gave high resolution images of the DAB staining pattern. Areas of electron dense material were clearly visible in neuronal processes of differentiated B104 neuroblastoma cells forming patterns that were similar to those observed in studies by Marra et al. 2012. The distinct circular staining patterns were clearly visible where synaptic vesicles were present at the presynaptic terminal. It must be appreciated that here only a very small representative volume is imaged in this 70 nm thin section; although multiple points are examined, it may still not reflect the true 3 dimensional structural detail. To increase the usefulness of this, techniques such as FIB and 3View (Gatan) could be used to study of 3D volumes at this high resolution. FIB would mill away the block face revealing previously un-imaged sections with the resolution of each milling step typically 10’s of nanometers, whilst 3View performs microtoming of sections within the SEM with the sample remaining in situ.

As successful photoconversion was observed by fluorescence microscopy and TEM, the method was repeated on samples prepared on ClairScope dishes. Unfortunately, electron dense areas could not be correlated with areas of high fluorescence emission. This may have been due to the converted material not being sufficiently electron dense to generate backscattered electrons to the detector in this environment. The lack of contrast made finding the correct focal plane difficult which compounded the problem of finding regions of interest. In order to increase contrast levels the samples were stained with Uranyl Acetate, which made focussing possible; areas of correlating fluorescence and photoconversion were located and imaged on the ClairScope as shown in Figures 4.3.4.1d) and h). From these results it is possible to see the outline of the cell membrane identified by ASEM, although there are no structures clearly identifiable as clusters of vesicles containing electron dense material, which would be observed as intensely bright areas. This may be a result of the DAB not generating a significant number of backscattered electrons in this environment, as the electron beam will be at a lower density due to beam broadening, and hence the back scattered electrons may have significantly lower intensity. This could result in very few backscattered electrons passing back through the sample to the detector.

Further work was carried out to investigate whether increased detector sensitivity would improve the imaging potential of converted FM 5-95 labelled vesicles within the 3 dimensional, hydrated cells. The JEOL FEGSEM 7600 was used in place of ASEM, to achieve greater sensitivity and resolution compared to the ClairScope due to the use of smaller beam diameter and greater range of detectors. Quantomix capsules were also used to create a hydrated closed environment in which cell samples may be cultured and imaged at atmospheric pressure within a conventional scanning electron microscope (Katz et al. 2007). Imaging of the cells loaded with converted FM5-95 revealed electron dense material, but low levels of contrast remained a problem, therefore UA staining was again used to expedite focussing and generate higher quality images, as a result of the lower electron beam exposure. Peri-nuclear areas of electron dense particles could be seen within the cell (Figure 4.3.5.1). However, in control samples where no FM dye is present these electron dense areas are still present. This suggests that the electron dense areas are an artefact created by UA staining rather than areas of FM dye photoconversion. FM photoconversion cannot be excluded as it was shown to be successful by fluorescence microscopy and EM, but the inherent low contrast that is generated in the liquid environment makes imaging near impossible by ASEM.

Typically DAB is used in imaging to absorb electrons in TEM, where a dehydrated thin section is imaged under vacuum, ensuring all interaction of the electron beam with the sample is detected. In ASEM the electron beam must pass through the wet imaging environment into the hydrated cell, to an area of sample containing electron dense material, preferably lying completely flat on the silicon nitride film window. This allows the electron beam to pass through the window directly to the hydrated sample, and any highly electron dense areas will cause greater backscatter and hence greater signal intensity. Therefore, if only a small population of vesicles incorporated the dye on exocytosis it is possible that this small group may not all be lying flat on the silicon nitride window, but are suspended within the cell. Therefore, due to these issues this method was considered unsuitable for use in correlative imaging using the ClairScope.

This suggests that the identically processed samples imaged on the ClairScope and in Quantomix capsules imaged on the FEGSEM may have contained photoconverted FM 5-95, although as the number of labelled vesicles was low, the magnitude of backscattered electrons was not great enough to allow visualisation through atmospheric scanning electron microscopy, as the hydrated environment scatters the electrons, in turn reducing contrast. An extra point for consideration is the fact that the recycled vesicles may be centrally located within the varicosity, therefore, if the material is too far from the point of initial penetration of the cell the more the electron beam will be scattered on return in the atmospheric, hydrated environment.

To overcome the caveats of imaging actively recycled vesicles by detection of photoconverted FM 5-95 using the ClairScope the recycling population was labelled by stimulated internalisation of anti-GFP primary antibody. As Chavis et al. (1998), successfully demonstrated, the rate of spontaneous vesicle exocytosis in comparison to vesicle dynamics under chemical stimulation could be measured. It was observed that the anti-GFP primary antibody was endocytosed specifically by B104 neuroblastoma cells transfected with spH (Figure 4.3.6.1a). This specificity was confirmed by control tests where primary anti-FLAG was used in place of anti-GFP antibody; here, no internalisation was observed. Analysis revealed that although internalisation is specific for GFP, it is not specific for only vesicular bound spH as a proportion of labelling remained membrane bound. The presence of spH in the cell membrane suggests that there may be leaky expression of spH by the B104 neuroblastoma cells. In this investigation inducer concentration was based on previous studies such as Burrone et al. (2007) which was shown to give reproducible results. In further studies this may be re- established to reduce the level of surface or leaky expression.

The internalisation of primary anti-GFP antibody under stimulation can only be presumed to have occurred, as the amount of surface staining, as suggested from the colocalisation studies in non-permeabilised cells, gave a predominant staining pattern that made positive identification of labelled internalised vesicles difficult. FM 5-95 results showed that that the stimulation technique works, and so as long as the antibody was bound to the spH, then the antibody should have been internalised upon stimulation.

In Chapter 3, it was proven that spH could be labelled with the same primary and secondary antibody using 20 nm gold particles, and so steric hindrance should be ruled out. However, in Chapter 3, spH was labelled post-permeabilisation with the primary antibody. There remains a possibility that the primary antibody labelling upon stimulation has prevented much of the spH from being internalised and thus remains on the cell surface which is in contrast to the staining pattern seen in Chapter 3 in fixed and permeabilised cells. In Chapter 3, non-permeabilised cells did not stain for spH, suggesting that in that case, most of the stained spH was contained within vesicles themselves and not as leaky (membrane) expression as the results here suggest. There remains a possibility that the immunolabelled spH on the cell surface is sterically hindered from binding 20nm tagged antibodies. Although Alexa 594 labelled antibodies can bind these surface proteins, they are significantly smaller than those that are tagged with 20 nm gold particles. To rule out steric effects, other fluorescent antibody probes could be used that are similar in size to the gold particles, for example QDots. However, in light of the difficulties in achieving high resolution images with minimal contrast, other approaches were developed to study protein localisation with improved accuracy.

## 5.0 Compartmentalisation of cAMP signalling in the neuronal differentiation of neuroblastoma cells.

### 5.1 Introduction

Neuroblastoma is predominately a childhood developmental neuroendocrine cancer that most frequently originates in the adrenal glands, although it may develop in nerve tissues in the neck, abdomen, chest and/ or pelvis (Papaioannou & McHugh 2005). In a number of cases spontaneous regression is observed and as a result, treatment of neuroblastoma sometimes includes the chemical differentiation of cancerous cells by retinoic acid to a benign neuronal cell fate, reviewed in (Papaioannou & McHugh 2005). Differentiation of neuroblastoma has been studied to identify mechanisms that could form a basis for the targeted treatment of the disease through stimulated differentiation. Differentiation of neuroblastoma cells in culture has been successfully achieved through the addition of retinoic acid to promote inhibition of carcinoma cell proliferation (Sidell 1982). The intracellular secondary messenger, 3’-5’-cyclic adenosine monophosphate (cAMP), has also been shown to promote the outgrowth of neurites and synaptogenesis, differentiating a variety of cell lines into neuronal-like cells. This has led to research focussing on the formation of neurites (neuritogenesis) axons, dendrites and synapse formation and organisations (Sutherland, 1970).

#### The cAMP signalling pathway

Differentiation of cells by cAMP occurs through the phosphorylation of effector proteins controlled by opposing actions of protein kinases and phosphatases (Krebs et al. 1959). Protein kinase A (PKA) (also known as cAMP-dependent protein kinase) is an enzyme complex that has long been considered a major player in cAMP dependent neuronal differentiation. The PKA holoenzyme is a heterotetramer that comprises two catalytic subunit domains, held in an inactive state by a regulatory dimer subunit (R-subunits) (Corbin & Keely 1977). There are two classes of PKA holoenzyme, Type I and Type II. Type I is mainly located throughout the cytoplasm, whilst PKA Type II is usually located and anchored to subcellular structures through tissue specific A-Kinase anchoring proteins (Dao et al. 2006). The two classes of PKA are identified by their different regulatory subunits, RI and RII, which may be further classified into subtypes RIα, RIβ, RIIα and RIIβ, defined not only by cellular localisation, but by their individual affinity for cAMP (Dao et al. 2006).

Ligand binding to G-protein coupled receptors (GPCRs) and activation of adenylyl cyclase (AC) via G proteins leads to increased levels of cAMP (Taskén & Aandahl 2004). As cytosolic cAMP concentrations increase, two molecules of cAMP bind to each cAMP binding domains of the regulatory subunit, resulting in a conformational change and releasing the subunits from the active domains of the catalytic subunits as the complex dissociates (Kopperud et al. 2002; Taskén & Aandahl 2004). This process leads to activation of the catalytic subunits through interaction with surrounding proteins resulting in the phosphorylation of serine and threonine residues. The usual target sequence for phosphorylation is Arg-Arg-X-Ser/Thr-X, where X is a hydrophobic amino acid (Tojima et al. 2003). It has been suggested that an increase in intracellular cAMP levels is able to activate two kinase pathways via PKA and mitogen activated protein kinase (MEK). The activation of MEK mediates neuritogenesis and the activation of the PKA pathway stimulates both neuritogensis and synaptogenesis (Figure 5.1.1) (Tojima et al. 2003).

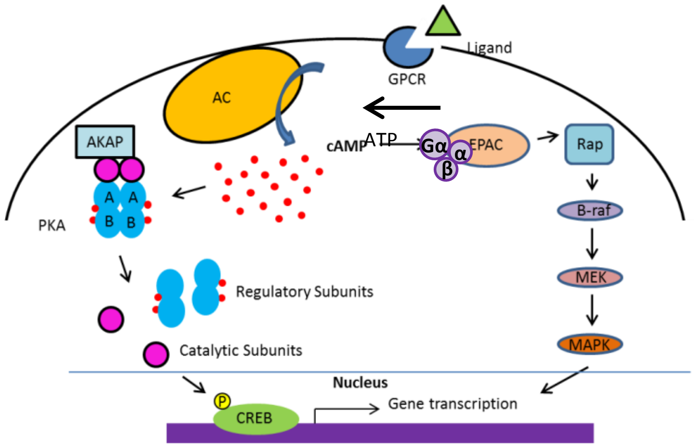

**igure 5.1.1. cAMP signalling pathway.** Through ligand stimulation of G-protein coupled receptors (GPCR), adenylyl cyclase (AC) is activated generating cAMP. Two molecules of cAMP bind each regulatory subunit of PKA. Dissociation of the PKA complex occurs, releasing the catalytic subunits, which regulate transcription factors in the nucleus. cAMP activates the MAPK pathway by activating EPAC. (Figure hand drawn)

### Spatial and temporal organisation and anchoring of PKA

A-kinase anchoring proteins (AKAPs) are a structurally diverse family of proteins with the ability to bind PKA, providing spatial and temporal regulation of PKA signalling by anchoring PKA to specific subcellular domains, structures and membranes (Figure 5.1.2) (Skalhegg & Tasken 2000; Dell'Acqua et al. 2006). AKAPs bind the regulatory subunits of PKA via the stretch of 14 – 18 amino acids forming an amphipathic helix, which binds to the hydrophobic groove formed by the dimerization domain of the PKA regulatory subunits (Dell'Acqua et al. 2006).

The majority of AKAPs bind only RI type subunits or only RII type subunits; only six AKAPs are able to bind both types of R subunits, so-called dual AKAPs; D-AKAP1, D-AKAP2, AKAP 220, Ezrin, Merlin and PAP7 (Jarnaess et al. 2008). AKAPs play a vital role by anchoring PKA to specific cellular locations and targeting it to signalling partners in various cellular functions (Coghlan et al. 1995; Scott et al. 2013), including neuronal plasticity and neurite outgrowth (Bauman et al. 2004). Investigations into AKAP binding specificity have led to the development of inhibitory peptides such as inhibitory peptide I (IP-I); a peptide specifically designed to bind RIα by mimicking the amphipathic AKAP binding helix. PKA localisation is disrupted on binding IP-I; this is similar to the inhibitory peptide Ht31, which has been used successfully in PKA studies, although Ht31 is not RIα specific as it also interacts with RIIα (Burns-Hamuro et al. 2003).

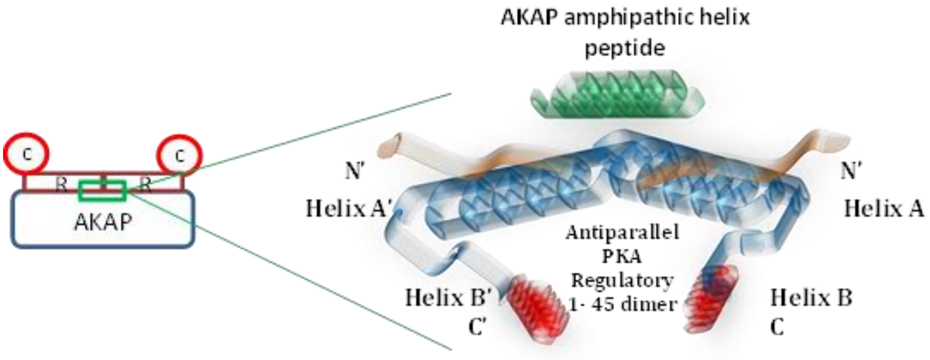

**Figure 5.1.2. PKA binding to AKAP.** The regulatory subunits of the PKA complex bind to the specific amphipathic helix peptide in the binding domain of AKAPs. AKAPs anchor PKA to subcellular targeting domains. (Figure hand drawn, based on Taskén & Aandahl (2004)).

## Imaging proteins involved in differentiation

Extensive research into PKA has focussed on the localisation of the two forms of PKA, Types I and II. Using antibodies specific for PKA I and PKA II, immunofluorescence enabled the visualisation of regulatory subunit localisation. For instance, in developing neurons it was observed that PKA type I was dispersed evenly throughout the cell, although PKA type II was localised only at the periphery of the growth cone (Han et al. 2007). Research has also shown that pools of cAMP are specifically generated in response to the availability of ligand and receptors. It has therefore been suggested that the cAMP gradient may follow the distinct route of PKA signalling or the localisation of PKA-AKAP complex formation (Skalhegg & Tasken 2000).

Live cell fluorescence imaging has been instrumental in the study of cAMP concentration, as in a study by Zaccolo and Pozzan (2002) the application of fluorescence resonance energy transfer (FRET) to follow PKA subunit dissociation in the presence of cAMP. This allowed the visualisation of microdomains of high concentrations of cAMP, indicating the specific localisation of cAMP within the cell. This technique was used to investigate the role of PKA and cAMP compartmentalisation in the regulation of Cl- efflux in cells with a cystic fibrosis transmembrane conductance regulator mutation. This resulted in excessive cytosolic accumulation of cAMP and increased PKA activity, allowing investigation into a mechanism to restore normal cellular organisation and compartmentalisation of cAMP and PKA (Monterisi et al. 2012).

Studies have been conducted into the localisation of the PKA subunit RIIα, such as those by Lester et al, which showed co-localisation of RIα puncta with testicular peroxisomes. It was also established in this study that the localisation is through interaction with AKAP 220, which possesses both a PKA binding region and a peroxisome targeting motif (Lester et al. 1996). Further to these studies, RIα puncta in a variety of cell lines were studied by Day et al. (2011), where the RIα subunits were shown to be incorporated in multivesicular bodies (MVBs). MVBs are unique organelles that form via the endosomal pathway, containing multiple vesicles within their lumen. This was demonstrated via correlative fluorescence and electron microscopy, as correlation between GFP fluorescence from GFP-RIα and electron dense areas within MVBs imaged by TEM (Figure 5.1.3).

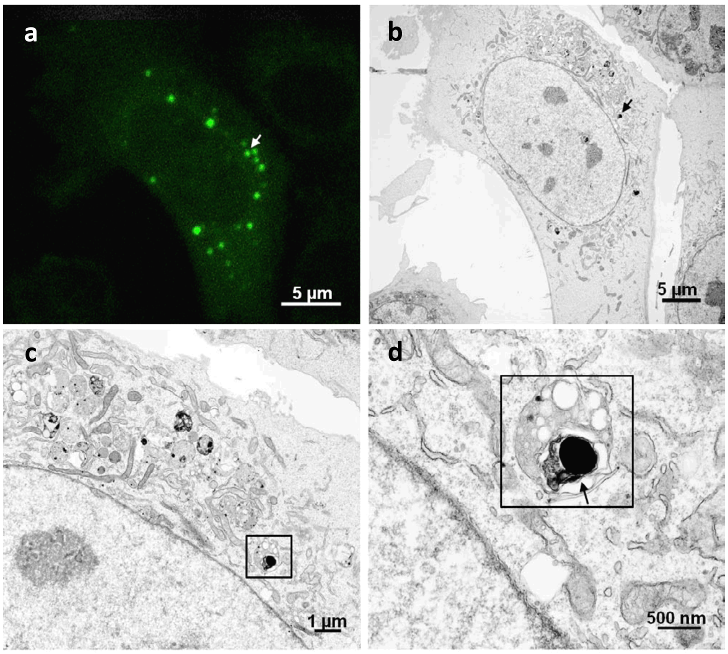

**Figure 5.1.3. RIα-GFP fluorescence correlated with TEM** a) GFP RIα fluorescence in MEF cells. b) Electron micrograph of the same cell in a) the black arrow highlights an electron dense area correlating to the GFP fluorescence in a). c) and d) higher magnification EM images of the electron dense area in b) displaying multivesicular membranes within one outer membrane. Image reproduced from Day et al. (2011). Disclaimer: Third parties may use our (Journal of Cell Biology) published materials under a Creative Common Attribution-Non commercial-Share Alike 3.0 Unported License six months after publication. (Full attribution given in bibliography)).

The electron micrograph in Figure 5.1.3 taken from Day et al (2011) highlights the colocalisation of RIα fluorescence with an electron dense area within a multivesicular formation. It is observed that only the indicated area co-localises with one electron dense area; many other clusters are fluorescent but do not correlate with electron dense areas in the EM image. It should also be noted that the sample has undergone no processing in order to transform or label the GFP fluorescence with an electron dense marker for detection by EM, although it is stated that the GFP produces electron dense puncta in correlation with those seen by fluorescence. Therefore this experiment does not, beyond doubt, identify the fluorescence in live cells as the electron dense puncta observed by EM, and hence, as no other electron dense material correlates with RIα fluorescence, the containment of RIα subunits within MVBs is equivocal.

This experimental system could be better studied using a more direct CLEM method such as is offered by the ClairScope.

## 5.2 Aims and objectives of the research described in Chapter 5.

**Aim:** The overall goal of the research presented in this chapter is to relate the intracellular localisation of RIα to function; with the aim to reproduce research presented by Day et al (2011). Investigations into RIα-AKAP localisation to MVBs were reproduced, following on to investigations into why these proteins might be found in association with the lumen of MVBs.

**Objectives:**

1) Visualise RIα puncta by immunogold labelling on the ClairScope.
2) Characterise the effect of cAMP on puncta formation.
3) Determine any co-localisation of RIα puncta with other cellular organelles.
4) Investigate the dynamics of CFP RIα puncta in live cells by FRAP and FLIP.

## 5.3 Results

### 5.3.1. RIα puncta in differentiated B104 neuroblastoma cells.

Initial studies were conducted into the formation of RIα containing puncta by incubation with membrane permeable dibutyryl cAMP (referred from here onwards as dib-cAMP) in B104 neuroblastoma cells and U251 glioblastoma cells. Fluorescence images of B104 neuroblastoma cells transfected with RIα-FLAG and labelled with mouse anti-FLAG antibody and anti-mouse Alexa 594 secondary antibody and DAPI were acquired by confocal microscopy. Cells were differentiated by incubation with 1 mM dib-cAMP over 4 days. In each case samples were fixed and permeabilised prior to labelling (Figure 5.3.1.1).

Insoluble puncta were seen to form in the differentiated B104 neuroblastoma cells, transfected with RIα-FLAG tagged protein by fluorescence microscopy. This was reconfirmed in a separate U251 glioblastoma cell line, (Figure 5.3.1.1). In non-differentiated samples RIα was dispersed throughout the cell. This confirmed the observations by fluorescence microscopy by Day et al. (2011).

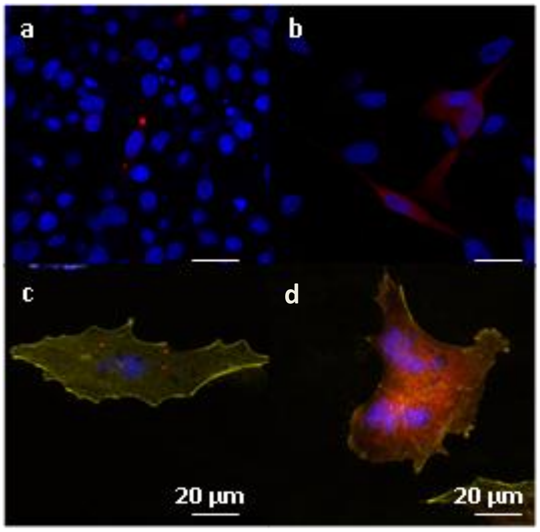

**Figure 5.3.1.1. Protein puncta in differentiated B104 neuroblastoma cells and U251 glioblastoma cells transfected with RIα-FLAG.** Fluorescence images of B104 neuroblastoma cells (a) and U251 glioblastoma cells (c) labelled with primary antibody mouse anti-FLAG and anti-mouse Alexa 594 secondary antibody and DAPI. Fluorescence of differentiated B104 neuroblastoma cells (b) and U251 glioblastoma cells (d) by incubation with 1 mM dib-cAMP over 4 days, labelled with primary antibody mouse anti-FLAG and anti-mouse Alexa 594 secondary antibody and DAPI.

To investigate the validity of the CLEM studies by Day et al. (2011) (Figure 5.1.3) RIα puncta were processed and imaged using the ClairScope, as previously described in this project. Fluorescently labelled RIα-CFP (cyan fluorescent protein) was overexpressed in differentiated B104 cells. This approach was initially tested for specificity; samples were labelled with primary mouse anti-GFP antibody (serum) and an anti-mouse Alexa 488 secondary fluorophore, as shown in Figure 5.3.1.1. For imaging by CLEM, RIα-CFP puncta were labelled with mouse anti-GFP primary antibody followed by specific immunogold labelling of the CFP protein with 20 nm immunogold particles. It was observed by imaging 5 samples displaying fluorescent RIα-CFP puncta using the ClairScope, that immunogold labelling of RIα-CFP puncta was not visible Figure 5.3.1.2. It is possible that the RIα-CFP might be located in the centre of the hydrated structure and therefore no signal is detected due to a high degree of scatter of both the electron beam and backscattered electrons. In order to continue investigations into the localisation of RIα-CFP, fluorescence microscopy techniques were used in place of CLEM. The position of RIα-CFP puncta was determined through the acquisition of z-stacks and comparison with the distance of the puncta from the glass cover slip (Figure 5.3.1.2g). The mean distance within the cell was calculated as ~3µm, which may explain the lack of contrast in ASEM images of RIα-CFP puncta. It would be difficult to determine the distance between the puncta and the silicon nitride membrane in the ASEM dishes, due to the need to use a water dipping lens. This has much poorer depth discrimination compared to the 63x oil immersion objectives used with coverslips.

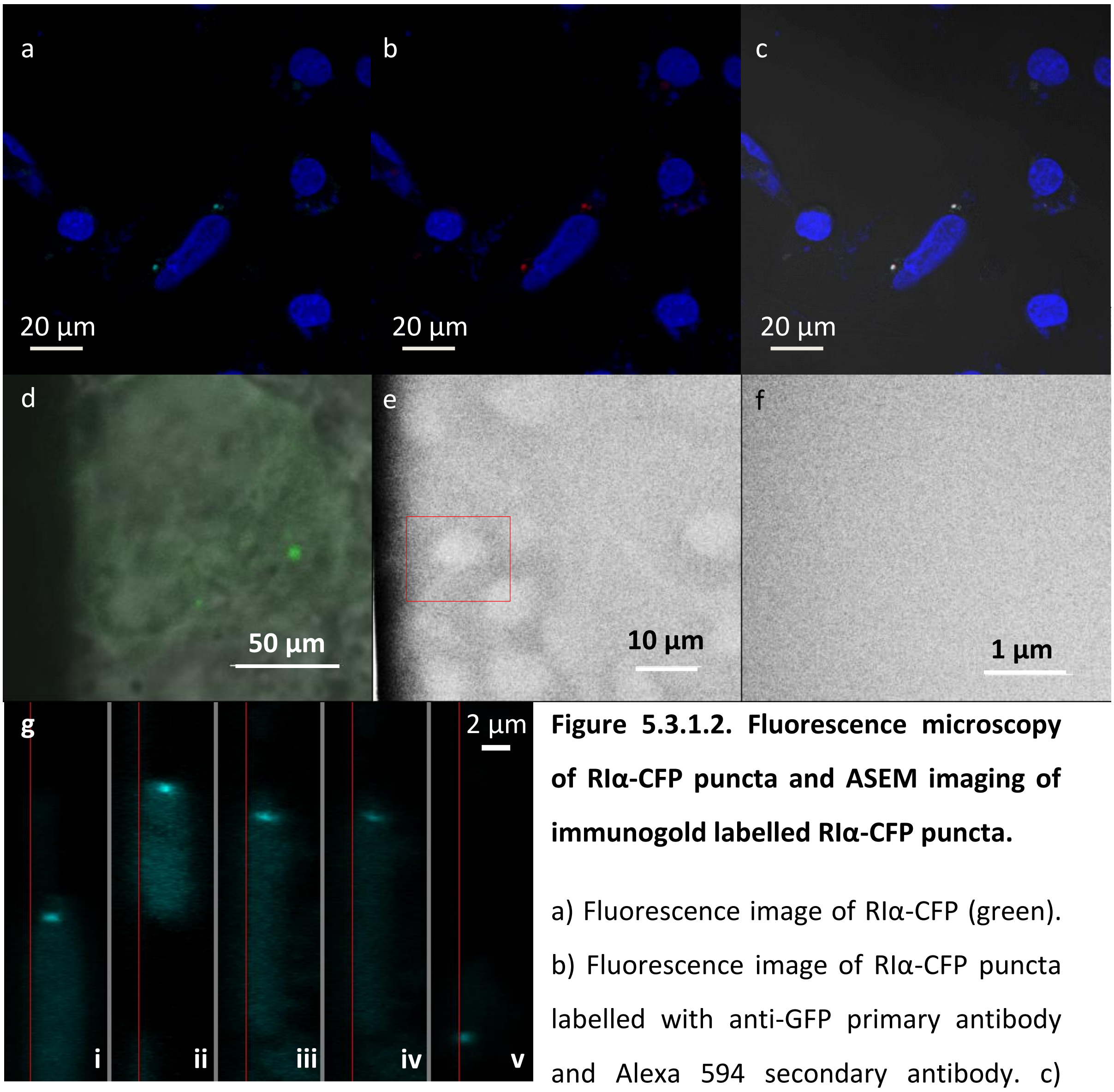

**Figure 5.3.1.2. Fluorescence microscopy of RIα-CFP puncta and ASEM imaging of immunogold labelled RIα-CFP puncta.**

a) Fluorescence image of RIα-CFP (green). b) Fluorescence image of RIα-CFP puncta labelled with anti-GFP primary antibody and Alexa 594 secondary antibody. c) Fluorescence overlay of images in a) and b). d) Confocal fluorescence image of RIα-CFP puncta (green), overlaid on transmitted light image. e) ASEM image at 4,000x magnification, highlighted area is the cell in d). f) ASEM image of highlighted area in b) imaged at 20,000x magnification. g) i-v) side view of RIα-CFP puncta z-stacks on glass coverslips. Red lines indicate the position of the glass surface compared to the puncta.

### 5.3.2. Identification of RIα-CFP and RIα-FLAG colocalisation.

In initial experiments where RIα-FLAG was used as a marker, labelling of the FLAG-tag peptide and any other target proteins was not possible due to un-availability of suitable antibodies. Therefore RIα-CFP was used in further experiments to provide a fluorescent marker of RIα without the requirement for extra labelling; this aspect is important for imaging by ASEM on the ClairScope, since labelling with electron dense material can be achieved by immunogold labelling of fluorescent proteins. To confirm that RIα-CFP may be used in place of RIα-FLAG, a time course experiment was carried out. B104 neuroblastoma cells were transfected with RIα-CFP and RIα-FLAG for 18 hours and incubated with dib-cAMP over 4 days, with samples fixed at several time points throughout the experiment. The samples were imaged by detecting the CFP fluorescence and immunolabelling of RIα-FLAG with anti-FLAG primary antibody and Alexa 594 secondary fluorophore (Figure 5.3.2.1a- f); the mean number of puncta per cell was quantified, as shown in (Figure 5.3.2.1g). The extent of colocalisation between RIα-CFP puncta and FLAG RIα puncta was also quantified (Figure 5.3.2.1h).

Quantification of puncta was achieved through manually counting the number of puncta in at least 90 cells in each data set in 3 biological replicates; RIα-CFP and RIα-FLAG puncta showed progressive development and colocalisation of puncta over time. It was observed that RIα-FLAG puncta develop at a faster rate with a mean number of puncta per cell of 2.8. RIα-FLAG puncta had formed after 1 hour and 3.7 at 96 hours of incubation with dib-cAMP, whereas a mean number of 1.0 RIα-CFP puncta per cell had formed at 1 hour and a mean of 2.7 puncta per cell after 96 hours incubation with dib-cAMP. The rate of development increased at a similar rate in each case, with colocalisation of the mean number of puncta per cell increasing over time from 21 ± 0.42 % at 18 hours to 33 ±0.8 % at 24 hours and 46 ±0.53 % colocalisation at 96 hours. This suggests that the two tagged forms of RIα protein form puncta by the same cellular pathway following incubation with dib-cAMP, although the temporal difference is still not clear. Therefore, to enable labelling of proteins which may co-localise with RIα; RIα-CFP was used in all further experiments.

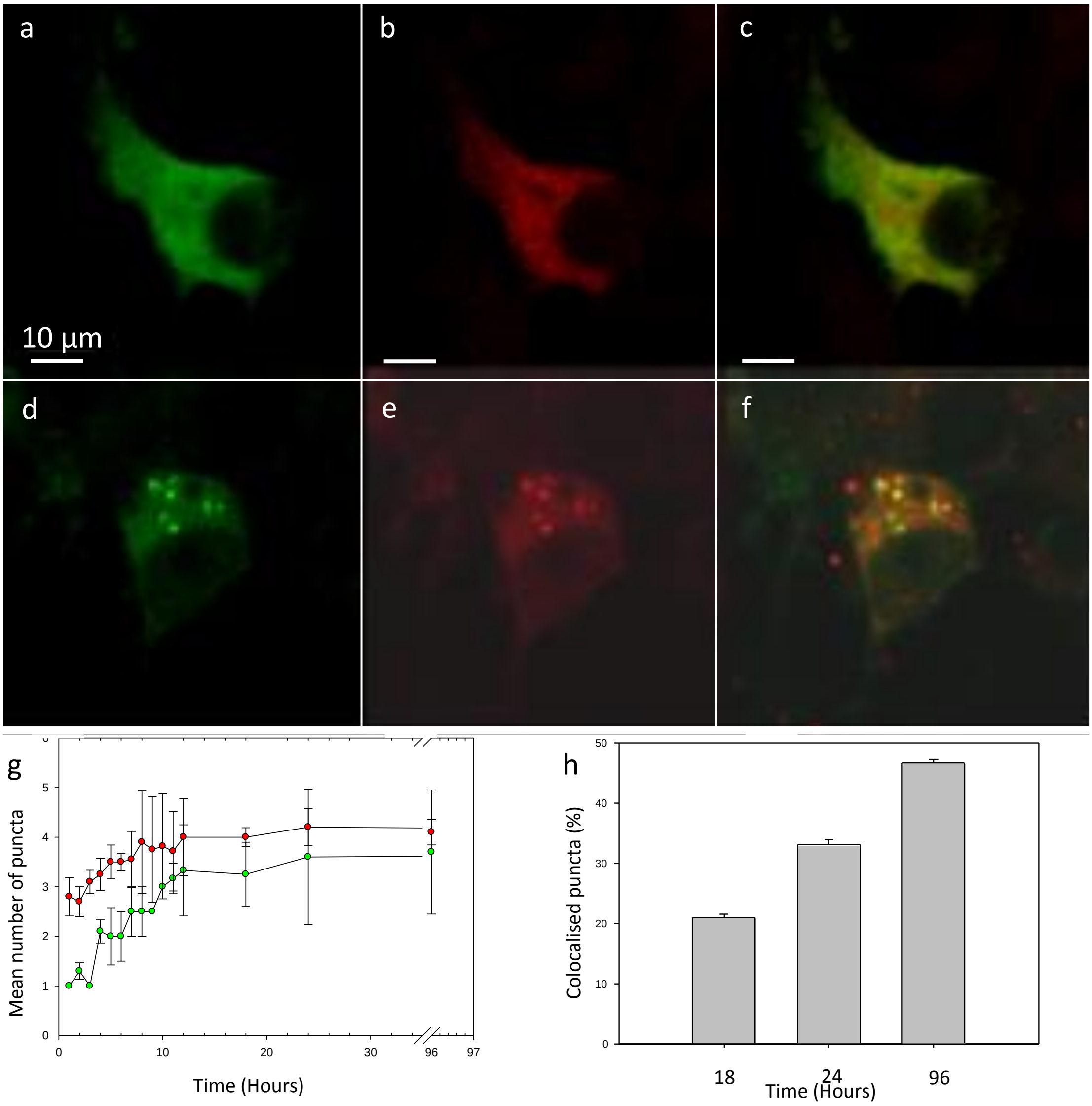

**Figure 5.3.2.1. RIα-CFP and RIα-FLAG puncta formation in B104 neuroblastoma cells over time and percentage puncta colocalisation.** a) Fluorescence image of RIα-CFP in B104 neuroblastoma cells imaged after 0 hours incubation with dib-cAMP. b) Fluorescence image of RIα-FLAG in the same cell as in (a) labelled with Alexa 594. c) Overlay of fluorescence RIα-CFP and RIα-FLAG fluorescence images a) and b). d) Fluorescence image of RIα-CFP in B104 cells imaged after 96 hours incubation with dib-cAMP. e) Fluorescence image of RIα-FLAG in the same cell as in (d) labelled with Alexa 594. f) Overlay of RIα-CFP and RIα-FLAG fluorescence images c) and d). g) Scatter plot showing mean number of RIα-CFP (green) and RIα-FLAG puncta (red) over 96 hours. h) Histogram displaying percentage colocalisation of RIα-CFP and RIα-FLAG puncta over time. Error bars show the s.e.m. for 90 measurements made on 3 separate biological replicates.

### 5.3.3. Dib-cAMP dependent RIα-CFP puncta dynamics

It has been previously shown by Day et al. (2011) that of the six AKAPs with dual binding specificity only AKAP 220 co-localises with RIα dib-cAMP-dependent puncta. This was shown to occur in the cell cytosol following incubation with dib-cAMP. To investigate the dynamics and association with cellular differentiation, experiments were carried out to establish what effect the removal of dib-cAMP from culture media had on the formation of RIα-CFP and AKAP 220 puncta. This would also determine if the puncta are dib-cAMP dependent.

Initial investigations studied the effect of dib-cAMP removal after incubation for four days on the formation of RIα-CFP puncta and AKAP 220 puncta. B104 neuroblastoma cells were transfected with RIα-CFP for 18 hours and then incubated for four days in the presence of 1mM dib-cAMP. A second set of non-transfected samples were cultured for 4 days in the presence of dib-cAMP. After four days the culture media was removed from each set and replaced with fresh DMEM containing no dib-cAMP and the samples cultured for a further 4 days. Following immune-labelling and imaging by confocal microscopy the number of puncta present in each sample set was analysed (Figure 5.3.3.1).

The removal of dib-cAMP from the culture media and incubation for a further 4 days in fresh media resulted in the disappearance of RIα-CFP puncta. A decrease in mean number of AKAP 220 puncta was also observed; suggesting that in both cases the puncta are dynamic and develop in a dib-cAMP-dependent manner.

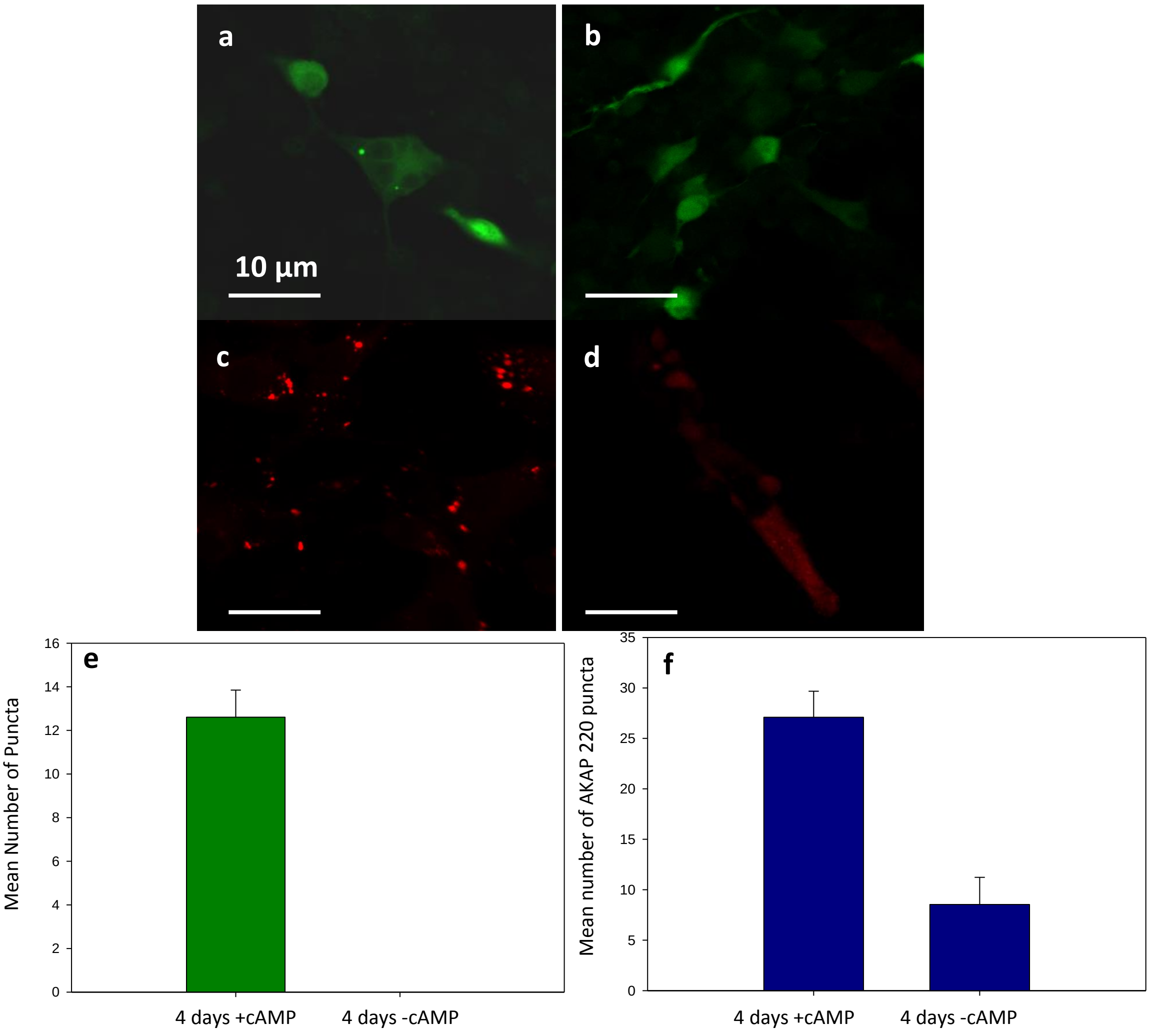

**Figure 5.3.3.1. RIα puncta formation in B104 neuroblastoma cells in the presence and absence of dib-cAMP.** a) Fluorescence image of RIα-CFP in B104 cells imaged after 4 days incubation with dib-cAMP. b) Fluorescence image of RIα-CFP in B104 cells imaged after 4 days incubation with dib-cAMP and 4 days in dib-cAMP free media. c) Fluorescence image of AKAP 220 in B104 cells imaged after 4 days incubation with dib-cAMP labelled with Alexa 594. d) Fluorescence image of AKAP 220 in B104 cells imaged after 4 days incubation with dib-cAMP and 4 days in dib-cAMP free media labelled with Alexa 594. e) Histogram displaying mean number of RIα-CFP puncta per cell at 4 days dib-cAMP incubation and 4 days dib-cAMP incubation followed by 4 days in dib-cAMP free media. f) Histogram displaying mean number of AKAP 220 puncta per cell at 4 days dib-cAMP incubation and 4 days dib-cAMP incubation followed by 4 days in dib-cAMP free media. Error bars show the s.e.m. for 90 measurements made on 3 separate biological replicates.

### 5.3.4. FRAP and FLIP of RIα-CFP puncta in live cells

Having shown that the RIα-CFP puncta are reversible following removal of dib-cAMP at 4 days, the study of the fast dynamics of RIα-CFP turnover by FRAP was performed. This enabled investigation into whether RIα-CFP puncta were in association with MVBs or localised elsewhere as suggested by Day et al. (2011).

Measurements were made on B104 neuroblastoma cells cultured in 8 chambered coverslips (LabTek) transfected with RIα-CFP for 18 h and differentiated by incubation with 1 mM dib-cAMP for 4 days.

On day 4 the cells were transferred to a stage incubator set up on an inverted confocal microscope. This stage incubator allowed live cell imaging to take place whilst maintaining the cells in media at 37°C in a humid atmosphere with 5 % $CO_2$. FRAP of the RIα-CFP puncta was then carried out, first establishing the baseline fluorescence over 20 scans, before bleaching the RIα-CFP puncta with a 405 nm laser at 50 % power with 25 iterations per bleach. The fluorescence intensity of the RIα-CFP puncta was traced (Figure 5.3.4.1a –e). Percentage recovery of the RIα-CFP cluster following bleaching of the punctum was 91.9 %, suggesting that the RIα-CFP molecules are able to exchange between the cytoplasmic regions and the puncta; therefore it is unlikely to be compartmentalised within a structure such as MVBs.

Fluorescence loss after photobleaching was used to further measure the fluorescence exchange dynamics of the RIα-CFP puncta. Following repeated bleaching of the cytoplasmic RIα-CFP fluorescence, it was observed that the fluorescence intensity of the puncta decreases (Figure 5.3.4.2a -e). These data demonstrate that RIα-CFP is able to exchange freely between the puncta and the soluble cytoplasmic pool, suggesting it is not compartmentalised within vesicular structures such as MVBs.

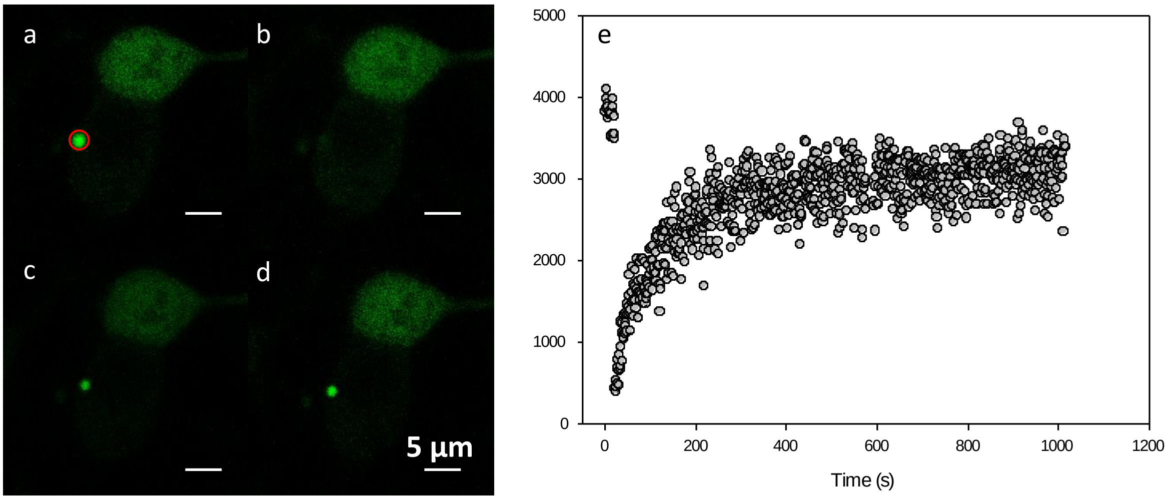

**Figure 5.3.4.1 Representative fluorescence recovery after photobleaching of RIα-CFP puncta.** a) Cell with RIα-CFP puncta pre bleaching; Red highlighted area indicates bleached area. b) post bleach, c) mid recovery d) recovery of CFP fluorescence. e) Scatter plot of fluorescence intensity of puncta shown in a). Red line denotes a best fit double exponential recovery of fluorescence (Methods and Materials section 2.4.3). $t_{1/2}$ of puncta recovery was 70 ± 7 s (n = 10) with a percentage recovery of 70 % (Methods and Materials section 2.4.3). All experiments conducted at 37°C, at a $CO_2$ humidity of 5 %.

Previous investigations of the behaviour of freely diffusing proteins in live cells by FRAP have shown varying rates of recovery. GFP (p53- GFP) in the nucleus was shown to have a t1/2 of ~2s, whereas in the same study GFP in the cytoplasm was shown to have a t1/2 of ~0.16s (Drake et al. 2010). A separate study showed that GFP localised in the plasma membrane had a t1/2 of ~20s (Kenworthy et al. 2004). These recovery times depend on simple diffusion and transient binding. Extracting meaningful numbers from recovery curves is highly complex, especially in 3D systems, where the bleach volume is poorly defined, as in the research discussed in this thesis. Therefore the t1/2 appears slow compared to those seen in previous research as recovery depends on binding rates as well as diffusion, although these results do prove that the RIα protein is in dynamic equilibrium.

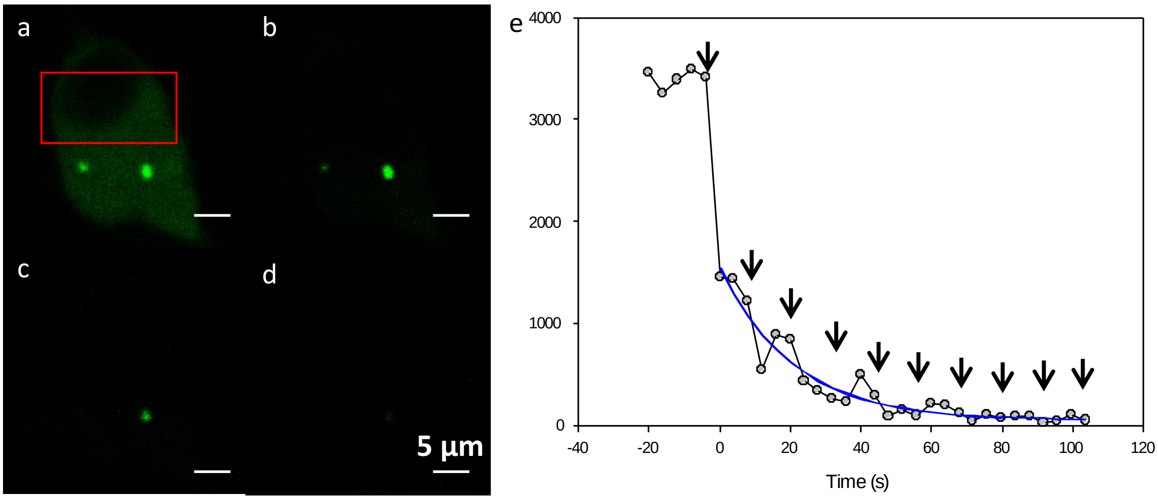

**Figure 5.3.4.2 Representative fluorescence loss after photobleaching of RIα-CFP puncta.** a) Cell with RIα-CFP puncta pre bleaching. Red highlighted area indicates bleached area; b) post single bleach, c) post 3 bleaches d) post 6 bleaches. e) Scatter plot of fluorescence intensity of RIα-CFP puncta through repeated bleaching of the cytoplasm shown in a). Arrows show timing of each bleach pulse. Number of biological replicates = 10.. Blue line denotes exponential decay fit to the data after the first bleach period.

### 5.3.5. Colocalisation of RIα with MVB and ESCRT proteins.

Despite some quite rigorous co-localisation studies with markers of the endocytic and endosomal trafficking pathways, Day et al. (2011) did not examine whether RIα puncta co-localise with MVB specific markers, like the endosomal sorting complex required for transport (ESCRT). To address this, an antibody raised against the ESCRT scaffold associated protein ALIX (apoptosis linked gene 2-interacting proteins X; also known as programmed cell death 6 interacting protein (PDCD6IP)) was used (Katoh et al. 2003; Mahul-Mellier et al. 2006). B104 neuroblastoma cells were transfected with RIα-CFP for 18 hours and differentiated for 4 days by incubation with 1 mM dib-cAMP. Samples were then fixed, permeabilised with 1 % (v/v) Triton X -100 and labelled with anti-ALIX primary antibody and Alexa 594 secondary antibody. Following imaging by confocal microscopy the mean number of RIα puncta, and ALIX labelled puncta per cell were quantified, and the number of co-localising puncta was calculated (Figure 5.3.5.1).

Analysis of the puncta showed no significant colocalisation for ALIX and RIα-CFP. The mean number of RIα-CFP puncta was 2.3 ± 1.4 per cell, in comparison to a higher mean number of ALIX puncta per cell which was 4.4 ±1.5. Colocalisation was only observed in one sample, resulting in an average number of co-localised of 0.05 ±0.08 per cell. The results shown here, that RIα-CFP and ALIX do not co-localise in differentiated B104 neuroblastoma cells, is not conclusive evidence against MVB localisation. No clear conclusion can be made about the association of RIα with MVBs, as hypothesised by Day et al. (2011), or that association occurred with a separate marker involved in the late endosomal pathway, e.g. Rab7 (Bucci et al. 2000) and Rab9 (Lombardi et al. 1993).

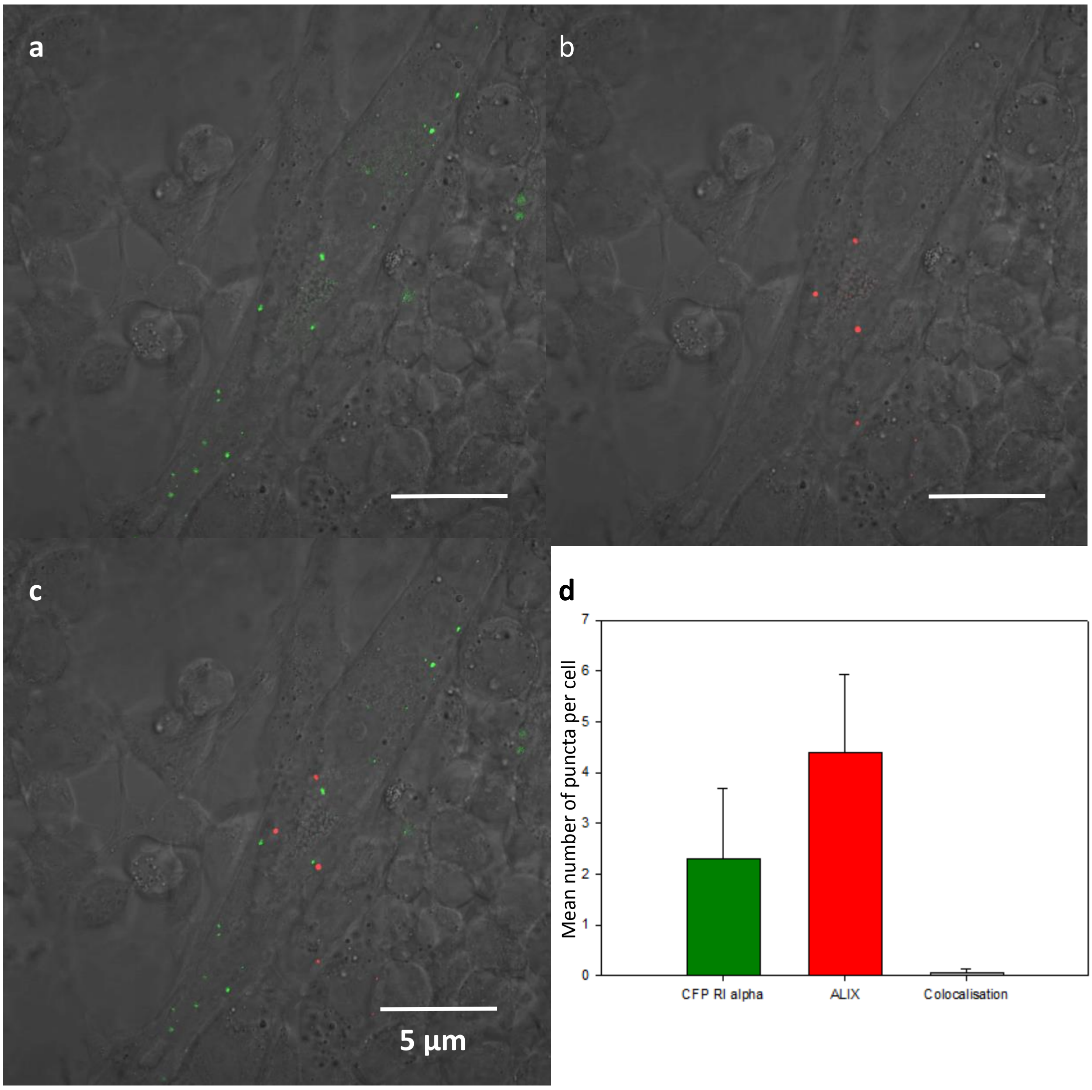

**Figure 5.3.5.1. RIα-CFP and ALIX puncta in B104 neuroblastoma cells.** a) Fluorescence image of RIα-CFP in a single B104 cell cultured for 4 days in the presence of dib-cAMP. b) Fluorescence image of ALIX puncta, in the same cell as in (a), labelled with Alexa 594. c) Overlay of RIα-CFP and ALIX fluorescence images. d) Histogram displaying mean number of RIα-CFP and ALIX puncta per cell and mean number of puncta colocalisation. Error bars show s.e.m. No significant difference was observed between mean numbers of CFP RIα and ALIX labelled puncta. n = 30 measurements made on one biological replicate.

Having demonstrated that RIα and AKAP 220 are unlikely to be localising to MVBs, a series of experiments were conducted to assess whether other punctate organelles co-localise with of RIα-AKAP220 puncta.

### RIα does not co-localise with mitochondria

Studies were carried out to investigate the colocalisation of RIα puncta with mitochondria. This was considered as a potential target for colocalisation due to studies into the interaction of PKA with localised pools of dib-cAMP. It has been shown that dib-cAMP dependent phosphorylation such as that induced by PKA activation occur in both the mitochondrial matrix and outer mitochondrial membrane (Lefkimmiatis et al. 2013). B104 neuroblastoma cells were co-transfected with RIα-CFP and Mito ds Red (gene product) for 18 hours and differentiated by incubation with dib-cAMP for 4 days. Cells were fixed and imaged by confocal microscopy (Figure 5.3.2.2a- c).

It was observed that no colocalisation occurred between RIα-CFP with the mitochondrial label Mito ds Red as shown in the cross section of fluorescence intensity (Figure 5.3.2.2d). A sharp increase in RIα-CFP fluorescence is seen representing the punctum, although in the red channel, representing the Mito ds Red, only on-cell base line fluorescence is observed at this point, suggesting no co-localisation of the fluorophores.

### RIα does not co-localise with lipid droplets

Having shown that RIα-CFP did not co-localise with mitochondria, a probe used to label lipid droplets, Oil red O (ORO), was used to test lipid droplets for co-localisation of RIα subunits (Pidoux et al. 2011). It has been observed that in adipocyte cells PKA surrounds lipid droplets (Brown 2001). It has been suggested that this may be in response to local availability of dib-cAMP due to PKA activated lipolysis and ATP generation.

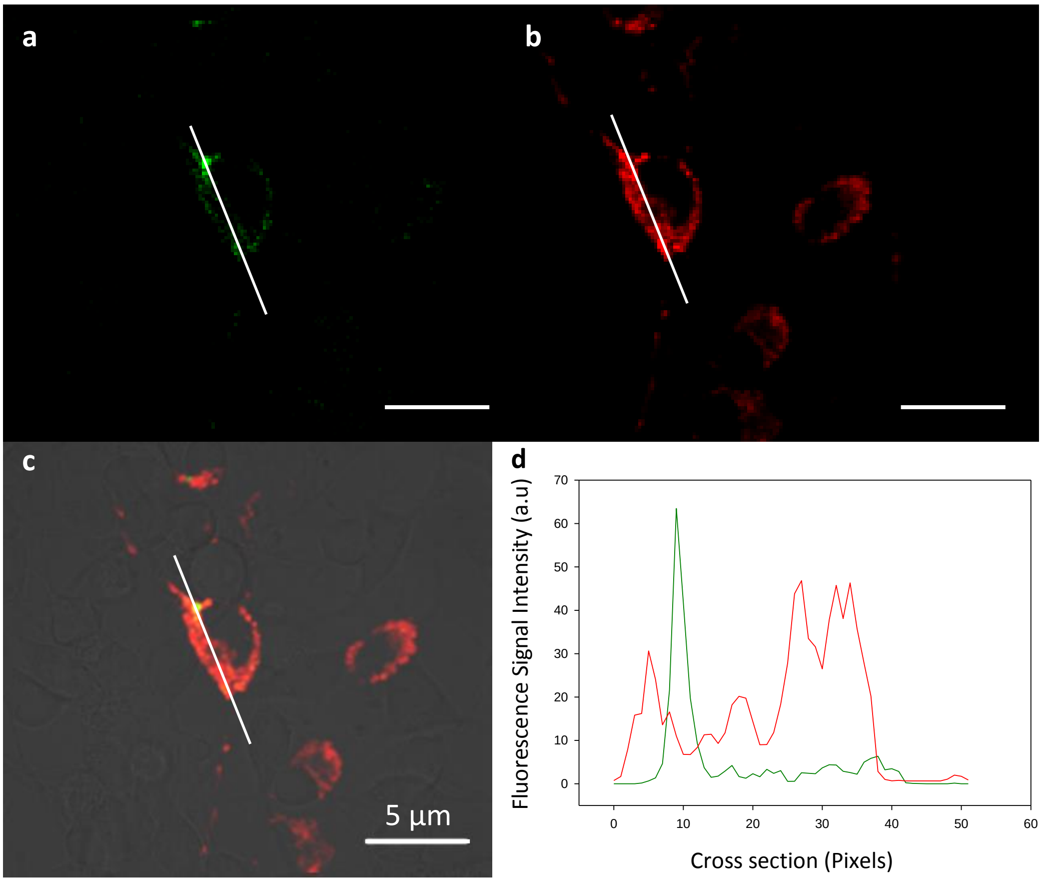

**Figure 5.3.5.2. RIα-CFP puncta fluorescence correlation with Mito ds Red.** a) Representative (n = 3) fluorescence image of RIα-CFP puncta with cross section measurement marked by white line. b) Fluorescence image of Mito ds Red puncta with cross section measurement marked by white line. c) Overlay of fluorescent images of RIα-CFP and Mito ds Red. d) Line graph of fluorescent intensity in both the Mito ds Red (red) and RIα-CFP (green) channels measured in the cross section marked in the images.

B104 neuroblastoma cells were transfected with RIα-CFP for 18 hours and cultured for 4 days in the presence of 1 mM dib-cAMP. Cells were fixed and permeabilised with 60 % (v/v) isopropanol and lipid droplets were labelled with ORO. Following visualisation by confocal microscopy the mean number of RIα puncta and lipid droplet puncta per cell were quantified, as shown in Figure 5.3.5.3.

It was observed that colocalisation assays between RIα-CFP and Oil Red O stained lipid droplets were inconclusive; Figure 5.3.5.3g, h, i. There was also no significant difference between mean number of ORO puncta under each condition. In cells transfected with CFP only the calculated mean number of ORO puncta per cell was 3.87 ±1.52 following incubation with dib-cAMP and 2.09 ±0.93 in the absence of dib-cAMP. Mean number of ORO puncta per cell was 4.11 ±0.94 following incubation with dib-cAMP and 4.42 ±1.20 in the absence of dib-cAMP. Mean number of RIα puncta per cell was 1.61 ±0.48 following incubation with dib-cAMP and 0 ±0 in the absence of dib-cAMP. Mean number of ORO puncta per cell transfected with CFP IP-I was 3.0 ±1.3 following incubation with dib-cAMP and 2.3 ±1.5 in the absence of dib-cAMP. It was observed that in the absence of dib-cAMP fewer ORO stained lipid droplets were present, except in cells transfected with RIα-CFP. Significance between each condition compared with the control was established using a one- way ANOVA test.

Although the RIα puncta have been shown not to co-localise with MVBs and show dynamic recovery by FRAP, further research into specific ultrastructural markers or proteins that possibly co-localise with RIα subunits is required. As co-localisation with lipid droplets using oil red O staining was inconclusive, labelling lipid droplets with antibody for perlipin (Brown 2001) in conjunction with RIα- CFP expression may reveal clearer results.

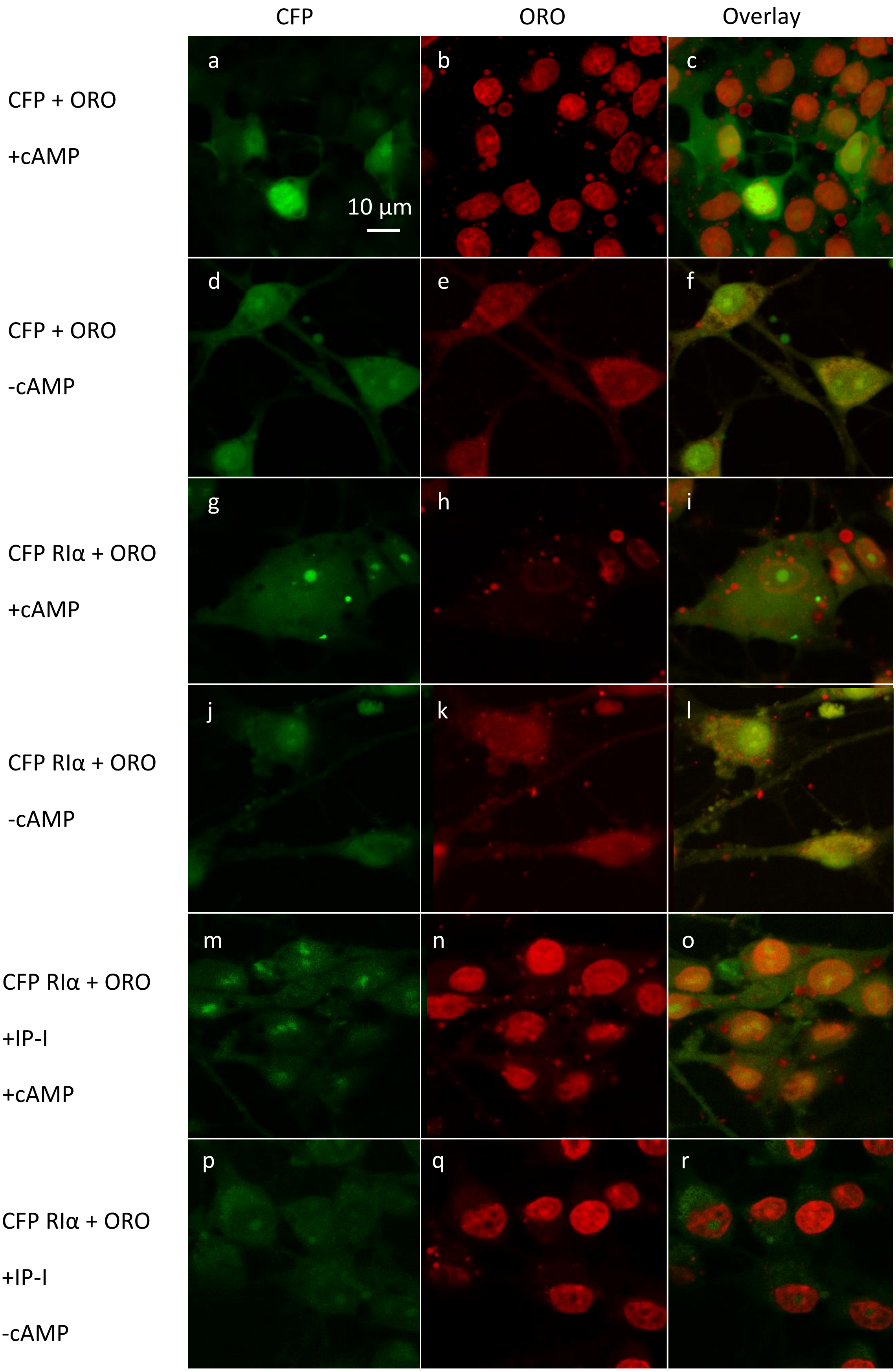
CFP
ORO
Overlay
CFP + ORO
+cAMP
a
b
c
10 µm
CFP + ORO
-cAMP
d
e
f
CFP RIα + ORO
+cAMP
g
h
i
CFP RIα + ORO
-cAMP
j
k
l
CFP RIα + ORO
+IP-I
+cAMP
m
n
o
CFP RIα + ORO
+IP-I
-cAMP
p
q
r

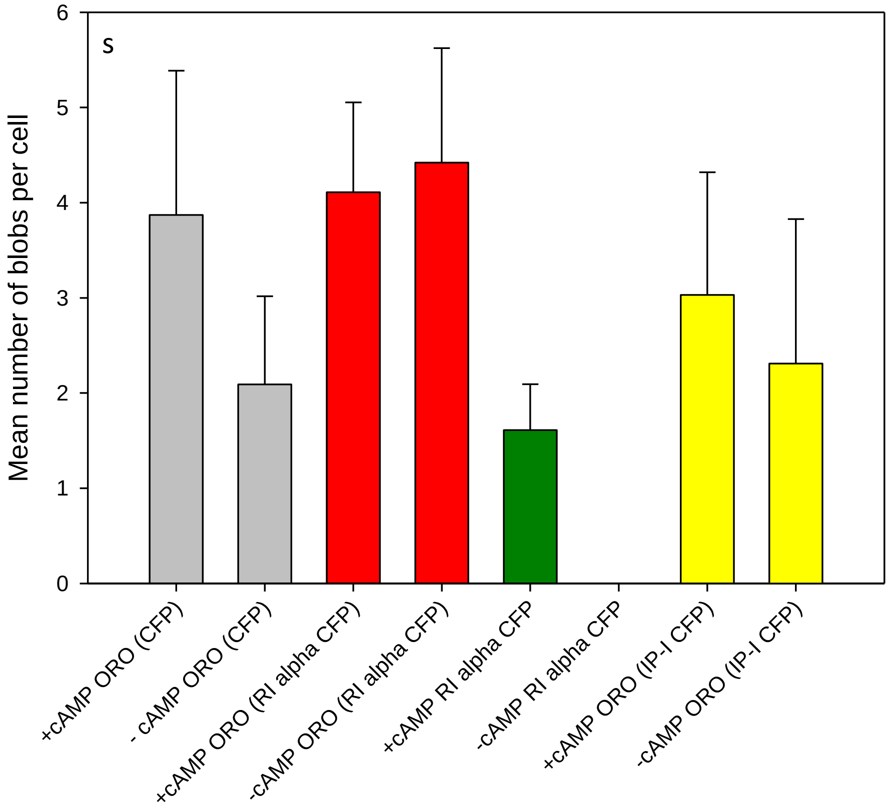

**Figure 5.3.5.3. RIα-CFP and Oil Red O puncta formation in B104 neuroblastoma cells in the presence or absence of dib-cAMP.** Fluorescence images of B104 cells following incubation with or without dib-cAMP for 4 days with corresponding fluorescence images of ORO puncta (red) and fluorescence overlay images. B104 cells transfected and labelled for a) –c) CFP and ORO + dib-cAMP, d) –f) CFP and ORO – dib-cAMP. g) –i) RIα-CFP and ORO + dib-cAMP, j) –l) RIα-CFP and ORO – dib-cAMP. m) –o) IP-I and ORO + dib-cAMP, p) –r) IP-I and ORO – dib-cAMP. s) Histogram displaying mean number of ORO puncta per cell in cells transfected with CFP (grey) and IP-I (yellow). Mean number of RIα-CFP puncta (green) in the presence of ORO puncta are also shown. Error bars shown s.e.m. (n = 3).

### 5.3.6. Differentiation in cerebellar granule neurons under chemical stimuli.

To confirm puncta formation in a more physiological neuronal system different methods of differentiation were applied for the differentiation of cerebellar granule neurons (CGNs). CGNs were cultured on glass cover slips and transfected with CFP (unlabelled CFP) and incubated with dib-cAMP, or pituitary adenylate cyclase- activating polypetide (PACAP). To test whether RIα targeting to AKAP 220 is required for dib-cAMP signalling in differentiation, a further set of samples were co- transfected with CFP and inhibitory peptide I (IP-I); a peptide specifically designed to bind RIα by mimicking the amphipathic AKAP binding helix (Burns-Hamuro et al. 2003). The treated cells were incubated for 7 days, fixed and imaged by fluorescence microscopy (Figure 5.3.6.1).

Mean neurite lengths were measured (Figure 5.3.6.1f), this showed the effect of dib-cAMP incubation on neurite length; one-way ANOVA tests comparing the CFP only control and each condition resulted in a significant difference in each case. Mean number of neurites per cell in each condition were also calculated (Figure 5.3.6.1g). A one-way ANOVA test against the CFP only control showed significant differences between each condition, except under incubation with PACAP, where no significant difference was observed, with a p value of 0.729. The mean branch length was measured (Figure 5.3.6.1h). One-way ANOVA tests against the CFP only control sample showed significant differences under each condition with a p value of 0.001 in all cases.

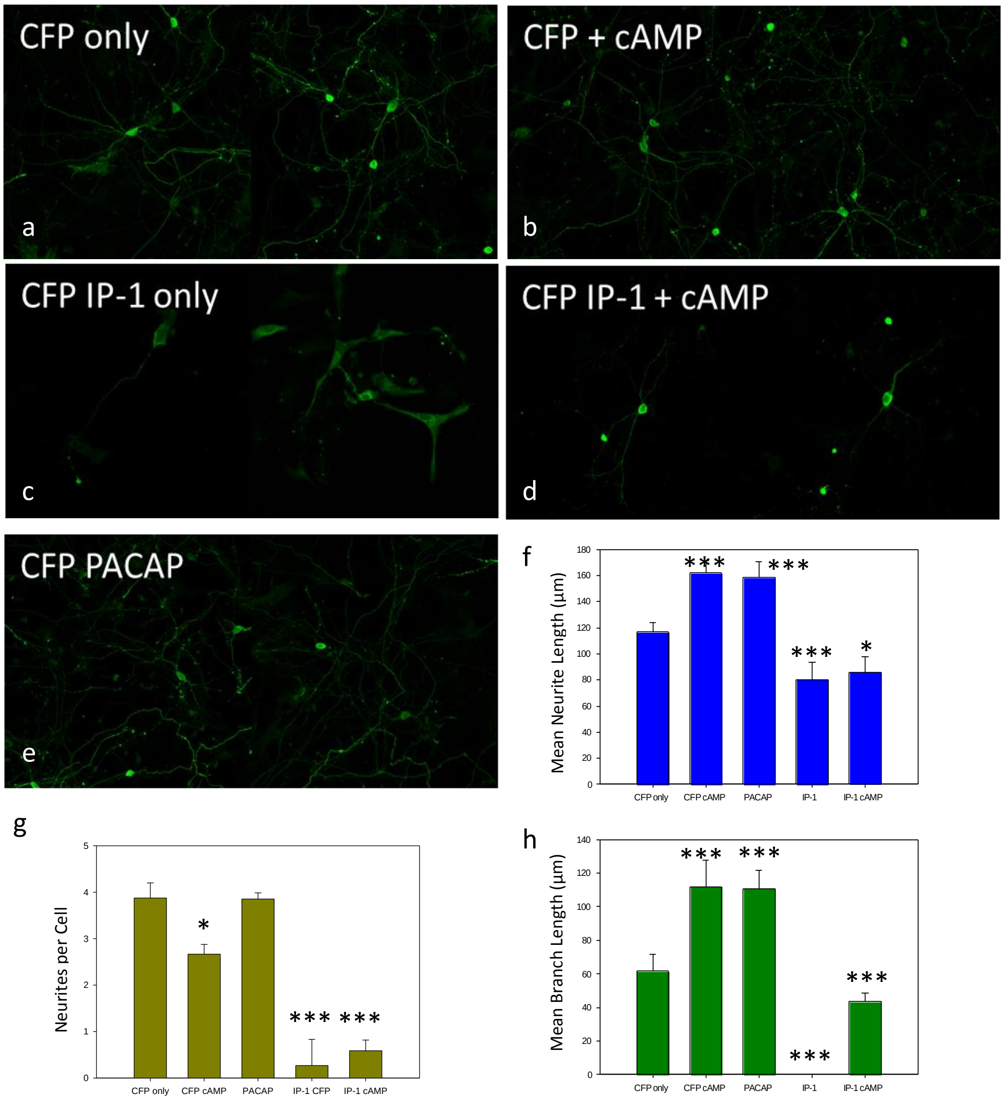

**Figure 5.3.6.1. Neuronal differentiation under chemical stimuli.** a)- e) Fluorescence images of hippocampal neurons. Transfected with a) CFP (CFP only) b) CFP, incubated with dib-cAMP c) IP-I only d) IP-I, incubated with dib-cAMP e) CFP only, incubated with PACAP. f) Mean neurite length. g) Mean number of neurites per cell. h) Mean branch length. Inset figures show P values of one way ANOVA tests against the CFP only control. Error bars show the s.e.m. for 90 measurements made on 3 separate biological replicates. P value stars; non- significant P= > 0.05, * = ≤ 0.05, ** = ≤ 0.01, *** = ≤ 0.001.

## 5.4 Discussion

Despite the identification of 6 dual specificity AKAPs, our understanding of the compartmentalisation of signalling involving Type I PKA is poor. A previous study shed light on one such mechanism, showing that stimulation of cAMP signalling in a range of cell types caused RIα and AKAP220 to accumulate in membranous organelles that resembled MVBs by TEM (Day et al. 2011). The investigation presented in this chapter sought to employ high-resolution imaging methods to discover whether the RIα-AKAP220 puncta formed in differentiating neuroblastoma cells also localised to MVBs. These investigations revealed no dib-cAMP-dependent co-localisation of RIα with MVBs or other punctate organelles tested, including lipid droplets and mitochondria. Although the cellular compartment responsible for RIα-AKAP220 targeting remains unknown, the FRAP and FLIP experiments in this chapter have revealed the dynamic nature of the puncta, which might give some insight into the role of this process in dib-cAMP-dependent neuronal differentiation. This research using high resolution microscopy approaches complements investigations conducted by Burgers et al. (2012). Here, by using bioinformatics tools in conjunction with fluorescence anisotropy, advances have been made to systematically identify AKAP binding motifs of a novel, PKA –RI specific AKAP. The characterisation of this small (11kDa) membrane peptide (smAKAP) revealed tethering to the plasma membrane through a dual acelaytion of the N terminal binding motif and the ability to target PKA –RI isoforms to the plasma membrane. MiniSOG was used in conjunction to identify the enrichment of cell –cell junctions by the plasma membrane targeted anchoring of PKA –RI isoforms (Burgers et al. 2012).

### Use of CLEM to investigate RIα co-localisation co-localisation with MVBs.

Localisation of RIα within MVBs was concluded from correlative fluorescence and TEM by Day et al (2011). The results of this experiment were not convincing, due to a lack of correlation between the fluorescent puncta observed and the electron dense areas that were present in the same focal plane of the same cell by TEM. It must also be noted that in these experiments no GFP staining, photoconversion or immunolabelling with electron dense material was used to enable imaging by electron microscopy. This calls in to question the correlation of the GFP fluorescence with electron dense areas by TEM, as GFP alone cannot be observed by TEM. In this chapter RIα-CFP localisation was investigated using CLEM methods as characterised in previous chapters.

RIα-CFP puncta within differentiated neuroblastoma cells were imaged using the ClairScope. This was carried out in order to identify localisation with the cell at high resolution and to further identify any associations with ultrastructure or localised proteins (Figure 5.3.1.2). Unfortunately, imaging showed no immunogold labelling visible within the transfected cells. This may have been due to the puncta being situated in the 3 dimensional structure of the hydrated cell sample, resulting in a lack of detection of the immunogold particles. For detection of electron dense material the electron beam must pass through the hydrated environment and sample. Back scattered electrons are then detected as the beam meets the electron dense material, which must passes back through to the detector, below the imaging window. Analysis of RIα-CFP puncta by imaging fluorescent z-stacks showed that on average the puncta localise ~4 µm within the cells. This would explain why immunogold labelling was not detected through ASEM imaging. The penetration of the electron beam in ASEM is ~3µm, with decreasing contrast observed with increasing penetration depth. To overcome this problem more classical methods in TEM could be used, such as serial sectioning with the possibility for 3D tomography of the sample to reveal interactions between the puncta and the cellular ultrastructure.

**RIα-CFP puncta are dynamic.**

The formation of RIα and AKAP 220 puncta was investigated with the aim of identifying the role of the proteins in differentiation of B104 neuroblastoma cells. It was calculated that the mean number of RIα-CFP puncta per cell was 12.6 ± 1.2 after 4 days incubation with dib-cAMP. Following removal of dib-cAMP and incubation in fresh, non- dib-cAMP containing media, no RIα-CFP puncta remained. A similar effect was seen in the reduction of AKAP 220 puncta formation, following removal of dib-cAMP.

As the puncta were seen to be dynamic over several days, further investigations were carried out by fluorescence recovery after photobleaching (FRAP) allowing the visualisation of puncta dynamics over a period of seconds to minutes (Figures 5.3.4.1a – e). Following bleaching of CFP puncta the rate of recovery was measured by live cell fluorescence microscopy, which was repeated on multiple samples. The recovery of the fluorescent puncta in the same area of original bleaching suggests that the RIα-CFP fluorescence was soluble and mobile, allowing the interchange of bleached and unbleached RIα-CFP molecules into the bleached area. If the RIα-CFP proteins were fully exchanged then the puncta would show 100 % recovery, through exchange with the free and unbleached cytoplasmic RIα-CFP. However, this was not observed as the puncta itself accounts for a significant percentage of available RIα-CFP, and a proportion of the RIα-CFP freely diffusing in the cytoplasm in the immediate bleach area around the puncta will also have been bleached. The observed percentage recovery will reflect the number of unbleached molecules remaining. The recovery of RIα-CFP fluorescence was observed to occur in the same region as the original bleach spot, suggesting that at this location RIα is in association with the cellular ultrastructure or anchoring proteins.

Fluorescence loss after photo bleaching was performed to confirm the mobility of the RIα-CFP molecules (Figures 5.3.4.2a –e). Fluorescence intensity of puncta was measured by live cell imaging throughout repeated bleaching of the cytoplasm away from the puncta within the same cell. After repetitive bleaching of the freely diffusing RIα-CFP in the cytoplasm, the RIα-CFP puncta also lost all fluorescence signal. This gave strong evidence that the clusters of RIα-CFP are able to freely exchange with the free molecules and thus are unlikely to be contained within a membranous structure, but are forming an open cluster within the cytoplasm for which molecules are constantly being exchanged and are in equilibrium with respect to bound and unbound proportions.

The interaction of PKA in the maintenance of the Golgi body was monitored revealing similar results in a study by (Bejarano et al. 2006). Measurement of FRAP of RIIα-GFP bleached at the Golgi body showed recovery of fluorescence at the Golgi body by exchange with cytoplasmic RIIα-GFP. FLIP was also carried out in the same study, where repeated bleaching of the cytoplasm showed the exchange of RIIα-GFP molecules between the cytoplasm and the Golgi body until all fluorescence was lost (Bejarano et al. 2006).

### Co-localisation of RIα CFP/FLAG

RIα-CFP and RIα-FLAG puncta development showed progressive development with co-localisation of the puncta observed to increase over time (Figures 5.3.2.1a –f; this is also shown as scatter plot in Figure 5.3.2.1g). The mean number of puncta per cell increased over time from 21 ± 0.4 % at 18 h and 46 ± 0.5 % co-localisation at 96 h (Figure 5.3.2.1h). The initial low amount of co-localisation may be a result of the differences in puncta development. It has been observed that the development of FLAG labelled RIα puncta occurred at a faster rate than RIα-CFP with mean number of RIα-CFP puncta ranging from 1.7 per cell at 1 hour and 4.2 per cell at 96 h of incubation with dib-cAMP respectively. The mean number of RIα-CFP puncta range from 1 puncta per cell at 1 hour and 3.3 per cell at 96 h. This delay in puncta formation may be due to the difference in labelling of the RIα sequence; the FLAG peptide tag consists of the peptide sequence DYKDDDDK (Einhauer et al. 2001). This may be less intrusive in live cell protein dynamics than the CFP label of RIα-CFP, which may act to delay puncta formation. Despite this, the RIα proteins labelled by each tag was shown to form puncta under identical conditions which co-localise over time and therefore may be used interchangeably. Further investigations which may reveal the composition and possible associations behind puncta formation include the application of techniques in molecular biology. This may include the tracking of puncta formation and involved proteins through western blotting to assess and compared the mass of proteins throughout formation. It may also be profitable to follow this by mass spectrometry of digested puncta proteins, with the aim of precisely identifying proteins involved.

### Which cellular compartment does RIα-CFP co-localise with?

Investigations into the co-localisation with cellular proteins and compartments were undertaken to verify studies conducted by Day et al (2011). The ESCRT protein ALIX is a major component of the multivesicular and late endosomal pathway, and would therefore be expected to co-localise with RIα incorporated in MVBs (Bissig & Gruenberg 2014). In differentiated B104 neuroblastoma cells no co-localisation was observed between RIα-CFP/ ALIX puncta (Figure 5.3.5.1). This suggests that RIα is not located within MVBs, as ALIX is involved in the formation of late endosomes and MVBs, the lack of co-localisation suggests that RIα is not involved in any stage of the formation of late endosomes or MVBs. The correlation of GFP-RIα observed by CLEM by Day et al (2011) may have been due to labelling artefacts. It is possible that ALIX and RIa did not co-localise due to transient association of ALIX with MVBs during their formation. This could be addressed by overexpressing a mutant form of Vps4 with RIa. Vps4 is an AAA ATPase endosomal associated protein that is involved in the disassembly of ESCRT proteins during MVB formation (Zahn et al. 2001). The mutant version inhibits this activity, preventing ESCRT disassembly, and remains associated with malformed MVBs (Raymond et al. 1992; Odorizzi et al. 1998). This could be tested experimentally in differentiated B104 neuroblastoma cells dual transfected with the mutant form of VPS4 and CFP- RIα. During differentiation and overexpression of the proteins malformation of MVBs would reveal the formation of CFP- RIα puncta at any point during MVB formation, effectively trapping the puncta, so that any transient association would be identifiable.

As no co-localisation of RIα with MVBs was observed, co-localisation with other punctate cellular compartments was investigated. The association of RIα puncta with mitochondria was investigated; increased concentrations of PKA and activated subunits have been observed within mitochondria due to the availability of ATP in the local environment (Lefkimmiatis et al. 2013). Transfection with the Mito dsRed plasmid resulted in labelling of the mitochondria through expression of a fluorescent red construct. Following analysis of the images acquired by confocal microscopy, it was observed that there was no co-localisation of RIα-CFP and Mito dsRed. This suggests that the RIα-CFP puncta are not in association with the mitochondria. It has been shown that mitochondria and AKAP1 are in association to anchor PKA in the local environment to promote phosphorylation of local effector proteins such as dynamin-related protein-1 (Drp-1). Also, when AKAP1 expression is knocked down neuronal survival is diminished, suggesting that PKA is crucial for the mitochondrial integrity and neuronal survival (Merrill & Strack 2014).

The accumulation of PKA around intracellular lipid droplets has been observed in adipocytes, possibly due to the presence of local high concentrations of dib-cAMP and PKA activation (Skalhegg & Tasken 2000). In order to ascertain whether the RIα puncta were co-localised with lipid droplets, differentiated B104 neuroblastoma cells transfected with either CFP, RIα-CFP or CFP IP-I were labelled with Oil red O (Figure 5.3.5.3 a -r). It was observed that lipid droplets and RIα-CFP puncta do not co-localise, which suggest that the RIα proteins do not form puncta in areas that may be intracellular sources of ATP. It was observed that in the absence of dib-cAMP fewer ORO stained lipid droplets were present, except in cells transfected with RIα-CFP. This suggests that dib-cAMP plays a role in the formation of lipid droplets (Brasaemle et al. 2000), although when RIα is overexpressed the formation of lipid droplets is recovered. A similar effect was seen in B104 neuroblastoma cells transfected with the inhibitory peptide CFP IP-I. In the absence of RIα, differentiation is suppressed, whereas in cells co-transfected with CFP IP-I and RIα differentiation and RIα puncta formation is recovered.

### Differentiation in cerebellar granule neurons.

Discovering a role for RIα-AKAP220 compartmentalisation in neuroblastoma cells is important in revealing a possible link between RIα localisation and neuronal differentiation. Previous studies have shown that specific localisation of RIα occurs through RIα association with AKAPs in the post synaptic terminal of the neuromuscular junction, creating micro- environments directing signalling pathways (Perkins et al. 2001). This PKA activation dependent pathway has also been reported to stimulate the differentiation of prostate cancer cells; in this study the absence of PKA activation by cAMP also showed inhibition of differentiation (Cox et al. 2000). This disruption of differentiation was achieved in research discussed in Chapter 5 through the use of inhibitory peptide-1 (IP-1), which specifically inhibited the interaction between cAMP and PKA binding sites. The inhibition of differentiation by IP-1 suggested localisation of RIα alone is necessary for the process because the peptide only inhibits AKAP binding and not kinase activity. To verify that this mechanism is also observed in the differentiation of central nervous system neurons, primary cultures of cerebellar granule neurons (CGNs) were transfected with CFP or CFP IP-I and treated with dib-cAMP or pituitary adenylate cyclase-activating polypeptide (PACAP). PACAP activates a GPCR that is a potent activator of adenylyl cyclase and has been shown to regulate the differentiation of cerebellar granule neurons *in vivo* (McIlvain et al. 2006).

Mean length of neurites per cell in each condition were calculated, with a one way ANOVA test showing that each data set was found to be significantly different to the CFP only control sample. The mean number of neurites per cell in each condition was also calculated, here a one-way ANOVA test confirmed each condition was significantly different apart from in the comparison of CFP only treated cells with PACAP treated cells. The mean number of branches per cell under each condition was calculated, once again showing significant difference between each condition in comparison to the CFP only control by a one way ANOVA test. These results confirm that neurons treated with dib-cAMP and PACAP have on average longer neurites and branches, although the number of neurites may not be significantly different. IP-I treated cells were observed to have significantly shorter and fewer neurites, even in the presence of dib-cAMP throughout culture.

Further investigations into the characterisation of RIα puncta might focus on localisation of RIα with proteins which are involved in cellular differentiation. The puncta we observe are reminiscent of P-bodies or stress granules and could be tested for co-localisation with RIa. Markers for these complexes include decapping protein 1 (Dcp1) (Rehwinkel et al. 2005). This protein is involved in the removal of the mRNA 5’ cap, a step that is important in the regulation of mRNA stability (Liu & Kiledjian 2006), which results in the formation of P-bodies, to degrade mis-folded mRNA. Other proteins that might interact with RIα as a result of differentiation are the proteins Argonaut 1 and 2 (Ago 1 and Ago2) and direct interaction partner, scaffold protein GW182 (Liu et al. 2005; Dueck et al. 2012). These proteins are crucial in the formation of processing bodies (P – bodies) where mRNA is promoted and mRNA decay occurs by interaction with the RNA –induced silencing (RISC) complex. Localisation of RIα with such proteins would provide a link to a specific role of RIα puncta as a function of differentiation in neuronal cells.

Future work into the importance of AKAP220 in differentiation involves investigations into the effect of IP-I on the development of AKAP220 puncta and also the use of an AKAP220 knockdown by the application of small hairpin RNA (shRNA). This method would identify the role of AKAP220 in differentiation; it is proposed that knockdown of AKAP220 would inhibit differentiation, which in turn would directly link localisation of the RIα puncta to a functional role in differentiation. These studies have revealed insights into the understanding of the role of dib-cAMP in the differentiation of neuroblastoma cells (via AKAP220). This could help in the development of more specific, targeted therapies in the treatment of neuroblastoma.

## 6.0 General Discussion

SRM and correlative microscopy techniques are at the forefront of current imaging approaches, but to bridge these technologies to enable the best of both modalities remains a challenge. ASEM offers the possibility of a new approach to overcoming some of these problems by enabling the imaging of the same sample by both fluorescence and EM. Utilising the novel JEOL ClairScope™, the first commercial ASEM, although naturally an *in situ* CLEM microscope, here we employed the e-beam in a very different approach than that envisaged by the manufacturer to develop a novel SRM technique. Not only was it possible to develop a direct approach to SRM, but the microscope permitted the collection of correlated fluorescence and EM images gathered from the sample while it remained fully hydrated and at atmospheric pressure.

This electron SRM (eSRM) technique complements other light derived SRM methodologies. Unlike many SRM techniques, the resolution is achieved within the raw image without the need for further image processing. This can significantly speed up the process of image visualisation compared to techniques such as PALM, STORM and SIM, which require extensive offline data analysis. As the resolution of the image itself is around 20 nm, higher densities of probes can be readily imaged. This should make it better suited to localising specific proteins and functional complexes whilst it gives an alternative approach to imaging the cellular ultrastructures.

The work presented here has shown that the ClairScope™ system enables the direct correlation of fluorescence and electron microscopy. A resolution of ~20 nm is achieved by immunolabelling fluorescent proteins with gold particles (Chapter 3). This imaging system was applied with the aim of using B104 neuroblastoma cells as a biological model system for the investigation of stimulated vesicle recycling (Chapter 4). Classical dyes and immunogold labelling were used to enable visualisation of vesicle populations and actively recycled vesicles within the 3 dimensional, hydrated sample. This formed the basis for investigative work into neuronal protein trafficking during the differentiation of neuroblastoma cells (Chapter 5).

## Achieving super resolution in hydrated samples at atmospheric pressure

The combination of adapted immunolabelling techniques with the novel imaging technology, the ClairScope™, enabled high resolution imaging of labelled proteins by direct labelling of fluorescent probes with 20 nm immunogold particles. This is a variation of the labelling methods used to visualise target proteins in previous studies by, for example, Nishiyama et al. (2010) and Hirano et al. (2014) where enhancement of 1.4nm gold labelling was used to create better contrast. The work presented in this thesis shows that by this direct labelling method it is possible to directly image actin filaments whilst also enabling the collection of correlated fluorescence and eSRM images using the ASEM. The imaging of actin filaments revealed the technicalities involved in sample optimisation, where the use of 20 nm immunogold revealed a sparse labelling pattern, rather than the filamentous structures observed by fluorescence microscopy.

In all techniques that use antibodies, saturation of primary antibody epitopes only reflects the saturation of available binding sites and does not account for sterically hindered sites and assumes no changes in isoform. The use of immunogold particles should enable one-to-one labelling of binding sites, as the particles have uniform size and binding ratio in comparison to fluorescent antibody markers where none or multiple fluorescent probes may be bound to a single antibody. This should allow for a more accurate protein localisation identification of protein clustering.

It was observed that the use of 15 nm immunogold appeared to produce a higher density actin labelling pattern. This enabled the high resolution imaging of the distribution of immunolabelled fluorescent actin filaments by directly correlated light and electron microscopy approaches. This suggests that steric hindrance caused by the probes themselves may be partly responsible for the lower than expected number of visualised probes. However, with decreasing probe size, the ability to image at a sufficient contrast became more challenging and would require a dish with a thinner silicon-nitride membrane to be available. Although these have been manufactured in the past and proven to increase resolution and contrast (Nishiyama et al. 2010a), they were not available for these studies. This does give encouragement for future studies at much higher resolution and the ability to use smaller probes. The analysis of the individual particles is useful in the optimisation of the imaging system, although once optimised it may be more productive to increase sample labelling density using a well resolved probe, with the aim to achieve maximum resolution for each sample and hence allow correlation to fluorescence imaging by using smaller probes. Through the availability of thinner membrane dishes, decreased probes sizes and potentially more sensitive detectors, the possibility of studying single labelled proteins at high densities should become achievable.

One approach to overcome the sensitivity and noise problems with regards to the detectors is being developed elsewhere, and utilises cathodoluminescence probes that permit the use of charge coupled device or photomultiplier detectors. These probes will permit multicolour labelling of samples with little background interference and hence increased signal to noise (Morrison et al. 2012).

Although there is no calibrated z-drive on the ASEM, it was still possible to generate 3D images. However, the e-beam has a very poor resolution in the axial z-plane compared to the lateral x,y resolution. This results in eSRM images that can have many particles focussed at once throughout a significant z-volume. Compared to raw images collected by other SRM techniques, the axial resolution is potentially very similar. Most of these techniques improve the lateral resolution rather than the axial resolution, which remains at around 700 nm (as reviewed in Huang et al. (2009)). TIRFM may be used for to improve resolution, but in turn this limits their applicability to membrane studies or no more than around 100 nm into the cytosol. As this eSRM imaging modality is still very new, no research has yet investigated deconvolution approaches to help improve the axial resolution using similar approaches to those employed in light microscopy; reviewed by Schermelleh et al. (2010).

It was hoped that CLEM imaging could be done by collecting fluorescence images and then preparing the sample with heavy metal stains to gather fine ultrastructural details using backscattered electrons in the ASEM whilst the sample remained *in situ*. Although this was possible, the resolution was not that normally associated with electron microscopy (~20 nm compared to 1-2 nm). The contrast was also decreased as the e-beam was presumably broadened as it travelled through the SiN membrane and entered the hydrated environment. This prevented the use of DAB and would also limit its ability to study other low contrast photoconversion probes, e.g. miniSOG; reviewed by Shu et al. (2011). Therefore, the use of high contrast probes, such as immunogold was desired for further studies.

The immunogold labelling method was carried forward for the imaging and study of granular vesicular distribution. This used vesicles containing the intraluminal fluorescent marker spH to permit correlated imaging with standard immunolabelling techniques.

The JEOL ClairScope™ may be used in conjunction with traditional imaging technologies; as a result in this research a novel imaging approach was achieved; a sample was imaged through a series of z-planes, to produce a z-stack by ASEM of vesicle labelling in differentiated neuroblastoma cells. This novel method does not replace the use of traditional imaging techniques where z-stacks are achieved at high resolution, such as TEM, FIB and serial block face sectioning. These techniques involved intensive sample processing such as milling the block face of a resin embedded sample to reveal stepped layers throughout the sample. These are particularly detrimental as at each stage the sample is destroyed through the milling process. Approaches such as serial tape sectioning can be used to achieve higher resolution, and retain the sectioned samples for repeated imaging. These techniques are still limited as they produce images of dehydrated or embedded cell structures and sections become distorted by the sectioning procedure. The development of novel probes is a growing area of research, especially in the development of bi-functional probes which can be readily used in CLEM to study cellular activity in relation to ultrastructure (Kamimura et al. 2008; Carpenter et al. 2012). Such probes could be used in flow cytometry to validate the binding efficiency of EM probes.

### Can ASEM be used for imaging cellular activity?

The work presented in Chapters 4 and 5 represent the first work on the use of novel methods using ASEM with the aim to correlate cellular activity and high-resolution ultrastructural detail by the use of bi-functional probes, for example, photoconvertible FM dyes. Experiments focussed on the visualisation of actively recycled vesicles in stimulated, differentiated neuroblastoma cells. It was acknowledged that imaging whole cells by an electron beam brings limitations, mainly due to limited penetration and production of detectable back-scattered electron signal.

Photoconversion was observed by fluorescence, bright field microscopy and TEM in this thesis, although when the hydrated samples were imaged by ASEM no electron dense areas were observed. The same method was used in Quantomix capsules and imaged using a JEOL 7600 FEGSEM and again no photoconverted electron dense material was observed, suggesting that although photoconversion had taken place, the density of material within the samples was not great enough to create the quantity of backscattered electrons required for detection by ASEM. Therefore it was concluded that photoconversion of FM dye was not suitable for use in the aqueous environment afforded by ASEM. This was a particular caveat in imaging of the actively recycled population of vesicles in stimulated neuroblastoma cells. The photoconversion of FM dyes has been shown to be successful for imaging by TEM and has been used in several CLEM studies (Harata et al. 2001; Darcy et al. 2006a; Darcy et al. 2006b; Marra et al. 2012; Marra et al. 2014). The development of bi-functional markers, which allow fluorescence and electron microscopy include the possible use of platinum derivatives such as platinum blue to label the actively recycling population (Inaga et al. 2007). Quantum dots are often used to correlate fluorescence with EM, although they are generally large in comparison to vesicles and are more suited to imaging by TEM; imaging by SEM is achievable (Drbohlavova et al. 2009), although problematic, and this may be even worse when imaged in an aqueous environment.

Since photoconversion was ineffective primary antibody labelling was then attempted to label new endocytosed vesicles. This led to further challenges in imaging cellular activity by ASEM, including the detection of antibody labelling of the actively recycled vesicles. Secondary labelling of primary antibody after stimulation exhibited specific membrane staining after stimulation of differentiated neuroblastoma cells. By fluorescence microscopy the specific binding of the primary antibody was clearly observed, however internalisation could not be confirmed. When imaged by ASEM, when the primary antibody was labelled with secondary immunogold no staining was seen. This may have been due to steric effects on the cell surface caused by the extracellular matrix preventing 20 nm gold labelled antibodies from penetrating the membrane and accessing the primary antibody.

Gadolinium phosphors may be another option for the visualisation of endocytosis (Morrison et al. 2015). These may be imaged in an aqueous environment and detected by scanning electron microscopy in direct correlation with cathodoluminescence; a process by which a fluorescent emission may be detected by the electron microscope following excitation by the electron beam. An advantage of this approach is that the probes themselves can be smaller than the 20 nm gold particles and the electron beam is used only to excite, with no need for backscattered electron detection, therefore allowing deeper penetration in systems such as ASEM. Development of such methods would benefit the studies of protein localisation, through the specific labelling of target proteins within a fully hydrated cell sample. Although this may be possible in fixed cells, imaging by ASEM is not ideally suited to imaging live cells.

### Using ASEM to investigate localisation of proteins in differentiation.

ASEM labelling methods confirmed in this thesis were used to investigate the localisation of the PKA subunit RIα. This work reproduced studies conducted by Day et al (2011), where it was shown that RIα incorporated into MVBs. In this study the immunogold labelling was not visible due to the limitations of imaging centrally located labelled proteins, as previously described, although further studies into RIα localisation were made using other high-resolution fluorescence microscopy techniques. This publication also highlighted a previous study into the localisation of RIα with testicular peroxisomes (Lester et al. 1996), although this was shown not to be the case in MEF cells labelled with antibody specific for peroxisomes (PMP70) (Day et al. 2011).

The use of immunolabelling revealed no colocalisation of RIα with the MVB marker ALIX (an ESCRT protein involved in MVB formation) or with other proteins known to be associated with PKA. These puncta were also observed in primary culture neurons, showing that the formation of the puncta was not an artefact due to the differentiation of neuroblastoma cell lines.

### The localisation of the RIα and AKAPs

The fact that the FLIP results show exchange with the cytoplasmic RIα-CFP fluorescence and FRAP of the RIα-CFP puncta was observed in localised areas suggests that the puncta have a defined nucleation point. This suggests that the puncta may be in association with the cellular ultrastructure or even with proteins such as AKAPs, resulting in structured organisation. The organisation of AKAPs in regard to PKA and RIα localisation still requires investigation to gain insight into the nature of RIα during differentiation. It was observed in this study that in non-differentiated neuroblastoma cells, RIα is dispersed throughout the cell; following differentiation RIα puncta are formed. Due to this change in localisation in dib-cAMP treated cells it is thought that RIα puncta formation may be a function of differentiation and may possibly have a role in neuronal plasticity.

This may be investigated further by the use of conventional TEM methods, to reveal the ultrastructural detail and any associations with immunolabelled puncta. Investigations may also be enhanced by the use of ASEM, or CLEM, which could reveal the association between distinct labelled proteins or with respect to the organisation of the hydrated cellular structure. Extensive studies into the organisation and interactions of AKAPs have revealed multiple interactions between cellular ultrastructure and proteins in the local environment. These interactions in neuronal cells are thought to be important in long-term synaptic plasticity. AKAP79/ 150 (AKAP 5) is known to be a scaffolding protein, which binds PKA along with a number of signalling, scaffolding and ion channel proteins (Dacher et al. 2013). It has also been shown that AKAP79/150 binds several adenylyl cyclase isoforms in neurons, which further suggests a crucial role in the cAMP pathway and neuronal differentiation (Sanderson et al. 2012). The organisation of AKAP79/150 suggests that the protein acts as a linker between F-actin, cadherins and kinases, especially between PKA. There is also evidence to suggest that anchoring of calcineurin results in the regulation of $Ca^{2+}$ permeable AMP receptors, a key role in mediating synaptic plasticity during long-term potentiation (Dittmer et al. 2014).

## Future Work

Investigations further to those presented in this thesis could combine correlative imaging methods with biochemical techniques, by labelling the RIα protein to enable protein isolation and identification. This could then be linked with studies using FRET to define the protein-protein interactions within the live cell and EM to reveal the ultrastructural organisation.

The continued development of techniques and novel technologies in CLEM and ASEM must take into consideration the requirements for high-resolution imaging of biological samples. The ClairScope™ enables the imaging of a hydrated sample at atmospheric pressure, whereas most other techniques require the removal of these elements, for imaging under vacuum. Although fluorescence may be correlated with the high resolution images acquired, the original hydrated 3 dimensional state of the cell is lost; to achieve high resolution imaging of a biological sample in its live state the sample must remain un-fixed, hydrated throughout processing and imaging. Techniques for preservation of as close to ‘live state’ as possible include HPF and cryo fixation as previously discussed (Verkade 2008). With improvements to technologies such as the ClairScope™ it may be possible to achieve resolution imaging similar to PALM/STORM, where ASEM may be carried out through a z-stack (as demonstrated in this thesis) to identify and resolve the location of individual labelled proteins throughout the sample.

This technique would also enable true fluorescence correlation, through alignment of fluorescent z-stacks acquired by confocal microscopy.

To improve further on this imaging technique, live cell real-time video imaging is possible; this could be very useful to visualise the endocytosis of fluid phase markers by stimulated neuronal cells. In addition to this the use of cathodoluminescence from nanophosphor probes, as previously discussed, could provide enhanced imaging techniques, such as improved electron beam penetration. This would also potentially enable multicolour imaging for precise high-resolution correlation of target proteins and the cell ultrastructure. This could prove useful to probe the potential interactions between AKAPs and the cellular ultrastructure, and to investigate synaptic vesicle distributions in the presynaptic terminal. Although the ClairScope, in this study, has not been shown to be a beneficial standalone technique for high resolution imaging it does offer a novel approach, which may be used in conjunction with various robust super resolution techniques. This combination may be beneficial in the study of a number of cellular processes which are currently at the forefront of super resolution technology development; these include the investigation of SNARE proteins in vesicular trafficking and budding (Bar-On et al. 2012), reviewed by (Maglione & Sigrist 2013); and the involvement of ESCRT proteins in intracellular and viral protein trafficking (Engelenburg et al. 2014). In studies focussing primarily on neuronal development, the ClairScope may be used in conjunction with SRM techniques to investigate long-term potentiation (LTP) and the organisation of vesicles in relation to trafficking proteins in the pre- and post-synaptic terminals. This research would significantly advance our understanding of how such signalling proteins are organised and their roles in neuronal differentiation and plasticity, and potentially identify targets for drug therapies in treatment of childhood neuroblastoma.

## List of Abbreviations

| | |
|---|---|
| AKAP | A-kinase anchor protein |
| ALIX | Apoptosis linked gene 2iinteracting proteins X; or scaffold associated protein |
| ANOVA | Analysis of variance |
| ASEM | Atmospheric scanning electron microscope |
| ATP | Adenosine triphosphate |
| AZ | Active zone |
| BDNF | Brain derived neurotrophic factor |
| BSA | Bovine serum albumin |
| CaM | Calmodulin |
| cAMP | 3',5'-cyclic adenylyl monophosphate |
| CFP | Cyan fluorescent protein |
| CGN | Cerebellar granule neuron |
| CLEM | Correlated light and electron microscopy |
| CLSM | Confocal laser scanning microscopy |
| cpGFP | Circularly permuted green fluorescent protein |
| cpYFP | Circularly permuted yellow fluorescent protein |
| cryo-ET | Cryo-electron tomography |
| DA | Doperminergic |
| DAB | Diaminobenzidine |
| DAPI | Diamidino-2-phenyl indole |
| DIC | Differential interference microscopy |
| DMEM | Dulbecco's modified Eagles medium |
| DNA | Deoxyribonucleic acid |

| | |
|---|---|
| dSTORM | Direct stochastic optical reconstruction microscopy |
| EDTA | Ethylene diamine tetra-acetic acid |
| EM | Electron microscopy |
| ER | Endoplasmic reticulum |
| ESCRT | Endosomal sorting complex required for transport |
| FEGSEM | Field emission gun scanning electron micrscope |
| FIB | Focussed ion beam (milling) |
| FISH | Fluorescence in-situ hybridisation |
| FLAsH | Fluorescein biarsenical tetracysteine probe |
| FLIP | Fluorescence loss in photobleaching |
| FLM | Fluorescence light microscopy |
| FM | Fei Mao (FM dyes) |
| FNG | Fluoronanogold |
| FRAP | Fluorescence recovery after photobleaching |
| FRET | Fluorescence/Forster resonance energy transfer |
| GFP | Green fluorescent protein |
| GPCR | G-protein coupled receptors |
| HPF | High pressure freezing |
| IF | Immunofluorescence |
| IgG | Immunoglobulin G |
| iLEM | Integrated light and electron microscopy |
| IP-1 | Inhibitory protein 1 |
| LABE | Low angle backscatter electron |
| LAMP-1 | Lysosome-associated membrane glycoprotein |
| LB | Luria broth |

| | |
|---|---|
| MEK | Mitogen activated protein kinase |
| miniSOG | Mini singlet oxygen generator |
| MVB | Multivesicular body |
| ORO | Oil red O |
| PACAP | Pituitary adenylate cyclase-activating peptide |
| paGFP | Photoactivatable green fluorescent protein |
| PALM | Photoactivated localisation microscopy |
| PBS | Phosphate buffered saline |
| PFA | Paraformaldehyde |
| PKA | Protein kinase A |
| PMT | Photomultiplier tube |
| PSF | Point spread function |
| ReAsH | Resorufin biarsenical tetracysteine probe |
| RI,RII | PKA regulatory subunits I and II |
| RISC | RNA induced silencing complex |
| ROXS | Oxidising and reducing buffer system |
| SBF | Serial block face |
| SEM | Scanning electron microscopy |
| SIM | Structured illumination microscopy |
| SiN | Silicon nitride |
| SNAP | Synaptosomal-associated protein |
| SNARE | Soluble NSF (N-ethylamide-sensitive factor) attachment protein receptor |
| SOFI | Super-resolution optical fluctuation imaging |
| SPFI | Single particle fluorescence imaging |
| spH | Synaptofluorin |

| | |
|---|---|
| SRM | Super resolution light microscopy |
| SS | Spot size |
| STED | Stimulated emission depletion microscopy |
| STORM | Stochastic optical reconstruction microscopy |
| TEM | Transmission electron microscopy |
| TIRFM | Total internal reflectance microscopy |
| UA | Uranyl acetate |
| VAMP | Vesicle associated membrane protein |
| VEC-DEC | Video enhanced contrast differential interference contrast |
| VTC | Vesicular tubular complexes |
| WGA | Wheat germ agglutinin |

# Bibliography

Abbe, E., 1873. Beiträge zur Theorie des Mikroskops und der mikroskopischen Wahrnehmung. *Archiv für mikroskopische Anatomie*, 9(1), pp.413–418.

Adams, S.R. et al., 2002. New biarsenical ligands and tetracysteine motifs for protein labeling in vitro and in vivo: synthesis and biological applications. J. Am. Chem. Soc. 124(21), pp.6063–6076.

Adams, S.R. & Tsien, R.Y., 2008. Preparation of the membrane-permeant biarsenicals FlAsH-EDT2 and ReAsH-EDT2 for fluorescent labeling of tetracysteine-tagged proteins. Nat. Protoc., 3(9), pp.1527–1534.

Akimoto, M. et al., 2013. Signaling through dynamic linkers as revealed by PKA. *PNAS*, 110(35), pp.14231–14236.

Akita, M. et al., 2013. Detection of CD133 (prominin-1) in a human hepatoblastoma cell line (HuH-6 clone 5). Microsc. Res. Tech, 76(8), pp.844–852.

Albrecht, R.M., Goodman, S.L. & Simmons, S.R., 1989. Distribution and movement of membrane-associated platelet glycoproteins: Use of colloidal gold with correlative video-enhanced light microscopy, low-voltage high-resolution scanning electron microscopy, and high-voltage transmission electron microscopy. *Am J Anat*, 185(2-3), pp.149–164.

Allen, R.D. et al., 1982. Fast axonal transport in squid giant axon. *Science*, 218(4577), pp.1127–1129.

Allen, R.D., David, G.B. & Nomarski, G., 1969. The zeiss-Nomarski differential interference equipment for transmitted-light microscopy. *Zeitschrift Für Wissenschaftliche Mikroskopie Und Mikroskopische Technik*, 69(4), pp.193–221.

Anderson, J.C. et al., 1994. Map of the synapses formed with the dendrites of spiny stellate neurons of cat visual cortex. *J Comp Neurol*, 341(1), pp.25–38.

Andreska, T. et al., 2014. High abundance of BDNF within glutamatergic presynapses of cultured hippocampal neurons. Front Cell Neurosci, 8, p.107.

Ardenne, M. von, 1938. Das Elektronen-Rastermikroskop. *Zeitschrift für Physik*, 109(9-10), pp.553–572.

Axelrod, D., 1981. Cell-substrate contacts illuminated by total internal reflection fluorescence. *J Cell Biol*, 89(1), pp.141–145.

Bannykh, S.I., 1996. The organization of endoplasmic reticulum export complexes. *J Cell Biol*, 135(1), pp.19–35.

Bar-On, D. et al., 2012. Super-resolution Imaging Reveals the Internal Architecture of Nano-sized Syntaxin Clusters. *J. Biol Chem*, 287(32), pp.27158–27167.

Bates, M., Blosser, T.R. & Zhuang, X., 2005. Short-Range Spectroscopic Ruler Based on a Single-Molecule Optical Switch. *PRL*, 94(10), p.108101.

Bauman, A.L., Goehring, A.S. & Scott, J.D., 2004. Orchestration of synaptic plasticity through AKAP signaling complexes. *Neuropharmacology*, 46(3), pp.299–310.

Bean, B.P., 2007. The action potential in mammalian central neurons. *Nat. Rev. Neurosci*, 8(6), pp.451–465.

Bejarano, E. et al., 2006. Golgi structural stability and biogenesis depend on associated PKA activity. *J Cell Sci*, 119(18), pp.3764–3775.

Bertrand, C.A. & Frizzell, R.A., 2003. The role of regulated CFTR trafficking in epithelial secretion. *Am J Physiol - Cell Physiology*, 285(1), pp.C1–C18.

Betzig, E. et al., 2006. Imaging intracellular fluorescent proteins at nanometer resolution. *Science (New York, N.Y.)*, 313(5793), pp.1642–1645.

Bezzi, P. & Volterra, A., 2014. Imaging Exocytosis and Recycling of Synaptic-Like Microvesicles in Astrocytes. *Cold Spring Harb Protoc*, 2014(5), p.pdb.prot081711.

Bianchi, S. et al., 2013. Synaptogenesis and development of pyramidal neuron dendritic morphology in the chimpanzee neocortex resembles humans. *PNAS*, 110(Suppl 2), pp.10395–10401.

Binder, M.D., Hirokawa, N. & Windhorst, U. eds., 2009. En Passant Synapses. *Encyclopedia of Neuroscience*. Springer Berlin Heidelberg, pp. 1100–1100.

Bissig, C. & Gruenberg, J., 2014. ALIX and the multivesicular endosome: ALIX in Wonderland. *Trends Cell Biol*, 24(1), pp.19–25.

Bleckert, A., Photowala, H. & Alford, S., 2012. Dual pools of actin at presynaptic terminals. *J Neurophysiol*, 107(12), pp.3479–3492.

Bloom, O. et al., 2003. Colocalization of synapsin and actin during synaptic vesicle recycling. *The J Cell Biol*, 161(4), pp.737–747.

Bohrmann, B. & Kellenberger, E., 2001. Cryosubstitution of frozen biological specimens in electron microscopy: use and application as an alternative to chemical fixation. *Micron*, 32(1), pp.11–19.

Braet, F. et al., 2014. Combining wide-field super-resolution microscopy and electron tomography: rendering nanoscopic correlative arrays on subcellular architecture. *Methods Cell Biol*, 124, pp.129–149.

Branco, T. et al., 2008. Local Dendritic Activity Sets Release Probability at Hippocampal Synapses. *Neuron*, 59(3), pp.475–485.

Brasaemle, D.L. et al., 2000. Perilipin A Increases Triacylglycerol Storage by Decreasing the Rate of Triacylglycerol Hydrolysis. *J. Biol. Chem*, 275(49), pp.38486–38493.

Brown, D.A., 2001. Lipid droplets: Proteins floating on a pool of fat. *Curr. Biol*, 11(11), pp.R446–R449.

Bucci, C. et al., 2000. Rab7: A Key to Lysosome Biogenesis. *Mol. Biol Cell*, 11(2), pp.467–480.

Budzinski, K.L. et al., 2011. Measurements of the acidification kinetics of single SynaptopHluorin vesicles. *Biophys. J*, 101(7), pp.1580–1589.

Burgers, P.P. et al., 2012. A Small Novel A-Kinase Anchoring Protein (AKAP) That Localizes Specifically Protein Kinase A-Regulatory Subunit I (PKA-RI) to the Plasma Membrane. *J. Biol Chem*, 287(52), pp.43789–43797.

Burns-Hamuro, L.L. et al., 2003. Designing isoform-specific peptide disruptors of protein kinase A localization. *PNAS*, 100(7), pp.4072–4077.

Burrone, J., Li, Z. & Murthy, V.N., 2007. Studying vesicle cycling in presynaptic terminals using the genetically encoded probe synaptopHluorin. *Nat. Protoc*, 1(6), pp.2970–2978.

Bushby, A.J. et al., 2012. Correlative light and volume electron microscopy: using focused ion beam scanning electron microscopy to image transient events in model organisms. *Methods Cell Biol*, 111, pp.357–382.

Carpenter, C.M. et al., 2012. Radioluminescent nanophosphors enable multiplexed small-animal imaging. *Opt. Express*, 20(11), pp.11598–11604.

Del Castillo, J. & Katz, B., 1954. Quantal components of the end-plate potential. *J. Physiol*, 124(3), pp.560–573.

Chalfie, M. et al., 1994. Green fluorescent protein as a marker for gene expression. *Science*, 263(5148), pp.802–805.

Chattopadhyay, P.K., Hogerkorp, C.-M. & Roederer, M., 2008. A chromatic explosion: the development and future of multiparameter flow cytometry. J. *Immunol*, 125(4), pp.441–449.

Chavis, P. et al., 1998. Visualization of cyclic AMP-regulated presynaptic activity at cerebellar granule cells. *Neuron*, 20(4), pp.773–781.

Cherry, R.J. et al., 1998. Detection of Dimers of Dimers of Human Leukocyte Antigen (HLA)–DR on the Surface of Living Cells by Single-Particle Fluorescence Imaging. *J. Cell Biol*, 140(1), pp.71–79.

Cheutin, T. et al., 2007. Visualizing Macromolecules with Fluoronanogold: From Photon Microscopy to Electron Tomography. In J. R. McIntosh, ed. *Methods Cell Biol.*, pp. 559–574.

Chevrier, D.M., Chatt, A. & Zhang, P., 2012. Properties and applications of protein-stabilized fluorescent gold nanoclusters: short review. *J. Nanophotonics*, 6(1).

Clayton, E.L., Evans, G.J.O. & Cousin, M.A., 2008. Bulk Synaptic Vesicle Endocytosis Is Rapidly Triggered during Strong Stimulation. *J. Neurosci*, 28(26), pp.6627 –6632.

Coghlan, V.M. et al., 1995. Association of protein kinase A and protein phosphatase 2B with a common anchoring protein. *Science*, 267(5194), pp.108–111.

Corbin, J.D. & Keely, S.L., 1977. Characterization and regulation of heart adenosine 3’:5’-monophosphate-dependent protein kinase isozymes. *J. Biol. Chem*, 252(3), pp.910–918.

Corish, P. & Tyler-Smith, C., 1999. Attenuation of green fluorescent protein half-life in mammalian cells. *Protein Eng.*, 12(12), pp.1035–1040.

Cousin, M.A. & Evans, G.J.O., 2011. Activation of silent and weak synapses by cAMP-dependent protein kinase in cultured cerebellar granule neurons. *J. Physiol*, 589(8), pp.1943–1955.

Cox, M.E. et al., 2000. Activated 3′,5′-Cyclic AMP-dependent Protein Kinase Is Sufficient to Induce Neuroendocrine-like Differentiation of the LNCaP Prostate Tumor Cell Line. *J. Biol. Chem*, 275(18), pp.13812–13818.

Cox, S. et al., 2012. Bayesian localization microscopy reveals nanoscale podosome dynamics. *Nat. Meth*, 9(2), pp.195–200.

Cremer, C. & Cremer, T., 1978. Considerations on a laser-scanning-microscope with high resolution and depth of field. *Microsc. Acta*, 81(1), pp.31–44.

Dacher, M. et al., 2013. A-Kinase Anchoring Protein–Calcineurin Signaling in Long-Term Depression of GABAergic Synapses. *J. Neurosci*, 33(6), pp.2650–2660.

Dahan, M. et al., 2001. Time-gated biological imaging by use of colloidal quantum dots. *Opt. Letters*, 26(11), pp.825–827.

Dao, K.K. et al., 2006. Epac1 and cAMP-dependent Protein Kinase Holoenzyme Have Similar cAMP Affinity, but Their cAMP Domains Have Distinct Structural Features and Cyclic Nucleotide Recognition. *J. Biol. Chem*, 281(30), pp.21500–21511.

Darcy, K.J. et al., 2006a. An ultrastructural readout of fluorescence recovery after photobleaching using correlative light and electron microscopy. *Nat. Protoc*, 1(2), pp.988–994.

Darcy, K.J. et al., 2006b. Constitutive sharing of recycling synaptic vesicles between presynaptic boutons. *Nat. Neurosci*, 9(3), pp.315–321.

Day, M.E. et al., 2011. Isoform-specific targeting of PKA to multivesicular bodies. *J.Cell Biol*, 193(2), pp.347–363.

Deerinck, T.J. et al., 1994. Fluorescence photooxidation with eosin: a method for high resolution immunolocalization and in situ hybridization detection for light and electron microscopy. *J. Cell Biol*, 126(4), pp.901–910.

Delgado-Álvarez, D.L. et al., 2010. Visualization of F-actin localization and dynamics with live cell markers in Neurospora crassa. *Fungal Genet.Biol*, 47(7), pp.573–586.

Dell'Acqua, M.L. et al., 2006. Regulation of neuronal PKA signaling through AKAP targeting dynamics. *Eur J. Cell Biol*, 85(7), pp.627–633.

Denker, A. et al., 2011. A small pool of vesicles maintains synaptic activity in vivo. *PNAS*.

Denk, W. & Horstmann, H., 2004. Serial Block-Face Scanning Electron Microscopy to Reconstruct Three-Dimensional Tissue Nanostructure. *PLoS Biol*, 2(11).

Dertinger, T. et al., 2009. Fast, background-free, 3D super-resolution optical fluctuation imaging (SOFI). *PNAS*, 106(52), pp.22287–22292.

Dittmer, P.J., Dell'Acqua, M.L. & Sather, W.A., 2014. Ca2+/Calcineurin-Dependent Inactivation of Neuronal L-Type Ca2+ Channels Requires Priming by AKAP-Anchored Protein Kinase A. *Cell Rep*, 7(5), pp.1410–1416.

Dobell, C. & Leeuwenhoek, A. van, 1932. *Antony van Leeuwenhoek and his "Little animals".* New York,: Harcourt, Brace and company,. Available at: http://www.biodiversitylibrary.org/item/47806.

Drake, K.R., Kang, M. & Kenworthy, A.K., 2010. Nucleocytoplasmic Distribution and Dynamics of the Autophagosome Marker EGFP-LC3. *PLoS ONE*, 5(3).

Drbohlavova, J. et al., 2009. Quantum Dots — Characterization, Preparation and Usage in Biological Systems. *Int J.Mol.Sci*, 10(2), pp.656–673.

Dubochet, J. et al., 1988. Cryo-electron microscopy of vitrified specimens. *Q. Rev. Biophys*, 21(02), pp.129–228.

Dubochet, J. et al., 2007. How to "read" a vitreous section. *Methods Cell Biol*, 79, pp.385–406.

Dueck, A. et al., 2012. microRNAs associated with the different human Argonaute proteins. *Nucleic Acids Res*, 40(19), pp.9850–9862.

Dulubova, I. et al., 2007. Munc18-1 binds directly to the neuronal SNARE complex. *PNAS*, 104(8), pp.2697–2702.

Durst, S. et al., 2014. Organization of perinuclear actin in live tobacco cells observed by PALM with optical sectioning. *J. Plant Physiol*, 171(2), pp.97–108.

Dyab, A.K.F. & Paunov, V.N., 2010. Particle stabilised emulsions studied by WETSEM technique. *Soft Matter*, 6(12), pp.2613–2615.

Ebihara, T. et al., 2015. The Atmospheric Scanning Electron Microscope (ASEM) observes the Cultured Fluorescent Neuron. *Microsc. Microanal*, 21(Supplement S3), pp.889–890.

Eggeling, C., Willig, K.I. & Barrantes, F.J., 2013. STED microscopy of living cells – new frontiers in membrane and neurobiology. *J. Neurochem.*, 126(2), pp.203–212.

Einhauer, A. & Jungbauer, A., 2001. The FLAG$^{TM}$ peptide, a versatile fusion tag for the purification of recombinant proteins. *J. Biochem. Bioph Meth*, 49(1–3), pp.455–465.

Ekimov, A.I., Efros, A.L. & Onushchenko, A.A., 1985. Quantum size effect in semiconductor microcrystals. *Solid State Commun*, 56(11), pp.921–924.

Ellis, R.J., 2001. Macromolecular crowding: obvious but underappreciated. *Trends Biochem Sci*, 26(10), pp.597–604.

Engelenburg, S.B.V. et al., 2014. Distribution of ESCRT Machinery at HIV Assembly Sites Reveals Virus Scaffolding of ESCRT Subunits. *Science*, 343(6171), pp.653–656.

Faas, F.G.A. et al., 2013. Localization of fluorescently labeled structures in frozen-hydrated samples using integrated light electron microscopy. *J. Struct Biol*, 181(3), pp.283–290.

Fatt, P. & Katz, B., 1952. Spontaneous subthreshold activity at motor nerve endings. *J. Physiol*, 117(1), pp.109–128.

Förster, T., 1948. Zwischenmolekulare Energiewanderung und Fluoreszenz. *Annalen der Physik*, 437(1-2), pp.55–75.

Frackowiak, D., 1988. The Jablonski diagram. *J. Photochem. Photobiol*, 2(3), p.399.

Fredj, N.B. & Burrone, J., 2009. A resting pool of vesicles is responsible for spontaneous vesicle fusion at the synapse. *Nat Neurosci*, 12(6), pp.751–758.

Gaffield, M.A. & Betz, W.J., 2007. Imaging synaptic vesicle exocytosis and endocytosis with FM dyes. *Nat. Protoc*, 1(6), pp.2916–2921.

Gaietta, G. et al., 2002. Multicolor and Electron Microscopic Imaging of Connexin Trafficking. *Science*, 296(5567), pp.503–507.

Gandhi, S.P. & Stevens, C.F., 2003. Three modes of synaptic vesicular recycling revealed by single-vesicle imaging. *Nature*, 423(6940), pp.607–613.

Geissbuehler, S., Dellagiacoma, C. & Lasser, T., 2011. Comparison between SOFI and STORM. *Biomed Opt. Express*, 2(3), pp.408–420.

Giepmans, B.N.G. et al., 2005. Correlated light and electron microscopic imaging of multiple endogenous proteins using Quantum dots. *Nat Methods*, 2(10), pp.743–749.

Granata, A. et al., 2008. The dystonia-associated protein torsinA modulates synaptic vesicle recycling. *J. Biol. Chem*, 283(12), pp.7568–7579.

Greengard, P. et al., 1993. Synaptic vesicle phosphoproteins and regulation of synaptic function. *Science*, 259(5096), pp.780 –785.

Griffin, B.A., Adams, S.R. & Tsien, R.Y., 1998. Specific covalent labeling of recombinant protein molecules inside live cells. *Science*, 281(5374), pp.269–272.

Gross, L.A. et al., 2000. The structure of the chromophore within DsRed, a red fluorescent protein from coral. *PNAS* 97(22), pp.11990–11995.

Gusnard, D. & Kirschner, R.H., 1977. Cell and organelle shrinkage during preparation for scanning electron microscopy: effects of fixation, dehydration and critical point drying. *J. Microsc*, 110(1), pp.51–57.

Gustafsson, M.G.L., 2000. Surpassing the lateral resolution limit by a factor of two using structured illumination microscopy. *J. Microsc*, 198(2), pp.82–87.

Han, J. et al., 2007. Spatial targeting of type II protein kinase A to filopodia mediates the regulation of growth cone guidance by cAMP. *The Journal of Cell Biology*, 176(1), pp.101–111.

Harata, N. et al., 2001. Visualizing recycling synaptic vesicles in hippocampal neurons by FM 1-43 photoconversion. *Proceedings of the National Academy of Sciences of the United States of America*, 98(22), pp.12748–12753.

Harata, N. et al., 2001. Visualizing recycling synaptic vesicles in hippocampal neurons by FM 1-43 photoconversion. *Proceedings of the National Academy of Sciences of the United States of America*, 98(22), pp.12748–12753.

Heim, R., Cubitt, A.B. & Tsien, R.Y., 1995. Improved green fluorescence. *Nature*, 373(6516), pp.663–664.

Heim, R., Prasher, D.C. & Tsien, R.Y., 1994. Wavelength mutations and posttranslational autoxidation of green fluorescent protein. *Proceedings of the National Academy of Sciences of the United States of America*, 91(26), pp.12501–12504.

Hein, B., Willig, K.I. & Hell, S.W., 2008. Stimulated emission depletion (STED) nanoscopy of a fluorescent protein-labeled organelle inside a living cell. *Proceedings of the National Academy of Sciences*, 105(38), pp.14271–14276.

Hell, S.W., 2007. Far-Field Optical Nanoscopy. *Science*, 316(5828), pp.1153–1158.

Hell, S.W. & Wichmann, J., 1994. Breaking the diffraction resolution limit by stimulated emission: stimulated-emission-depletion fluorescence microscopy. *Optics Letters*, 19(11), pp.780–782.

Herberg, F.W. et al., 2000. Analysis of A-kinase anchoring protein (AKAP) interaction with protein kinase A (PKA) regulatory subunits: PKA isoform specificity in AKAP binding. *Journal of Molecular Biology*, 298(2), pp.329–339.

Heuser, J., 1989. The role of coated vesicles in recycling of synaptic vesicle membrane. *Cell Biology International Reports*, 13(12), pp.1063–1076.

Heuser, J.E. & Reese, T.S., 1973.Evidence for recycling of synaptic vesicle membrane during transmitter release at the frog neuromuscular junction. *The Journal of Cell Biology*, 57(2), pp.315–344.

Heymann, J.A.W. et al., 2006. Site-specific 3D imaging of cells and tissues with a dual beam microscope. *Journal of Structural Biology*, 155(1), pp.63–73.

Hines, M.A. & Guyot-Sionnest, P., 1996. Synthesis and Characterization of Strongly Luminescing ZnS-Capped CdSe Nanocrystals. *The Journal of Physical Chemistry*, 100(2), pp.468–471.

Hirano, K. et al., 2014. Electron microscopy of primary cell cultures in solution and correlative optical microscopy using ASEM. *Ultramicroscopy*, 143, pp.52–66.

Hirokawa, N., 1989. The cytoskeletal architecture of the presynaptic terminal and molecular structure of synapsin 1. *The Journal of Cell Biology*, 108(1), pp.111–126.

Holmes, K.C. et al., 1990. Atomic model of the actin filament. *Nature*, 347(6288), pp.44–49.

Hooke, R., 1665. Micrographia; National library of medicine. (https://ceb.nlm.nih.gov/proj/ttp/flash/hooke/hooke.html)

Hoopmann, P., Rizzoli, S.O. & Betz, W.J., 2012. FM Dye Photoconversion for Visualizing Synaptic Vesicles by Electron Microscopy. *Cold Spring Harb Protoc*, 2012(1), p.pdb.prot067611.

Huang, B., Bates, M. & Zhuang, X., 2009. Super resolution fluorescence microscopy. *Annu. Rev. Biochem.*, 78, pp.993–1016.

Inaga, S. et al., 2007. Platinum blue as an alternative to uranyl acetate for staining in transmission electron microscopy. *Arch. Histol. Cytol*, 70(1), pp.43–49.

Izeddin, I. et al., 2011. Super-Resolution Dynamic Imaging of Dendritic Spines Using a Low-Affinity Photoconvertible Actin Probe. *PLoS ONE*, 6(1).

Jarnaess, E. et al., 2008. Dual specificity A-kinase anchoring proteins (AKAPs) contain an additional binding region that enhances targeting of protein kinase A type I. *J. Biol Chem*, 283(48), pp.33708–33718.

Jablonski, A., 1933. Efficiency of anti-stokes fluorescence in dyes. Nature. pp.839-840

Jordan, R., Lemke, E.A. & Klingauf, J., 2005. Visualization of Synaptic Vesicle Movement in Intact Synaptic Boutons Using Fluorescence Fluctuation Spectroscopy. *Biophy. J*, 89(3), pp.2091–2102.

Kamimura, M. et al., 2008. Design of poly(ethylene glycol)/streptavidin coimmobilized upconversion nanophosphors and their application to fluorescence biolabeling. *Langmuir*, 24(16), pp.8864–8870.

Kanemaru, T. et al., 2009. A fluorescence scanning electron microscope. *Ultramicrosc*, 109(4), pp.344–349.

Karki, R. et al., 2013. βIII-Tubulin: biomarker of taxane resistance or drug target? *Expert opin. ther. targets*, 17(4), pp.461–472.

Katoh, K. et al., 2003. The ALG-2-interacting protein Alix associates with CHMP4b, a human homologue of yeast Snf7 that is involved in multivesicular body sorting. *J.Biol Chem*, 278(40), pp.39104–39113.

Katz, A., Bentur, A. & Kovler, K., 2007. A novel system for in-situ observations of early hydration reactions in wet conditions in conventional SEM. *Cement and Concrete Res*, 37(1), pp.32–37.

Kellenberger, E., 1987. The Response of Biological Macromolecules and Supramolecular Structures to the Physics of Specimen Cryopreparation. In P. D. R. A. Steinbrecht & D. K. Zierold, eds. *Cryotechniques in Biological Electron Microscopy*. Springer Berlin Heidelberg, pp. 35–63.

Kenworthy, A.K. et al., 2004. Dynamics of putative raft-associated proteins at the cell surface. *J. Cell Biol*, 165(5), pp.735–746.

Kinoshita, T. et al., 2014. Immuno-Electron Microscopy of Primary Cell Cultures from Genetically Modified Animals in Liquid by Atmospheric Scanning Electron Microscopy. *Microsc. Microanal*, 20(02), pp.470–484.

Klar, T.A. et al., 2000. Fluorescence microscopy with diffraction resolution barrier broken by stimulated emission. *PNAS*, 97(15), pp.8206–8210.

Klenchin, V.A. & Martin, T.F.J., 2000. Priming in exocytosis: Attaining fusion-competence after vesicle docking. *Biochimie*, 82(5), pp.399–407.

Knoll M, und Ruska E., 1932. Das Elektronenmikroskop. Zeitschrift für Physik. pp.318–339

Knott, G. et al., 2008. Serial Section Scanning Electron Microscopy of Adult Brain Tissue Using Focused Ion Beam Milling. *J. Neurosci*, 28(12), pp.2959–2964.

Kopek, B.G. et al., 2012. Correlative 3D superresolution fluorescence and electron microscopy reveal the relationship of mitochondrial nucleoids to membranes. *PNAS*, 109(16), pp.6136–6141.

Kopperud, R. et al., 2002. Formation of inactive cAMP-saturated holoenzyme of cAMP-dependent protein kinase under physiological conditions. *J. Biol Chem*, 277(16), pp.13443–13448.

Krebs, E.G., Graves, D.J. & Fischer, E.H., 1959. Factors affecting the activity of muscle phosphorylase b kinase. *J. Biol Chem*, 234, pp.2867–2873.

Kuge, O. et al., 1994. Sar1 promotes vesicle budding from the endoplasmic reticulum but not Golgi compartments. *J. Cell Biol*, 125(1), pp.51–65.

Kümmel, D. et al., 2011. Complexin cross-links prefusion SNAREs into a zigzag array. *Nat. Struc. Mol. Biol*, 18(8), pp.927–933.

Lampe, A. et al., 2012. Multi-colour direct STORM with red emitting carbocyanines. *Biology of the Cell*, 104(4), pp.229–237.

Lange, F. de et al., 2001. Cell biology beyond the diffraction limit: near-field scanning optical microscopy. *J. Cell Sci*, 114(23), pp.4153–4160.

Lefkimmiatis, K., Leronni, D. & Hofer, A.M., 2013. The inner and outer compartments of mitochondria are sites of distinct cAMP/PKA signaling dynamics. *J. Cell Biol*, 202(3), pp.453–462.

Lester, L.B. et al., 1996. Cloning and Characterization of a Novel A-kinase Anchoring Protein AKAP 220, association with testicular peroxisomes. *J. Biol  Chem*, 271(16), pp.9460–9465.

Liu, H. & Kiledjian, M., 2006. Decapping the message: a beginning or an end. *Biochem. Soc. Trans*, 34(Pt 1), pp.35–38.

Liu, J. et al., 2005. A role for the P-body component GW182 in microRNA function. *Nat Cell Biol*, 7(12), pp.1261–1266.

Liv, N. et al., 2014. Scanning electron microscopy of individual nanoparticle bio-markers in liquid. *Ultramicrosc*, 143, pp.93–99.

Liv, N. et al., 2013. Simultaneous Correlative Scanning Electron and High-NA Fluorescence Microscopy. *PLoS ONE*, 8(2).

Lombardi, D. et al., 1993. Rab9 functions in transport between late endosomes and the trans Golgi network. *EMBO J.*, 12(2), pp.677–682.

Lu, H.E. et al., 2014. Multiple Spatial and Kinetic Subpopulations of CaMKII in Spines and Dendrites as Resolved by Single-Molecule Tracking PALM. *J. Neurosci*, 34(22), pp.7600–7610.

Lukinavičius, G. et al., 2014. Fluorogenic probes for live-cell imaging of the cytoskeleton. *Nat Methods*, 11(7), pp.731–733.

Luo, W. et al., 2013. Single-molecule monitoring in living cells by use of fluorescence microscopy. *Anal. Bioanal. Chem*, 405(1), pp.43–49.

Maglione, M. & Sigrist, S.J., 2013. Seeing the forest tree by tree: super-resolution light microscopy meets the neurosciences. *Nat Neurosci*, 16(7), pp.790–797.

Mahul-Mellier, A.-L. et al., 2006. Alix, Making a Link between Apoptosis-Linked Gene-2, the Endosomal Sorting Complexes Required for Transport, and Neuronal Death In Vivo. *The J. Neurosci*, 26(2), pp.542–549.

Malgaroli, A. et al., 1995. Presynaptic Component of Long-Term Potentiation Visualized at Individual Hippocampal Synapses. *Science*, 268(5217), pp.1624–1628.

Mani, M. & Ryan, T.A., 2009. Live imaging of synaptic vesicle release and retrieval in dopaminergic neurons. *Front Neural Circuits*, 3, p.3.

Marra, V. et al., 2012. A Preferentially Segregated Recycling Vesicle Pool of Limited Size Supports Neurotransmission in Native Central Synapses. *Neuron*, 76(3-3), pp.579–589.

Marra, V. et al., 2014. Ultrastructural readout of functional synaptic vesicle pools in hippocampal slices based on FM dye labeling and photoconversion. *Nat Protoc*, 9(6), pp.1337–1347.

Maruyama, Y., Ebihara, T., Nishiyama, H., Konyuba, Y., et al., 2012. Direct observation of protein microcrystals in crystallization buffer by atmospheric scanning electron microscopy. *Int. J. Mol. Sci*, 13(8), pp.10553–10567.

Maruyama, Y., Ebihara, T., Nishiyama, H., Suga, M., et al., 2012. Immuno EM-OM correlative microscopy in solution by atmospheric scanning electron microscopy (ASEM). *Journal of Structural Biology*, 180(2), pp.259–270.

Matsuoka, S. et al., 2012. Single-molecule imaging of stochastic signaling events in living cells. *Cold Spring Harb Protoc*, 2012(3), pp.267–278.

Mattheyses, A.L., Simon, S.M. & Rappoport, J.Z., 2010. Imaging with total internal reflection fluorescence microscopy for the cell biologist. *J. Cell Sci*, 123(Pt 21), pp.3621–3628.

McDonald, K.L. & Webb, R.I., 2011. Freeze substitution in 3 hours or less. *J. Microsc*, 243(3), pp.227–233.

McIlvain, H.B. et al., 2006. Pituitary adenylate cyclase-activating peptide (PACAP) induces differentiation in the neuronal F11 cell line through a PKA-dependent pathway. *Brain Res*, 1077(1), pp.16–23.

McIntosh, R., Nicastro, D. & Mastronarde, D., 2005. New views of cells in 3D: an introduction to electron tomography. *Trend Cell Biol*, 15(1), pp.43–51.

Medine, C.N. et al., 2007. Munc18-1 prevents the formation of ectopic SNARE complexes in living cells. *J. Cell Sci*, 120(24), pp.4407–4415.

Melan, M.A. & Sluder, G., 1992. Redistribution and Differential Extraction of Soluble Proteins in Permeabilized Cultured Cells. Implications for Immunofluorescence Microscopy. *J. Cell Sci*, 101(4), pp.731–743.

Memtily, N. et al., 2015. Observation of tissues in open aqueous solution by atmospheric scanning electron microscopy: Applicability to intraoperative cancer diagnosis. *Int. J Oncol*, 46(5), pp.1872–1882.

Merrill, R.A. & Strack, S., 2014. Mitochondria: A kinase anchoring protein 1, a signaling platform for mitochondrial form and function. *Int J.Biochem.Cell Biol*, 48, pp.92–96.

Midgley, P.A. & Weyland, M., 2003. 3D electron microscopy in the physical sciences: the development of Z-contrast and EFTEM tomography. *Ultramicrosc*, 96(3–4), pp.413–431.

Miesenböck, G., De Angelis, D.A. & Rothman, J.E., 1998. Visualizing secretion and synaptic transmission with pH-sensitive green fluorescent proteins. *Nature*, 394(6689), pp.192–195.

Mingos, D.M.P., 2014. Gold Clusters, Colloids and Nanoparticles. Springer.

Monterisi, S. et al., 2012. CFTR regulation in human airway epithelial cells requires integrity of the actin cytoskeleton and compartmentalized cAMP and PKA activity. *J. Cell Sci*, 125(5), pp.1106–1117.

Moor, H., 1987. Theory and Practice of High Pressure Freezing. In P. D. R. A. Steinbrecht & D. K. Zierold, eds. *Cryotechniques in Biological Electron Microsc*. pp. 175–191.

Morrison, I.E. et al., 1994. Analysis of receptor clustering on cell surfaces by imaging fluorescent particles. *Biophy J.*, 67(3), pp.1280–1290.

Morrison, I.E.G. et al., 2012. Atmospheric scanning electron microscope for correlative microscopy. *MethodsCell Biol.*, 111, pp.307–324.

Morrison, I.E.G. et al., 2015. Multicolour correlative imaging using phosphor probes. *J. Chem. Biol*, pp.1–9.

Moseley, J.B. & Goode, B.L., 2006. The Yeast Actin Cytoskeleton: from Cellular Function to Biochemical Mechanism. *Microbiol Mol. Biol Rev*, 70(3), pp.605–645.

Mundigl, O. & De Camilli, P., 1994. Formation of synaptic vesicles. *Curr. Opin Cell Biol*, 6(4), pp.561–567.

Murai, T. et al., 2011. Low cholesterol triggers membrane microdomain-dependent CD44 shedding and suppresses tumor cell migration. *J. Biol Chem*, 286(3), pp.1999–2007.

Murai, T. et al., 2013. Ultrastructural analysis of nanogold-labeled cell surface microvilli in liquid by atmospheric scanning electron microscopy and their relevance in cell adhesion. *Int. J. Mol Sci*, 14(10), pp.20809–20819.

Murray, C.B., Norris, D.J. & Bawendi, M.G., 1993. Synthesis and characterization of nearly monodisperse CdE (E = sulfur, selenium, tellurium) semiconductor nanocrystallites. *J. Am Chem Soc*, 115(19), pp.8706–8715.

Nagai, T. et al., 2001. Circularly permuted green fluorescent proteins engineered to sense Ca2+. *PNAS*, 98(6), pp.3197–3202.

Nikonenko, I. et al., 2005. Application of photoconversion technique for correlated confocal and ultrastructural studies in organotypic slice cultures. *Microsc. Res Tech*, 68(2), pp.90–96.

Nirenberg, M. et al., 1983. Modulation of Synapse Formation by Cyclic Adenosine Monophosphate. *Science*, 222(4625), pp.794–799.

Nishiyama, H. et al., 2010a. Atmospheric scanning electron microscope observes cells and tissues in open medium through silicon nitride film. *J Struc.Biol*, 169(3), pp.438–449.

Nishiyama, H., Koizumi, M., et al., 2014. Atmospheric scanning electron microscope system with an open sample chamber: configuration and applications. *Ultramicrosc*, 147, pp.86–97.

Nishiyama, H., Teramoto, K., et al., 2014. Positively charged nanogold label allows the observation of fine cell filopodia and flagella in solution by atmospheric scanning electron microscopy. *Microsc Res. Tech*, 77(2), pp.153–160.

Nishiyama, H. et al., 2010b. Reprint of: Atmospheric scanning electron microscope observes cells and tissues in open medium through silicon nitride film. *J. Struc.Biol*, 172(2), pp.191–202.

Nisman, R. et al., 2004. Application of quantum dots as probes for correlative fluorescence, conventional, and energy-filtered transmission electron microscopy. *J. Hist. Cytochem*, 52(1), pp.13–18.

Orloff, J., Swanson, L.W. & Utlaut, M., 1996. Fundamental limits to imaging resolution for focused ion beams. *J.Vac Sci Tech*, 14(6), pp.3759–3763.

Ormö, M. et al., 1996. Crystal Structure of the Aequorea victoria Green Fluorescent Protein. *Science*, 273(5280), pp.1392–1395.

Papaioannou, G. & McHugh, K., 2005. Neuroblastoma in childhood: review and radiological findings. *Cancer Imag.*, 5(1), pp.116–127.

Patterson, G.H. & Lippincott-Schwartz, J., 2002. A photoactivatable GFP for selective photolabeling of proteins and cells. *Science (New York, N.Y.)*, 297(5588), pp.1873–1877.

Peddie, C.J. et al., 2014. Correlative and integrated light and electron microscopy of in-resin GFP fluorescence, used to localise diacylglycerol in mammalian cells. *Ultramicrosc*, 143, pp.3–14.

Peddie, C.J. & Collinson, L.M., 2014. Exploring the third dimension: volume electron microscopy comes of age. *Micron*, 61, pp.9–19.

Peng, X., Wickham, J. & Alivisatos, A.P., 1998. Kinetics of II-VI and III-V Colloidal Semiconductor Nanocrystal Growth: "Focusing" of Size Distributions. *J. Am Chem.Soc*, 120(21), pp.5343–5344.

Perkins, G.A. et al., 2001. PKA, PKC, and AKAP localization in and around the neuromuscular junction. *BMC Neurosci,* 2(1), p.17.

Pidoux, G. et al., 2011. Optic atrophy 1 is an A-kinase anchoring protein on lipid droplets that mediates adrenergic control of lipolysis. *EMBO J*, 30(21), pp.4371–4386.

Pieribone, V.A. et al., 1995. Distinct pools of synaptic vesicles in neurotransmitter release. *, Nature.* 375(6531), pp.493–497.

Plitzko, J.M., Rigort, A. & Leis, A., 2009. Correlative cryo-light microscopy and cryo-electron tomography: from cellular territories to molecular landscapes. *Curr. Opin Biotech*, 20(1), pp.83–89.

Powell, R.D. et al., 1997. A covalent fluorescent-gold immunoprobe: simultaneous detection of a pre-mRNA splicing factor by light and electron microscopy. *J. Histochem. Cytochem.* 45(7), pp.947–956.

Powell, R.D., Halsey, C.M.R. & Hainfeld, J.F., 1998. Combined fluorescent and gold immunoprobes: Reagents and methods for correlative light and electron microscopy. *Microsc Res Tech*, 42(1), pp.2–12.

Presley, J.F. et al., 1997. ER-to-Golgi transport visualized in living cells. *Nature*, 389(6646), pp.81–85.

Pumplin, D.W., Reese, T.S. & Llinás, R., 1981. Are the presynaptic membrane particles the calcium channels? *PNAS*, 78(11), pp.7210 –7213.

Ratnayaka, A. et al., 2011. Extrasynaptic vesicle recycling in mature hippocampal neurons. *Nat Commun*, 2, p.531.

Rayleigh Lord., 1879. XXXI. Investigations in optics, with special reference to the spectroscope. *Philosophical Magazine Series 5*, 8(49), pp.261–274.

Rayleigh Lord., 1896. XV. On the theory of optical images, with special reference to the microscope. *Philosophical Magazine Series 5*, 42(255), pp.167–195.

Rehwinkel, J. et al., 2005. A crucial role for GW182 and the DCP1:DCP2 decapping complex in miRNA-mediated gene silencing. *RNA*, 11(11), pp.1640–1647.

Riedl, J. et al., 2008. Lifeact: a versatile marker to visualize F-actin. *Nat methods*, 5(7), p.605.

Rigort, A. et al., 2012. Focused Ion Beam Micromachining of Eukaryotic Cells for Cryoelectron Tomography. *PNAS*, 109(12), pp.4449–4454.

Rijnsoever, C. van, Oorschot, V. & Klumperman, J., 2008. Correlative light-electron microscopy (CLEM) combining live-cell imaging and immunolabeling of ultrathin cryosections. *Nat Methods*, 5(11), pp.973–980.

Robinson, J.M. & Takizawa, T., 2009. Correlative fluorescence and electron microscopy in tissues: immunocytochemistry. *J. Microsc*, 235(3), pp.259–272.

Rust, M.J., Bates, M. & Zhuang, X., 2006. Stochastic optical reconstruction microscopy (STORM) provides sub-diffraction-limit image resolution. *Nat methods*, 3(10), pp.793–795.

Ryan, T.A. & Reuter, H., 2001. Measurements of vesicle recycling in central neurons. *News in Physiological Sciences: PNAS,* 16, pp.10–14.

Sanderson, J.L. et al., 2012. AKAP150-Anchored Calcineurin Regulates Synaptic Plasticity by Limiting Synaptic Incorporation of Ca2+-Permeable AMPA Receptors. *J. Neurosci*, 32(43), pp.15036–15052.

Sartori, A. et al., 2007. Correlative microscopy: bridging the gap between fluorescence light microscopy and cryo-electron tomography. *J. Sruct Biol*, 160(2), pp.135–145.

Sato, C. et al., 2012. Rapid imaging of mycoplasma in solution using Atmospheric Scanning Electron Microscopy (ASEM). *Biochem. Biophys. Res. Commun*, 417(4), pp.1213–1218.

Scales, S.J., Pepperkok, R. & Kreis, T.E., 1997. Visualization of ER-to-Golgi Transport in Living Cells Reveals a Sequential Mode of Action for COPII and COPI. *Cell*, 90(6), pp.1137–1148.

Schafer, D. & Anthony Jones, E., 1982. Hepatic encephalopathy and the γ-aminobutyric-acid neurotransmitter system. *The Lancet*, 319(8262), pp.18–20.

Schermelleh, L., Heintzmann, R. & Leonhardt, H., 2010. A guide to super-resolution fluorescence microscopy. *J. Cell Biol*, 190(2), pp.165–175.

Schnell, U. et al., 2012. Immunolabeling artifacts and the need for live-cell imaging. *Nature Methods*, 9(2), pp.152–158.

Schouten, M. et al., 2014. Imaging dendritic spines of rat primary hippocampal neurons using structured illumination microscopy. *J. Visual. Exper: JoVE*, (87).

Scott, J.D., Dessauer, C.W. & Taskén, K., 2013. Creating order from chaos: cellular regulation by kinase anchoring. *Annu. Rev. Pharm.Tox*, 53, pp.187–210.

Sengupta, P., van Engelenburg, S.B. & Lippincott-Schwartz, J., 2014. Superresolution Imaging of Biological Systems Using Photoactivated Localization Microscopy. *Chem. Rev*, 114(6), pp.3189–3202.

Sengupta, P., Van Engelenburg, S. & Lippincott-Schwartz, J., 2012. Visualizing Cell Structure and Function with Point-Localization Superresolution Imaging. *Develop. Cell*, 23(6), pp.1092–1102.

Shepherd, G.M. & Harris, K.M., 1998. Three-dimensional structure and composition of CA3-->CA1 axons in rat hippocampal slices: implications for presynaptic connectivity and compartmentalization. *J. Neurosci:*, 18(20), pp.8300–8310.

Sheppard, C.J. & Wilson, T., 1981. The theory of the direct-view confocal microscope. *J. Microsc*, 124(Pt 2), pp.107–117.

Shi, X., Lim, J. & Ha, T., 2010. Acidification of the Oxygen Scavenging System in Single-Molecule Fluorescence Studies: In Situ Sensing with a Ratiometric Dual-Emission Probe. *Anal. Chem*, 82(14), pp.6132–6138.

Shulman, R.G. et al., 2004. Energetic basis of brain activity: implications for neuroimaging. *Trend Neurosci*, 27(8), pp.489–495.

Shupliakov, O. et al., 2002. Impaired recycling of synaptic vesicles after acute perturbation of the presynaptic actin cytoskeleton. *PNAS*, 99(22), pp.14476–14481.

Shu, X. et al., 2011. A Genetically Encoded Tag for Correlated Light and Electron Microscopy of Intact Cells, Tissues, and Organisms. *PLoS Biol*, 9(4).

Sidell, N., 1982. Retinoic acid-induced growth inhibition and morphologic differentiation of human neuroblastoma cells in vitro. *J. Nat.Cancer Inst,* 68(4), pp.589–596.

Skalhegg, B.S. & Tasken, K., 2000. Specificity in the cAMP/PKA signaling pathway. Differential expression,regulation, and subcellular localization of subunits of PKA. *Front Biosci.* 5.

Small, J.V., 1988. The actin cytoskeleton. *Electron Microsc. Rev*, 1(1), pp.155–174.

Staras, K. et al., 2010. A Vesicle Superpool Spans Multiple Presynaptic Terminals in Hippocampal Neurons. *Neuron*, 66(1), pp.37–44.

Studer, D., Humbel, B.M. & Chiquet, M., 2008. Electron microscopy of high pressure frozen samples: bridging the gap between cellular ultrastructure and atomic resolution. *Histochem. Cell Biol*, 130(5), pp.877–889.

Südhof, T.C., 1995. The synaptic vesicle cycle: a cascade of protein-protein interactions. *Nature*, 375(6533), pp.645–653.

Suga, M. et al., 2011. The Atmospheric Scanning Electron Microscope with open sample space observes dynamic phenomena in liquid or gas. *Ultramicrosc*, 111(12), pp.1650–1658.

Sutherland EW, 1970. ON the biological role of cyclic amp. *JAMA*, 214(7), pp.1281–1288.

Takizawa, T. & Robinson, J.M., 2000. FluoroNanogold is a bifunctional immunoprobe for correlative fluorescence and electron microscopy. *J. Histochem. Cytochem*, 48(4), pp.481–486.

Takizawa, T., Suzuki, K. & Robinson, J.M., 1998. Correlative microscopy using FluoroNanogold on ultrathin cryosections. Proof of principle. *J. Histochem. Cytochem*, 46(10), pp.1097–1102.

Tam, J. et al., 2014. Cross-Talk-Free Multi-Color STORM Imaging Using a Single Fluorophore. *PLoS ONE*, 9(7).

Tang, S. et al., 2014. Cyclic-AMP-dependent protein kinase (PKA) activity assay based on FRET between cationic conjugated polymer and chromophore-labeled peptide. *The Analyst*, 139(18), pp.4710–4716.

Taskén, K. & Aandahl, E.M., 2004. Localized effects of cAMP mediated by distinct routes of protein kinase A. *Physiol Rev*, 84(1), pp.137–167.

Tatavarty, V. et al., 2009. Investigating Sub-Spine Actin Dynamics in Rat Hippocampal Neurons with Super-Resolution Optical Imaging. *PLoS ONE*, 4(11).

Templeton, A.C., Wuelfing, W.P. & Murray, R.W., 2000. Monolayer-Protected Cluster Molecules. *Acc. Chem. Res*, 33(1), pp.27–36.

Thiberge, S. et al., 2004. Scanning electron microscopy of cells and tissues under fully hydrated conditions. *PNAS*, 101(10), pp.3346–3351.

Thomas, K.G. & Kamat, P.V., 2003. Chromophore-Functionalized Gold Nanoparticles. *Acc. Chem. Res*, 36(12), pp.888–898.

Thompson, R.E., Larson, D.R. & Webb, W.W., 2002. Precise nanometer localization analysis for individual fluorescent probes. *Biophys. J*, 82(5), pp.2775–2783.

Thorley, J.A., Pike, J. & Rappoport, J.Z., 2014. Chapter 14 - Super-resolution Microscopy: A Comparison of Commercially Available Options. In A. Cornea & P. M. Conn, eds. *Fluorescence Microscopy*. Boston: Academic Press, pp. 199–212.

Tojima, T., Kobayashi, S. & Ito, E., 2003. Dual role of cyclic AMP-dependent protein kinase in neuritogenesis and synaptogenesis during neuronal differentiation. *Journal of Neurosci. Res*, 74(6), pp.829–837.

Topell, S., Hennecke, J. & Glockshuber, R., 1999. Circularly permuted variants of the green fluorescent protein. *FEBS Letters*, 457(2), pp.283–289.

Tsien, R.Y., 1998. The Green Fluorescent Protein. *Annu. Rev. Biochem*, 67(1), pp.509–544.

Vale, R.D., Reese, T.S. & Sheetz, M.P., 1985. Identification of a novel force-generating protein, kinesin, involved in microtubule-based motility. *Cell*, 42(1), pp.39–50.

Verkade, P., 2008. Moving EM: the Rapid Transfer System as a new tool for correlative light and electron microscopy and high throughput for high-pressure freezing. *J. Microsc*, 230(Pt 2), pp.317–328.

Vishwasrao, H.D., Trifilieff, P. & Kandel, E.R., 2012. In Vivo Imaging of the Actin Polymerization State with Two-Photon Fluorescence Anisotropy. *Biophys J*, 102(5), pp.1204–1214.

Watanabe, S. et al., 2014. Nanometer-resolution fluorescence electron microscopy (nano-EM) in cultured cells. *Methods Mol. Biol*, 1117, pp.503–526.

Welzel, O. et al., 2010. Synapse clusters are preferentially formed by synapses with large recycling pool sizes. *PloS One*, 5(10).

White, E.L. & Rock, M.P., 1980. Three-dimensional aspects and synaptic relationships of a Golgi-impregnated spiny stellate cell reconstructed from serial thin sections. *J. Neurocytol*, 9(5), pp.615–636.

Wilke, S.A. et al., 2013. Deconstructing Complexity: Serial Block-Face Electron Microscopic Analysis of the Hippocampal Mossy Fiber Synapse. J. *Neurosci*, 33(2), pp.507–522.

Willig, K.I., Kellner, R.R., et al., 2006. Nanoscale resolution in GFP-based microscopy. *Nat Methods*, 3(9), pp.721–723.

Willig, K.I., Rizzoli, S.O., et al., 2006. STED microscopy reveals that synaptotagmin remains clustered after synaptic vesicle exocytosis. *Nature*, 440(7086), pp.935–939.

Wu, Y. et al., 2009. Biophysical Characterization of Styryl Dye-Membrane Interactions. *Biophys J*, 97(1), pp.101–109.

Xu, K., Babcock, H.P. & Zhuang, X., 2012. Dual-objective STORM reveals three-dimensional filament organization in the actin cytoskeleton. *Nat Methods*, 9(2), pp.185–188.

Xu, K., Zhong, G. & Zhuang, X., 2013. Actin, spectrin, and associated proteins form a periodic cytoskeletal structure in axons. *Science*, 339(6118), pp.452–456.

Zahn, R. et al., 2001. End13p/Vps4p is required for efficient transport from early to late endosomes in Saccharomyces cerevisiae. *J Cell Sci*, 114(10), pp.1935–1947.

Zernike, F., 1942. Phase contrast, a new method for the microscopic observation of transparent objects part II. *Physica*, 9(10), pp.974–986.

Zhang, W.I. et al., 2014. Fluorescent in situ hybridization of synaptic proteins imaged with super-resolution STED microscopy. *Microsc. Res.Tech*, 77(7), pp.517–527.

Zhou, J. et al., 2009. Functionalized gold nanoparticles: Synthesis, structure and colloid stability. *J. Colloid Interface Sci*, 331(2), pp.251–262.

Zhuang, X., 2009. Nano-imaging with Storm. *Nat Photonics*, 3(7), pp.365–367.

Zonnevylle, A. c. et al., 2013. Integration of a high-NA light microscope in a scanning electron microscope. *J. Microsc*, 252(1), pp.58–70.